First On-sky Closed-loop Atmospheric Dispersion Compensation: Demonstration of Sub-milliarcsecond Residual Dispersion Across H-band

PRASHANT PATHAK

Doctor of Philosophy

Department of Astronomical Science

School of Physical Sciences

SOKENDAI (The Graduate University for

Advanced Studies)

First On-sky Closed-loop Atmospheric Dispersion Compensation: Demonstration of Sub-milliarcsecond Residual Dispersion Across H-band

PRASHANT PATHAK

DEPARTMENT OF ASTRONOMICAL SCIENCE

SCHOOL OF PHYSICAL SCIENCES

SOKENDAI (THE GRADUATE UNIVERSITY FOR ADVANCED STUDIES)

Abstract

Several thousand exoplanets have thus far been discovered using indirect methods, such as transit and radial velocity, but very few using direct imaging. To answer questions about the habitability of exoplanets, it is essential to utilize direct detection methods in order to be able to conduct spectroscopic studies. Direct imaging of habitable exoplanets is challenging, as the planet is orders of magnitude fainter than the host star (reflected light from an Earth-like planet is a billion times fainter than its Sun). Upcoming extremely large telescopes (ELTs) will be able to image habitable exoplanets in reflected light around M-type stars, thanks to more moderate planet/star contrast. At present, the field of high-contrast imaging (HCI) is able to image young Jupiter-size exoplanets with current 8-10 m class telescopes. There will be new limitations and error terms faced by ELTs to achieve such large contrasts as those required for terrestrial planets, which are not dominant at current telescopes. Chromatic errors will have a significant effect on the performance of adaptive optics (AO) and for high-Strehl ratio performance, closed-loop correction of atmospheric dispersion will be required.

Traditionally, atmospheric dispersion is compensated for by an atmospheric dispersion compensator (ADC). The ADC control relies on an a priori model of the atmosphere whose parameters are solely based on the pointing of the telescope (the model often also includes temperature and pressure as an input), which is too simplistic and can result in an imperfect compensation, leading to some residuals. For a high-contrast instrument like the Subaru Coronagraphic Extreme Adaptive Optics (SCExAO) system, which employs very small inner working angle coronagraphs, refraction-induced smearing of the point spread function (PSF) due to atmospheric dispersion must be kept to < 1 mas across H-band for optimum performance.

In this thesis, I present a new approach for the closed-loop measurement and subsequent correction of atmospheric dispersion in the science image itself. The work presented in the thesis shows that, for a very precise correction of dispersion, it is important to measure and correct it in the final science image rather than rely on the theoretical calculation alone.

The measurement of residual dispersion in the final science image uses the chromatic scaling of the focal plane calibration speckles. The focal plane speckle can be generated by diffracting the PSF by a deformable mirror or a transparent grating. Due to the wavelength dependence of speckles, in the absence of dispersion (in the PSF) speckles radiate (point towards) from the PSF core and I call this point the radiation center. In the presence of dispersion, speckles no longer point towards the PSF core and the radiation center moves away from the PSF core. By measuring the distance between the radiation center and the PSF core, one can directly estimate the amount of residual dispersion on-sky. This concept and method of quantifying the amount of atmospheric dispersion were developed for the first time throughout the course of this thesis.

After verifying the concept and measurement technique via simulation, on-sky testing was conducted at the Subaru Telescope. The closed-loop measurement and correction were performed using a near-IR camera for sensing and the ADC in the AO188 facility instrument for correction. The value of residual dispersion reduced from 7.99 mas to 0.28 mas in H-band after closing the loop.

This was the first successful demonstration of a closed-loop correction of atmospheric dispersion, which provides a better compensation compared to a single step correction.

On-sky measurements of the residual dispersion allowed me to achieve the following goals:

- Analyze the performance of the look-up table based ADC correction as a function of telescope elevation and varying atmospheric conditions.

- Estimate the presence of dispersion due to internal optics.

- Understand sources contributing to the presence of residual dispersion in the final science image and how frequently dispersion needs to be corrected.

Finally, I tested the impact of closed-loop correction of atmospheric dispersion on coronagraphy. On-sky testing of light leakage through a high-performance coronagraph such as vortex was carried out. In a closed-loop correction of dispersion, the vortex coronagraph performed better in regards to flux suppression compared to the look-up table based correction of dispersion.

In the era of ELTs, this work will be valuable in the field of ground-based HCI to directly image and perform high-precision astrometric measurements of terrestrial exoplanets.

Acknowledgment

Foremost, I would like to express my sincere gratitude to my advisor Prof. Hideki Takami for providing me with the opportunity to carry out my PhD research, for helping me to get into SOKENDAI, and for his patience and caring.

My sincere thanks also to my co-advisor Prof. Olivier Guyon for motivating and guiding me in my research with his unmatched enthusiasm and immense knowledge. I could not have imagined a better mentor for my PhD. I would also like to thank my other supervisors Prof. Yusuke Minowa and Prof. Takayuki Kotani.

I would also like to thank the rest of my thesis committee: Prof. Michitoshi Yoshida, Prof. Naruhisa Takato, Prof. Yutaka Hayano, Prof. Masayuki Akiyama and Prof. Taro Matsuo for their insightful comments.

The past three years have been a period of intense learning for me, not only in the scientific arena but also on a personal level. I would like to thank Dr. Nemanja Jovanovic and Dr. Julien Lozi for the many stimulating discussions that have helped me make meaningful progress throughout my PhD and for all the fun we have had in the last three years. I would like to express my deepest appreciation to all the staff members at Subaru Telescope and NAOJ, Mitaka for their constant help.

I would like to thank Prof. S. Shankaranarayanan and Prof. Joy Mitra for their constant encouragement, and Prof. A. N. Ramaprakash for introducing me to the field of astronomical instrumentation. Also, I thank my dearest friends Gopi Krishnan, Prasanth Varma, Pavan Sharma, Shubhanshu Tiwari, Zahid Hassan and the rest of my batchmates from IISER TVM.

Last but not the least, I would like to express my deep gratitude to my family: my parents Kaushalendra and Shakuntala, and my brother Shashank and sister Shriya for their support throughout my life.

Thank you very much, everyone!
Prashant Pathak

Contents

Table 1: Acronyms and Abbreviations

PSF	Point Spread Function
ELT	Extremely Large Telescope
AO	Adaptive Optics
ADC	Atmospheric Dispersion Compensator
SCExAO	Subaru Coronagraphic Extreme Adaptive Optics
DM	Deformable Mirror
IAU	International Astronomical Union
HZ	Habitable Zone
IR	Infrared
COM	Center of Mass
ExAO	Extreme Adaptive Optics
NCP	Non-Common Path
HCI	high-contrast Imaging
WFS	WaveFront Sensor
RTC	Real Time Control
SHWFS	Shack Hartmann Wavefront Sensor
PyWFS	Pyramid Wavefront Sensor
MEMS	MicroElectroMechanical Systems
IWA	Inner Working Angle
ADI	Angular Differential Imaging
8OPM	Eight Octant Phase Mask
FQPM	Four Quadrant Phase Mask
PIAA	Phase-Induced Amplitude Apodization
VVC	Vector Vortex Coronagraph
LGS	Laser Guide Star
MKID	Microwave Kinetic Inductance Detector
NGS	Natural Guide Star
NIR	Near InfraRed
LOWFS	Low-Order Wavefront Sensor
LLOWFS	Lyot-based Low-Order Wavefront Sensor
FT	Fourier Transformation
FFT	Fast Fourier Transformation
DFT	Discrete Fourier Transformation
RH	Relative Humidity
WFE	Wave Front Erro
SNR	Signal to Noise Ratio
FOV	Field Of View
LWE	Low Wind Effect
ADU	Analog to Digital Unit
IFS	Integral Field Spectrograph

Exoplanets and Detection Techniques

1.1 Introduction

By analogy to our solar system, stars have long been suspected to host exoplanets. This leads to the possibility of life outside the solar system. Presently we live in a technologically advanced world where we can start answering this question: life outside the solar system. There was no proof to the existence of exoplanets (planets outside our solar system) until recently. At present nearly 3483 exoplanets have been discovered, with 581 being part of multi-planetary systems[1] (Han et al., 2014).

1.1.1 History of exoplanet science

For centuries astronomers wondered about the existence of exoplanets, In the 16th century, the Italian philosopher Giordano Bruno came with the theory that all the stars in our night sky are similar to the Sun, so they are also likely to have planets.

> This space we declare to be infinite... In it are an infinity of worlds of the same kind as our own.
>
> Giordano Bruno (1584).

The theory was proven true when the first confirmed detection was made in 1992 by two radio astronomers, Aleksander Wolszczan and Dale Frail, who found two planets orbiting the pulsar PSR B1257+12 (Wolszczan and Frail, 1992; Wolszczan, 1994). But a pulsar is very different from a normal star in the main sequence. The first confirmed giant exoplanet orbiting a Sun-like star (51 Pegasi) was made in 1995, with an orbit period of four day (Mayor and Queloz, 1995). The breakthrough in direct imaging of exoplanets came in 2004, a team from the European Southern Observatory led by Gael Chauvin observed 2M1207b, a planetary mass object orbiting the brown dwarf 2M1207, in constellation Centaurus, with the Very Large Telescope (VLT) at the Paranal Observatory in Chile (Chauvin et al., 2004).

1.1.2 Definition of a planet

Solar system

The solar system consists of celestial bodies bound by the gravitational attraction of the Sun. Among these bodies, five planets are visible to the naked eye and known since the birth of astronomy:

---

[1]exoplanets.org, exoplanet.eu
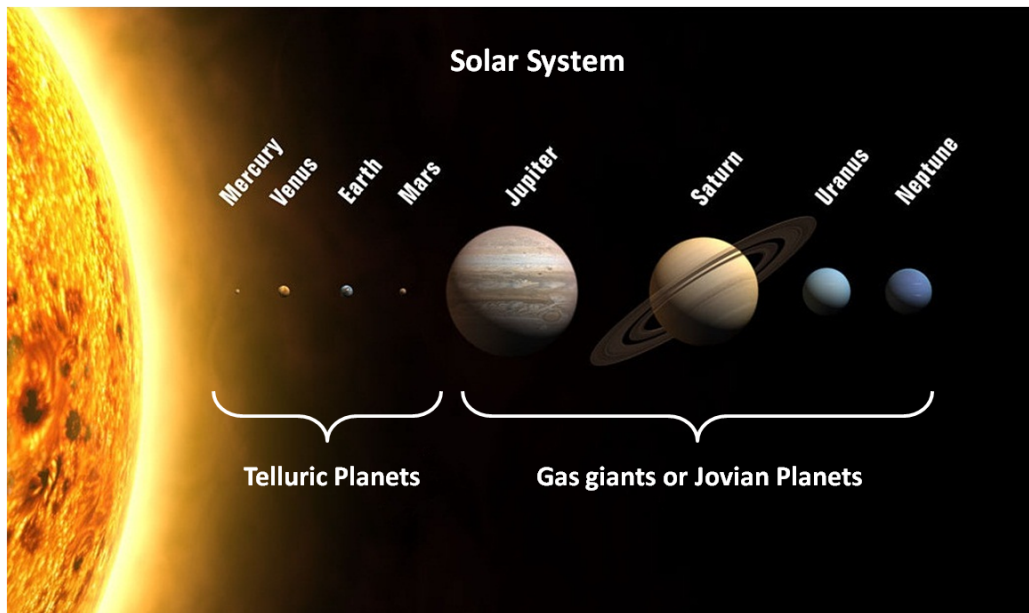
Figure 1.1: Solar system: Sun and planets scaled with the diameter (the distances are out of scale). Courtesy of Wikimedia Commons.

Mercury, Venus, Mars, Jupiter, and Saturn. Later the remaining two planets were discovered using telescope: Uranus (1781) and Neptune (1846) and several dwarf planets, such as Ceres (1801), Pluto (1930) and Eris (2003). Altogether there are eight planets (Earth included) orbiting the Sun. The planets of the solar system can be categorically put into two groups, the telluric and the gas giant (or "Jovian") planets, as shown in Fig. 1.1. The telluric planets are spherical bodies with a crust of rock, and the gas giant planets are spheres composed of mostly gas (Jupiter, Saturn, Uranus, and Neptune). The definition of "planet" was arbitrary and restricted to nine planets of the solar system until 2006. Pluto was among the bodies called "planets" while Eris wasn't among them, even though it is more massive than Pluto. Pluto was given planet status in 1930 because it was thought to be large enough to perturb Neptune's motion. But recently, it was discovered that Pluto could be the part of the Kuiper belt, a family of small bodies located outside the orbit of Neptune. The International Astronomical Union (IAU) in 2006, came up with the scientific definition of 'Planet' instead of being arbitrary to solve the problem Pluto and Eris.

Now the working definition of planet is: a body which orbits around the Sun, has sufficient mass for its self-gravity to overcome rigid body forces so that it assumes a hydrostatic equilibrium (nearly round) shape, and has cleared the neighborhood around its orbit.

The above definition does not apply to exoplanets because they do not orbit around the Sun. The IAU Working Group on Extrasolar Planets in 2003 came up with guidelines as explained below:

The role of nuclear energy

The Sun energy output is approximately constant over billion-yr timescale thanks to the nuclear fusion occurring at the core of the Sun. In contrast, a planet is a body without any internal nuclear energy. Scientific calculations show that thermonuclear reactions at the core can only start if the mass of the body is above 13 Jupiter masses. So any gravitationally collapsed astronomical object, whose mass is below this limit meets the criteria of a planet.

Formation scenario

Apart from the nuclear reaction, another difference between a star and a planet is the way they are formed. Stars are formed through the gravitational collapse of dust and gas clouds and start of nuclear reaction afterward, while planets are formed through the condensation of gas or dust "in a protoplanetary disk", which is formed during the gravitational collapse clouds.

Using the above criteria, a more complete definition for exoplanet can be formulated: a body whose mass is below 13 Jupiter masses orbiting a star other than Sun. But there are some exceptions to this definition, which is discussed next.

Rogue planets

In the process of gravitational collapse of dust and molecular clouds, some stars don't reach the 13 Jupiter mass limit and nuclear reaction never takes place and they are also gravitationally not bound to any star, so they are called rogue or floating planets.

The most fascinating thing about the hundreds of known exoplanets is their huge variety. Some stars have a giant planet like Jupiter where the earth would be, other stars have planets like Jupiter 10 times closer to them than Mercury is to our Sun. Some stars have planets we call "super-earths," rocky worlds bigger than earth but smaller than Neptune. In direct imaging, often there is ambiguity over demarcation between brown dwarfs and exoplanets due to difficulty in estimation of mass from images and spectra.

1.2 A long-term motivation: the search for life

A big quest is to answer the question such as the origin of life and to identify life outside our own planet. The quest started with our own solar system with observations of Mars, Venus, Europa or Titan, and now it has extended beyond our solar system. Figure 1.2 shows the number exoplanets detected as a function of discovery year. The plot includes different exoplanets ranging from sub-earth size to ten times of the earth. The plot shows all exoplanets detected using various techniques. The red color shows exoplanets interior to the habitable zone (HZ) of their star. In this zone, planets are too close to the host star to sustain liquid water like Venus which is too hot due to its close proximity to the Sun. Cyan color shows planets exterior to the HZ, in this zone planets are far from host star and too cold to sustain liquid water. Green color shows planets within the HZ. In this distance, range planets are neither too hot or cold and can sustain liquid water like Earth. The number of exoplanets in the HZ is also shown above each bar of the histogram.

Another criterion to define a planet habitability is mass: if a planet is too big, it will have a large atmosphere of hydrogen and helium gases, creating a greenhouse effect, which will make it too hot to support life, an example being Jupiter, which is big and hot. If a planet is too small, it can't
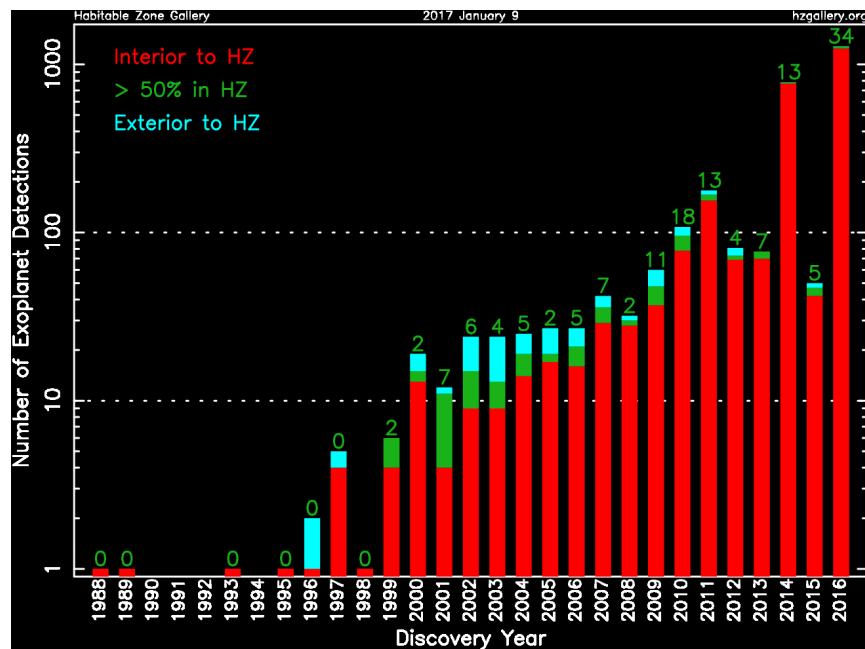
Figure 1.2: Histogram plot showing the number exoplanets detected as a function of discovery year. The red color shows exoplanets interior to the HZ, cyan color shows planets exterior to the HZ and green color shows planets within the HZ. The number of exoplanets in the HZ is also shown at the top of each histogram. Courtesy of Habitable zone gallery

hold an atmosphere, an example being Mercury, too small to hold an atmosphere. So the goal is to find a planet which is similar to earth and resides in the HZ. Figure 1.3 shows the occurrence rate of exoplanets as a function of planet radius. Note that Earth-like planets and super-earth are very common, as well as mini-Neptunes, but big planets are less common. So there should be quite a lot of these in the HZ, and maybe life.

1.3 How to find exoplanets?

There are several challenges in the direct observation of exoplanets. First, exoplanets are so much dimmer than their host star (hundred thousand to billions of time fainter), the photons of planets are usually overwhelmed in the diffracted light from their stars and the exoplanet gets lost in the noise. One can look at the thermal emission of exoplanets, but unless the planet is very young and massive, most of them have reached thermal equilibrium and do not emit a lot of light in infrared (IR). Second, since the observed stars are so far, most of the exoplanets are angularly very close to their host star.

Despite these difficulties, there have been numerous discoveries of exoplanets using indirect methods. Indirect detection methods rely on the influence of exoplanet on its host star, such as change in flux, spectrum, and position. Figure 1.4 shows a cumulative number of detected exoplanets using various techniques as a function of discovery year. At present, the number exoplanets detected using direct imaging is very small compared to indirect methods such as transit and radial velocity. Before discussing direct imaging technique of exoplanets, I will briefly describe two important
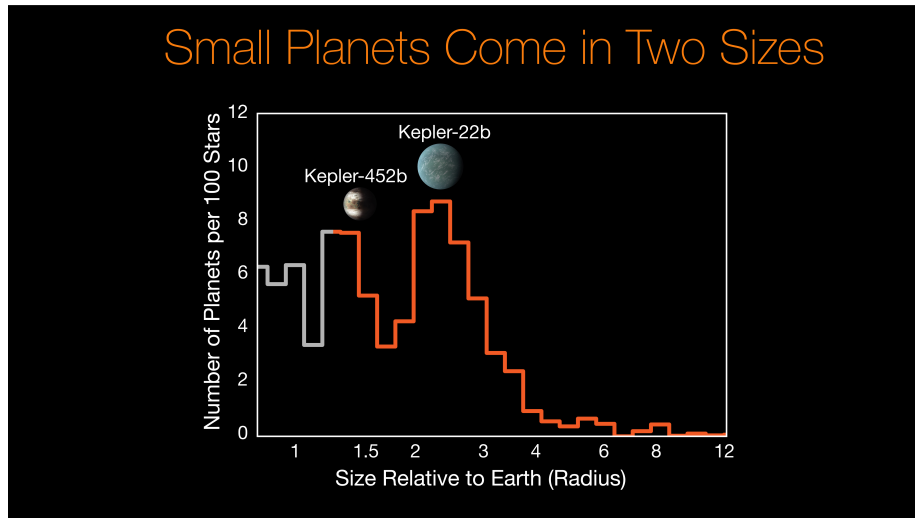
Figure 1.3: Exoplanets discovered using the Kepler mission, according to the size distribution. Courtesy of www.nasa.gov
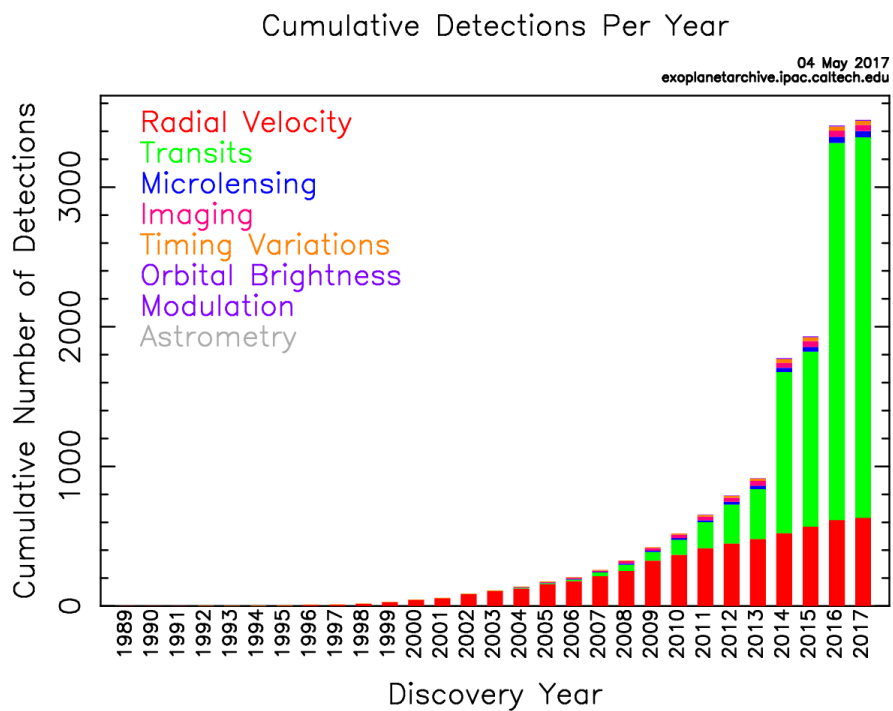
Figure 1.4: Bar plot shows the cumulative number of detected exoplanets using various techniques as a function of discovery year. Courtesy of NASA Exoplanet Archive

indirect techniques: transit and radial velocity method.

1.3.1   The radial velocity method

The radial velocity method is historically the first method used to find exoplanets, it is also called the "wobble" method. The concept behind this method is: if a planet or multiple planets are present around a star, the center of mass (COM) of the systems lies away from the stars COM. The star orbits around the COM of the system (wobbles). To measure the star's velocity, the Doppler effect is used: the spectrum is blue shifted when a source moves towards us and red when it moves away. Using high-resolution spectroscopy, one can precisely measure the Doppler shift in the star light, giving the radial velocity measurements of the star. By using radial velocity measurements, the exoplanet mass can be estimated.

A wide range of instruments now look for exoplanets using this technique. An example of instrument using Radial Velocity method is HARP (High Accuracy Radial Velocity Planet), which was commissioned in 2002 on the 3.6 meter La Silla Observatory in Chile. Since commissioning, it has discovered 130 exoplanets. HARPS can attain a precision of ≈ 1 m/s (Mayor et al., 2003; Cosentino et al., 2012).

1.3.2   The transit method

The transit method uses the fact that some planets are transiting in front of the star when observed from Earth. This transit blocks a fraction of the starlight. So if the stellar flux is measured accurately, one can measure the dip in flux induced by a planet. This method is powerful because it only requires a well-calibrated measurement of the stellar flux. But not all planets are transiting, and that fraction of transiting planets decrease rapidly with orbital period. Also, observations have to be carried out very frequently, since one or two events does not always indicate the presence of a planet. Advantages of this method are, its easier to detect exoplanets compared to other techniques.

A lot of ground- and space-based exoplanets surveys are carried out using this method, especially with space missions like CoRoT [2] and Kepler [3]. Thanks to the Kepler mission, now the majority of exoplanets were discovered using this method. So far Kepler has a confirmed detection of $2,335$ exoplanets of which 30 are being in the HZ. The Hubble Space Telescope[4] and MOST (Microvariability and Oscillations of STars) (Walker et al., 2003) telescopes have also found and confirmed few exoplanets using this technique. The future space mission based on this method is TESS (Transiting Exoplanet Survey Satellite) (Ricker et al., 2014), which is a space-based telescope by NASA's Explorers program and it is scheduled to launch in March 2018. The objective of this mission is to study the mass, size, density, and orbit of small exoplanets in the HZ. It will act as a precursor to the James Webb Space Telescope[5] (successor to Hubble Space Telescope), which will use targets provided by TESS for further characterization.

---

[2]https://corot.cnes.fr/en/COROT/index.htm

[3]https://www.nasa.gov/mission_pages/kepler/main/index.html

[4]http://hubblesite.org/

[5]https://www.jwst.nasa.gov/

There are few ground-based surveys which are useful in detecting giant exoplanets. Different ground-based transiting surveys are SuperWASP, HATNet Project, XO Telescope, Trans-Atlantic Exoplanet, etc. Out of these instruments, most of the exoplanet detections came from SuperWASP and HATNet (Hungarian Automated Telescope Network), SuperWASP has detected roughly 134 exoplanets (Pollacco et al., 2006) and 60 exoplanets were discovered by HATNet survey (Bakos et al., 2004).

1.3.3   Direct detection

Direct imaging is one of the most important technique in the search for exoplanets. If one can capture light from an exoplanet, then spectroscopy can be used to study the atmospheric composition. This can provide information like the size of the planet, its orbital motion, its temperature or composition, which is vital when looking for signs of life. Direct detection is also important to study the formation and evolution of these exoplanetary systems, when one or more planets are present. So far 43 exoplanets have been directly imaged, although most of them are closer to brown dwarfs than to more conventional planets. Solving the direct imaging challenge of exoplanets and discs requires:

- Angular resolution: a small angular separation between the host star and the exoplanet. The projected separation is $0.1''$ for an exoplanet orbiting at 1 AU from a star at a distance of 10 pc.

- Contrast: A typical contrast between a star and its planet varies from 10^{-4} for a young giant planet in thermal emission to 10^{-10} for an Earth-like planet in reflected light around a Sun-like star.

These two requirements are crucial to directly image exoplanets and discs. It is important to achieve both requirements in some form, although it is possible to relax one of the requirements and still achieve that goal. I have calculated the reflected light contrast for Earth-size exoplanets in the HZ of the stars within 20 pc from us. Figure 1.5 shows the reflected light contrast for an Earth-size planet as a function of angular separation from the host star, the circle area encoding the distance from us (larger the area close to us). The calculation is based on the catalog compiled by Prof. Olivier Guyon, which includes 2581 stars within 20 pc with the assumption of an Earth-size planet for each star and reflectance from the planet surface is assumed to be a Lambertian reflection at maximum elongation.

The space-based mission can achieve very high contrasts unattainable from Earth, but their angular resolution is limited. On the other hand, ground-based telescopes can achieve high angular resolution, especially with the future Extremely Large Telescope (ELTs), but are limited in contrast by the atmospheric turbulence. The answer is to employ adaptive optics (AO), which lets us achieve diffraction-limited image using a ground-based telescope. To achieve high-contrast using a ground-based telescope, techniques include extreme AO (ExAO), coronagraphy, sparse aperture masking, interferometry, etc. At present ExAO assisted imaging is the only option to be able to reach both the angular resolution and contrast below 10^{-7} at a few λ/D.

To achieve high-contrast, ExAO alone is not sufficient because the presence of Airy pattern (due to outer aperture edge) and of a residual speckle halo contaminates the region of interest within $1''$. These residuals speckles are the results of diffraction from telescope spiders, secondary mirror, residual wavefront error (WFE) (uncorrected atmospheric perturbations), non-common path (NCP) errors and imperfect optics within the telescope and instrument. In an ideal point spread function (PSF), at $4\lambda/D$, the Airy pattern still has an intensity 10^{-4} of the peak value. Therefore, detecting
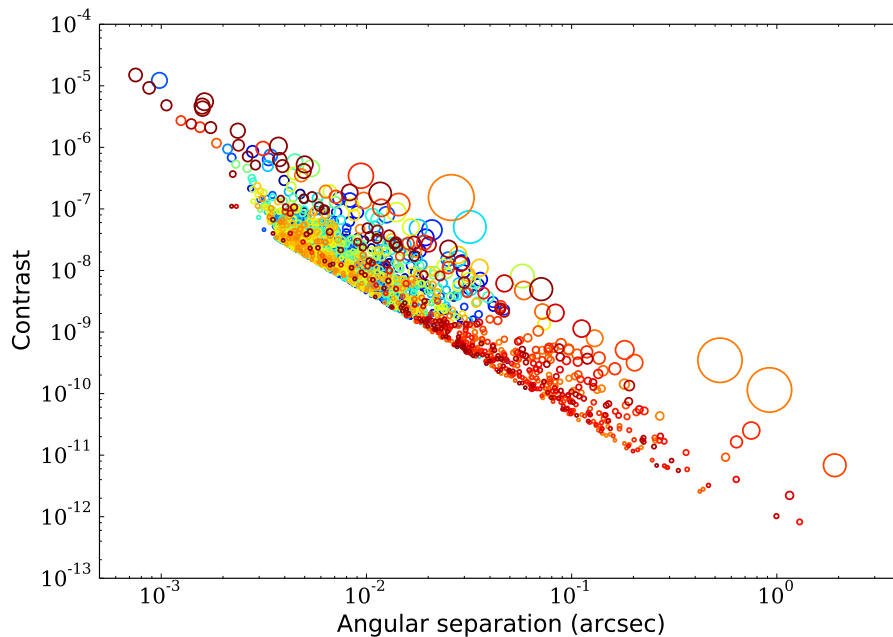
Figure 1.5: Reflected light contrast calculation for the Earth-size exoplanets in the HZ of stars within 20pc. The circle area represents the distance to exoplanets (larger the area close to us).

any exoplanet at this level of contrast without the aid of any other technique is challenging and would require a long integration time to accumulate enough signal. To overcome this, high-contrast imaging (HCI) instruments employ coronagraphs to suppress the light from host-star and enable the detection of faint companions around stars. As mentioned previously, the presence of residual speckles makes it challenging to detect planets and they cannot be suppressed by coronagraphs. Unlike the diffraction pattern, quasi-static speckles vary temporally on different timescales: from a fraction of a second to minutes. These are hard to calibrate and remove because they can mimic a planet signal. The quasi-static speckles are caused by temperature variance in the NCP to the AO and uncorrected WFE. There are techniques such as speckle nulling that can actively remove these speckles on-sky (Martinache et al., 2014a). The other techniques involve strategic observing and post-processing based on differential imaging techniques, which are discussed later in this chapter.

The first ExAO systems include PALM-3000/P1640 (Dekany et al., 2013), followed by Ma-gAO (Close et al., 2012). Three HCI instruments are now installed on 8 m class telescopes: Gemini Planet Imager (GPI) at Gemini South (Macintosh et al., 2014a), Spectro-Polarimetric High-contrast Exoplanet REsearch (SPHERE) at the VLT (Beuzit et al., 2008a) and Subaru Coronagraphic Extreme Adaptive Optics (SCExAO) at Subaru (Jovanovic et al., 2015b). The first two are already operational and have started producing science results and the SCExAO is undergoing commissioning. The next section discusses architecture and fundamentals of AO instruments.

For space-based detection of exoplanets, the Wide Field Infrared Survey Telescope (WFIRST) is a proposed space-based infrared telescope. Apart from a different science mission, it will be also equipped with different coronagraphs, which will enable direct imaging of exoplanets billion times fainter than the host star.
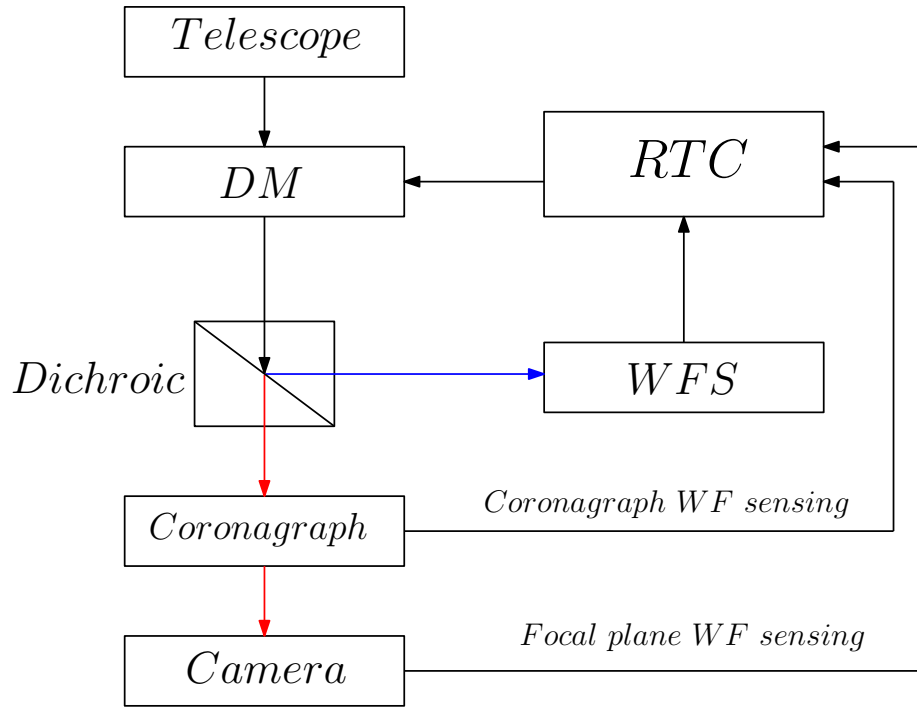
Figure 1.6: Standard architecture of an AO plus high-contrast instrument.

1.4   Fundamentals of adaptive optics

1.4.1   Imaging under atmospheric turbulence

The angular resolution of a ground-based telescope in the presence of atmospheric turbulence, or seeing, is given by λ/r_0, where r_0 is the Fried parameter (coherence length). For a good astronomical site such as Maunakea, the Fried parameter is about 20 cm at 550 nm, giving a seeing of 0.4". The variance defined as the optical phase distortion with a mean square value of 1 rad^2 over a circular aperture of diameter r_0, scales as $\lambda^{6/5}$. Any telescope with diameter a $D > r_0$ has no better spatial resolution than a telescope for which $D = r_0$.

Another important parameter to characterize atmospheric seeing is coherence time. It is defined as the time interval over which the wavefront variance changes by 1 rad^2. The temporal evolution of atmospheric turbulence is given by the Taylor hypothesis. According to the Taylor hypothesis of frozen flow of turbulence, the variations of the turbulence are caused by a single layer that is transported across the aperture by the wind in that layer. The coherence time by the Taylor hypothesis is $\tau_0 \approx r_0/v$, where v is the wind speed in the dominant layer. The more realistic evolution of turbulence is given by the Greenwood time delay. It is defined as $\tau_0 = 0.314\, r_0/v$ where v is the mean wind speed weighted by the turbulence profile along the line of sight (Roddier, 1981). This parameter sets the speed at which an AO system should run to achieve a 1 rad^2 temporal WFE requirement. It is also proportional to $\lambda^{6/5}$, so the AO correction in the near-infrared can generally be slower than in the visible.

1.4.2 Architecture of AO systems

Here, I briefly describe the architecture of an AO system, for more details please see (Roddier, 2004). The architecture of first generations of AO systems is composed of three key components as shown in the Fig. 1.6:

- A wavefront sensor (WFS), whose function is to measure wavefront distortions.

- A real-time control (RTC), which multiplies the WFS signals by the control matrix to create the DM commands.

- A deformable mirror (DM), which corrects for the distorted wavefront.

The above-mentioned elements of an AO system are briefly discussed in the following section.

1.4.3 Wavefront sensing

A WFS consists of an optical component and a high-speed detector. The WFS is responsible for measuring the distortion of the wavefront in real time. The spatial resolution, speed and sensitivity are the three parameters driving the design. A detailed review of WFS is given in Rousset (1999). One of the main challenges by ExAO system is to get enough spatial resolution by a WFS to correct as many modes as possible by driving the DM, others include speed and sensitivity. The fundamental limit to WFS is set by photon noise. In addition to speed and sensitivity, other WFS requirements include:

- Linearization: it is desirable to have a linear relationship between the wave-front and the intensity measurements.

- Broadband: the sensor should operate over a wide range of wavelengths.

There are several WFSs that are used by the AO/ExAO systems. I will briefly introduce the concept of two most common WFSs, which work by measuring the slope of the wavefront.

Shack-Hartmann WFS (SHWFS)

The SHWFS (Shack et al., 1971) is a commonly used WFS in AO because of its simplicity and mature technology, implemented by both GPI and SPHERE. It consists of a microlens array as shown in the Fig. 1.7 (a), placed in a conjugated pupil plane that samples the incoming wavefront. Each lenslet creates an image of the source, called a spot, at its focus onto a CCD. The position of each spot on the detector varies as the function of deformations in the wavefront. Therefore, measuring the spot displacement enables to derive the local slope of the wavefront in each lenslet.

Pyramid Wavefront Sensor (PyWFS)

The pyramid wavefront sensor (PyWFS) was proposed in 1995 by Ragazzoni (1996). PyWFS uses a 4-sided glass prism at a focal plane to generate 4 aperture images as shown in Fig. 1.7 (b). The PyWFS splits the focal plane into four quadrants, which are imaged by a relay lens onto the pupil plane, producing four images of the pupil. The subdivision occurs at the image plane, not the pupil plane. The intensity distribution in the images of the aperture are used for estimating the phase of the wavefront. It is similar to the Shack-Hartmann using quad cells: it measures the average slope
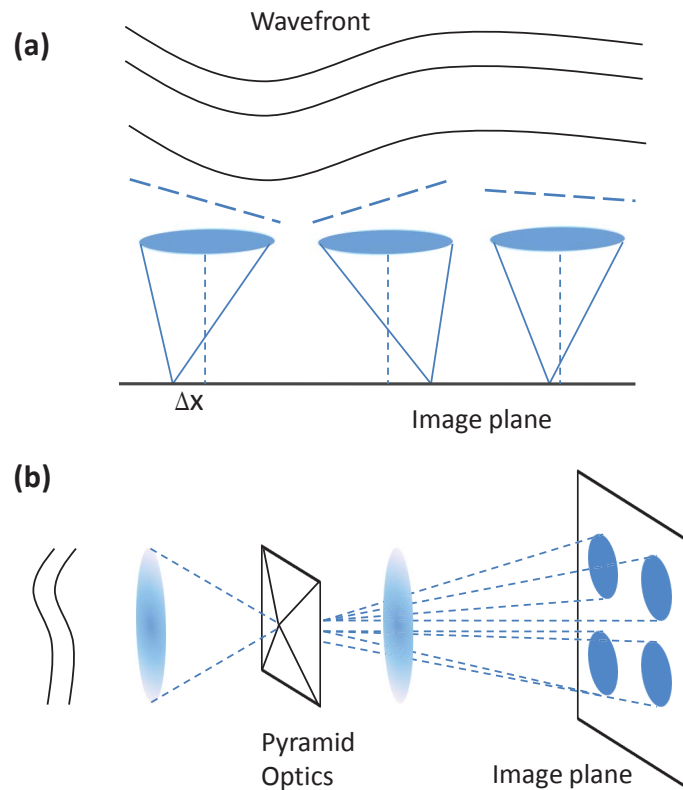
Figure 1.7: Principle of WFS: (a) SHWFS is based on lenslet array (b) PyWFS is based on pyramid optics.

over a subaperture. When the aberrations are large, the pyramid sensor is very non-linear. SHWFS and modulated PyWFS provides a large linear and dynamical range but at the cost of sensitivity. However, fixed PyWFS provides good sensitivity but over a smaller range (limited to < 1 radian) and modulated PyWFS (modulation can be achieved by physically moving the pyramid optics or by controlling the beam using a steering optics) is linear over the modulation width.

1.4.4 Deformable mirror

The DM is an integral part of an AO system. The basic process involved in the wavefront correction is achieved in two steps. First: correction of the atmospheric tip-tilt, which causes an overall shift of the PSF and is corrected by using a tip-tilt mirror (most DMs lack stroke to correct for tip-tilt). Second: correction of low and higher-order modes is done using a DM. There are several types of DM used in astronomy such as: Segmented, Continuous face-sheet, Piezoelectric, Bimorph, Membrane mirrors, Magnetically actuated mirrors, Micro-Electro-Mechanical Systems (MEMS), and Adaptive Secondary Mirror. A good review of different DM technologies can be found in Madec (2012).
A DM is characterized by the following parameters:

- Number of actuators: the number of actuators is set by WFE requirement, few 100 actuators

are sufficient to achieve a diffraction-limited PSF at current telescopes in near-infrared (NIR). However, for the HCI, a larger number of actuators (in the range of 1000's) are desirable to correct higher spatial frequencies.

- Actuator stroke: the stroke is the maximum possible actuator displacement when the maximum rated voltage is applied. The displacement is typically in positive or negative excursions from some central null position. High stroke DMs are usually used to correct high-amplitude low-spatial frequency components of the aberration whereas low stroke DMs are usually used to address low-amplitude high-spatial frequency components.

- Influence function: it corresponds to the characteristic shape of the response of a single actuator, i.e. the influence of an actuator on its neighbors.

The design of a DM is a trade-off between fast response, density of the actuators, stroke, and accuracy. MEMS offer the smaller actuator pitch, allowing small DMs with large number of actuators. MEMS use a thin silicon membrane with a highly reflective metallic coating, supported by an array of electrostatic micro-actuators. MEMS DMs are composed of actuator top plate to the membrane through a rigid post, which is controlled to create the local deformation of the membrane. MEMS have several advantages: sub-nanometer repeatability, high stability, negligible hysteresis, low weight, compact size, high speed, and large number of actuators with a proportionately large stroke. This solution was preferred by HCI instruments such as GPI and SCExAO, combined with a second low-order high-stroke DM performing a first correction.

Wavefront fitting error

The DM cannot exactly match the shape of the turbulence model described by Kolmogorov. This error arises due to a finite spatial sampling of the wavefront with a finite number of correcting elements of the DM. The wavefront fitting error for a DM with subaperture diameter d is given by,

$$\sigma^2_{DM\_fitting}(rad^2) = \mu \left(\frac{d}{r_0} \right)^{5/3}, \tag{1.1}$$

where r_0 is Fried's parameter and μ ($= 0.28$ for a DM with continuous phase sheet) is constant dependent on the design of a DM.

1.5 Extreme AO and high-contrast imaging

1.5.1 Wavefront error requirement

There are many independent factors that influence the performance of an AO system. A way to determine how well an AO system performs can be given by Strehl ratio (SR), which is the ratio of the peak on-axis intensity of an aberrated PSF, to that of a reference unaberrated PSF. The SR is related to the WFE via the Maréchal approximation (Hardy, 1998),

$$SR \approx \exp(-\sigma^2_\phi), \tag{1.2}$$

where σ_ϕ is the variance of the phase aberration across the pupil. The above approximation is valid when Strehl ratio $> 10\%$ or so ($\sigma^2_\phi < 2.3 \ rad^2$). According to this approximation, to achieve SR

$> 90\%$, the AO correction must achieve a wavefront residual $\sigma_\phi^2 < 0.1\ rad^2$. As discussed previously in Eq. 1.1 the DMs fitting error $\sigma_{DM\_fitting}$ is one of the major contributor to the WFE. The other errors contributing to the wavefront are discussed briefly:

Temporal error: It is the time lag error, which is based on the control loop update frequency and the wind speed during observations. If an AO system corrects turbulence perfectly but with a time lag given by τ, the WFE due to time lag will be,

$$\sigma_{temporal}^2 = 0.28 \left(\frac{\tau}{\tau_0} \right)^{5/3}, \tag{1.3}$$

where τ_0 is coherence time. To reduce the temporal error, AO systems have to run significantly faster than coherence time.

Wavefront sensor measurement error, σ_{WFS}^2 results from photon noise and detector read noise.

Alignment error, $\sigma_{alignment}^2$ residual alignment error between the DM and the WFS.

Assuming that these values are uncorrelated, their variances can be added to determine total WFE, $\sigma_\phi^2 = \sigma_{DM\_fitting}^2 + \sigma_{temporal}^2 + \sigma_{WFS}^2 + \sigma_{alignment}^2$.

For a single conjugate AO, a typical SR of 50% at Ks band requires 0.7 rad^2 of total phase variance, which is suitable for coronagraphy as stated by Sivaramakrishnan et al. (2001),

the improvement in image quality that AO provides makes it possible to study the region within a few times the diffraction width of the image of a bright star, with dynamic range limited by the presence of the halo and bright Airy rings rather than by atmospheric seeing. Systems delivering $50-70\%$ *Strehl ratio are suitable for coronagraphic instrument to suppress maximum of the on-axis starlight and gain sensitivity to faint structure surrounding a bright source.* The next section discusses coronagraphy.

1.5.2   Coronagraphy

The role of a coronagraph is to block the starlight from an on-axis source and let as much off-axis signal, i.e. the light from an off-axis source (a companion, planet or circumstellar material) to pass through the optical system. The coronagraph was invented by the French astronomer Bernard Lyot in 1939 (Lyot, 1939). He invented a solar coronagraph to study the corona of the sun, the access to which was previously limited to total solar eclipses. The invention by Bernard Lyot initiated the field of stellar coronagraphy to study the immediate surrounding of stars other than our sun. The stellar coronagraphs can only remove the static coherent part of the diffraction pattern but cannot remove speckles due to dynamic WFEs. Coronagraphs also help to overcome the limited dynamical range of detectors by avoiding saturation. Coronagraphs can be divided into two categories: (1) those using amplitude masks (act on the amplitude) and (2) those using phase masks (act on the phase of the wavefront). Depending on the coronagraphs, masks are placed in either focal or in a pupil plane. Below, I list key definitions, which are constantly used to define the performance of a coronagraph:

- Raw contrast: The ratio of the planet light to the star light.

- Inner Working Angle (IWA): smallest angle on the sky at which the designed contrast is achieved and the planet light is reduced by no more than 50% relative to throughput at large angular separation.

- Throughput: fraction of planet light in the photometric aperture.

- Bandwidth: wavelength range over which high-contrast is achieved.

- Sensitivity to WF errors: contrast is degraded in the presence of low-order aberrations such as tip-tilt, stellar angular size (stars will be partially resolved for ELTs) and atmospheric dispersion.

Most coronagraph designs are a trade-off between coronagraphic contrast, throughput, IWA, and bandwidth. A review of current state-of-the-art coronagraphs can be found in Mawet et al. (2012). Below I list few stellar coronagraphs which are widely used in HCI:

- The apodized Lyot coronagraphs, are an evolution of the Lyot coronagraph to include an apodized pupil to improve the contrast by removing the diffraction from edges of the pupil. They are typically limited to an IWA of $3\lambda/D$ in their current design. Examples of instruments employing these coronagraphs include VLT/SPHERE (Carbillet et al., 2011) and Gemini/GPI (Soummer et al., 2009).

- Phase mask coronagraphs, employ phase masks, which creates a phase-shift in the focal plane. These coronagraphs have a smaller IWA than conventional Lyot coronagraphs. The four-quadrant phase mask (FQPM) and vortex coronagraph are examples of this concept (Rouan et al., 2000; Mawet et al., 2010). Examples of instruments employing these coronagraphs include Keck/NIRC2, VLT/VISIR, VLT/SPHERE and Subaru/SCExAO. These coronagraphs have smaller IWA but they are sensitive to low order aberrations.

- Phase/amplitude apodization coronagraphs, employ apodization of the pupil in order to smooth the pupil edges that create the Airy rings, implemented through a continuous amplitude mask or a binary mask known as a shaped pupil (amplitude apodization in the pupil plane and phase mask in focal plane) (Kasdin et al., 2003). The phase-induced amplitude apodization coronagraph (PIAA) on Subaru/SCExAO (Guyon, 2003) uses lossless pupil apodization through phase remapping.

1.5.3   Coronagraphic low-order WFS

Small IWA coronagraphs are very sensitive to low-order aberrations (tip-tilt, focus, astigmatism, coma and so on) and bandwidth (chromaticity). One of the major obstacles that they face is the lack of efficient control of the low-order WF aberrations creating stellar leaks near the coronagraph's IWA. For ground-based telescopes, fast varying phase errors are induced in the wavefront due to the atmospheric fluctuations, optical/mechanical vibrations and telescope pointing errors. In order to directly image exoplanets in the HZ, it is crucial to control WF around the first few λ/D of the telescope PSF for terrestrial-like exoplanet science (Guyon et al., 2006). Most high-performance coronagraphs (small IWA) require the best possible correction of low-order aberrations, in order to suppress light efficiently. The uncorrected low-order aberrations are not rejected by the coronagraphs, which leads to leakage of light around the coronagraph degrading the achievable coronagraphic contrast.

To prevent starlight leakage at the IWA of a coronagraph, HCI instruments use a dedicated low order wavefront sensors (LOWFS) near to coronagraph location to correct for low order aberrations. A number of practical solutions are employed by HCI instruments, which are reviewed in Mawet et al. (2012). SCExAO uses a Lyot-based low-order wavefront sensor (LLOWFS), which senses aberrations using the rejected starlight diffracted at the Lyot plane Singh et al. (2015a).

LOWFS are good at measuring low-order aberrations and correct them by driving the DM. However, LOWFS cannot measure aberrations due to atmospheric dispersion, which can be attributed as a weighted average of tip-tilt, results in a leakage around small IWA coronagraphs. The more details about atmospheric dispersion and its effects are discussed in the next chapter.

1.5.4 Differential imaging

Even after the use of various wavefront sensing techniques and coronagraphy, some residual static speckles remain, which can mimic a planet signal or can overwhelm the signal of a faint companion. These speckles evolve slowly due to variations in the temperature and telescope flexure. Differential imaging techniques are used frequently to find a criteria that distinguish the image of the planet from the residual speckles.

Angular Differential Imaging (ADI)

ADI is a HCI technique that identifies quasi-static speckle using the relative motion of the sky. The fixed pupil mode of observation is used to disentangle between a fixed speckle and a rotating noise and facilitates the detection of nearby companions (Marois et al., 2006).

Advanced data reduction algorithms have been developed to further improve ADI such as locally optimized combination imaging, Karhunen-Loéve Image Projection (Galicher et al., 2011; Lafrenière et al., 2007; Mugnier et al., 2008; Soummer et al., 2012).

1.6 Summary

In this chapter, I provide the motivation for direct imaging of exoplanets and challenges behind it. I present how ground-based telescopes are more suited for imaging exoplanets compared to space-based telescopes. I briefly discussed various limitations for ground-based HCI instruments and how they can be overcome by employing various technologies such as ExAO, high-performance coronagraphs, and coronagraphic LOWFS.

For direct imaging of habitable planets in reflected light, a large contrast ($10^{-8} - 10^{-10}$) is required, which can be achieved by employing small IWA coronagraphs. These small IWA coronagraphs are very sensitive to low-order aberrations such as tip/tilt and dispersion. A coronagraphic LOWFS can be employed such as LLOWFS to measure these low-order aberrations and correct it by driving the DM. However, these sensors cannot easily measure the presence of residual atmospheric dispersion, which can become a dominant source of noise once the other aberrations have been accounted for. In the next chapter, I discuss the theory behind atmospheric dispersion models and their limitations.

Atmospheric Refraction

2.1 Introduction

Ground-based telescopes are adversely affected by the Earth's atmosphere, which is responsible for different types of wavefront errors. As light from the astronomical object passes through the Earth's atmosphere its path deviates from a straight line connecting the observer and the target. This bending is due to the refractive nature of the atmosphere. The amount of refraction depends on the refractive index of air along the path traversed by the light. As the refractive index varies throughout the atmosphere, increasing from upper to the ground layer, the path of the light traveled through the atmosphere is given by Fermat's principle of least time. As stated by this principle: the path taken by the light between two points is the path that can be traversed in the least time. Due to Fermat's principle, as light passes through the atmosphere its path is given by a curve rather than a straight line.

Due to atmospheric refraction, there is a change in the apparent position of the PSF, which affects the precision astrometry of astronomical objects. Atmospheric refraction also causes a chromatic shift in the PSF, commonly known as dispersion, which causes elongation in the PSF (both effects discussed in detail see Sec. 2.2). In the past three centuries astronomers have studied refractive bending of light due to Earth's atmosphere in order to improve astrometric measurements of astronomical objects. Historically, a large part of astronomy was devoted to measuring the precise position and motion of objects in the sky. To account for the refraction there have been many formulations of the atmospheric refraction model. A well-presented review of calculation of the atmospheric refraction throughout history is presented by Young (2004). The presence of atmospheric dispersion affects the performance of AO systems greatly by degrading the achievable Strehl ratio. The correction of atmospheric dispersion is discussed next.

Atmospheric dispersion correction is done using an atmospheric dispersion compensator (ADC), which consists of two prisms with similar dispersive properties. The amount and direction of the compensation are adjusted by rotating the prisms to form a dispersion compensation vector opposite to the atmospheric dispersion (Wynne, 1996). Chapter 4 discusses the operation of an ADC. For all ADC systems, the correction is applied based on a look-up table consisting of dispersion values as a function of telescope elevation angle (using atmospheric parameters such as temperature, pressure, relative humidity) (Allen, 1973; Ciddor, 1996). In particular, Subaru Telescope's adaptive optics, AO188, also employs a look-up table based ADC (Egner et al., 2010). More detail about the calculation of look-up table based atmospheric dispersion is described later in this chapter.

In classical AO systems such as AO188, the level of correction for dispersion from a look-up table based ADC is usually good enough to achieve moderate Strehl performance. In the case of

AO systems delivering high-Strehl ratio performance, residual atmospheric dispersion becomes the dominant limitation to image quality. As an example, Skemer et al. (2009) showed that at 10 μm (N-band), where AO systems are capable of eliminating wavefront error almost entirely, the PSF quality was dominated by atmospheric dispersion. In the case of HCI that try to image exoplanets at low IWA, sub-milliarcsecond of residual dispersion can lead to leakage of light around coronagraph. The look-up table based correction of atmospheric dispersion results in imperfect compensation due to varying atmospheric conditions and instrumental biases, leading to the presence of residual dispersion in the PSF and is insufficient when sub-milliarcsecond correction is required (Spanò, 2014).

2.2 Effects of atmospheric refraction

2.2.1 Astrometry

In astronomy, the field of astrometry deals with the precise measurements of the positions of astronomical objects. Astrometry is key to answer questions like celestial mechanics, stellar dynamics, galactic astronomy and detection of exoplanets. Astrometric measurements are greatly affected by atmospheric refraction, which changes the apparent position of stellar objects. Atmospheric refraction can change the apparent position by $\approx 100''$ for a zenith angle of $60°$. It is necessary to account for atmospheric refraction to achieve high-precision astrometry.

Here, I discuss astrometric requirements for current and future instruments. The Gemini/GPI astrometric accuracy requirement was set to be 1 mas, which was not achieved on-sky due to ADC alignment errors (Hibon et al., 2014). The astrometric error budget for the Thirty Meter Telescope (TMT) has been set to be < 2 mas (H-band) (Schöck et al., 2014) and for the ADC of the Infrared Imaging Spectrograph (IRIS), the residual dispersion needs to be < 1 mas across a given passband (Phillips et al., 2016). The work presented here will show that these requirements are difficult to achieve on-sky even with 8-10 m class telescopes by employing just a look-up table based correction of dispersion.

2.2.2 Coronagraphy: astrometry using satellite speckles

ADI is a powerful HCI technique, which removes quasi-static speckles in post-processing to enable the detection of exoplanets as discussed in the previous chapter. In ADI one of the challenges is to find the precise location of PSF in post-coronagraphic/PSF saturated images for co-centering of ADI frames, this is very crucial to employ the full potential of ADI technique. Sivaramakrishnan and Oppenheimer (2006) showed that by using a grid of lines in the pupil, it is possible to diffract light into speckles in the focal plane. The speckles are equally spaced around the PSF, which aids in determining the exact position of the target. The brightness of the speckles is determined by the width of the grid lines and can be used to measure the brightness of faint features when the star is either saturated or behind a coronagraph. This was later improved upon by implementing incoherent speckles (Jovanovic et al., 2015a). The use of satellite speckles for astrometry in broadband light is challenging due to the presence of residual dispersion, which introduces color based astrometric errors (Wertz et al., 2017).

2.2.3   Coronagraphy: high-contrast operation

The current HCI instruments on $8 - 10$ m class telescopes are only able to image young Jupiter mass exoplanets at wide separation (> 0.1 arcsec) (Marois et al., 2008; Kraus and Ireland, 2012; Wagner et al., 2016). Upcoming ELTs may be able to image closer-in habitable exoplanets around M-type stars using reflected light, with a contrast of 10^{-7} at $2\lambda/D$. To achieve high contrast, ELTs will face new limitations (such as low order aberrations) that are not dominant terms on the current smaller telescope. As discussed in the previous chapter, a potentially significant source of coronagraphic leakage comes from atmospheric dispersion, which can be particularly devastating if the coronagraph operates at a small IWA. As such, GPI set a residual dispersion limit for coronagraphy of < 5 mas, while the SCExAO instrument set a requirement of < 1 mas in H-band. The motivation behind the low residual dispersion requirement for SCExAO is to reach high contrast at small angular separation. The contrast in that region is limited by stellar angular size and residual low-order aberrations. The angular stellar size is typically around 1 mas and creates a stable and well-understood residual leak in the focal plane. The aim is then to keep all other sources of leakage —e.g. tip-tilt, low-order modes, residual dispersion— smaller than 1 mas. Even if this value is not reached, the precision of the sensors has to be better than 1 mas to allow for post-processing calibration. The rest of the chapter discusses the calculation of atmospheric refraction and limitation on the precision of the calculation.

2.3   Atmospheric refraction model

The calculation of atmospheric refraction utilizes two different geometrical models: the plane-parallel atmospheric model and the concentric spherical shell model; the latter being widely used in astronomy due to better accuracy at large zenith angles, which is discussed in detail later in this chapter. The concentric spherical shell model has also been incorporated in the commercial design software ZEMAX, which is widely used to design and simulate optical systems. ZEMAX provides a built-in model for calculating the atmospheric dispersion, which is based on a numerical solution to the refractive integral utilized in the concentric spherical shell model for the atmosphere (Spanò, 2014). The next section describes the plane-parallel model for calculation of atmospheric refraction.

2.3.1   Plane-parallel atmospheric model

In this section, I discuss atmospheric refraction using the plane parallel model. The derivation presented here follows closely works by Smart (1965) and Green (1985). A visualization of the plane-parallel model is provided in Fig. 2.1. Figure 2.1 (a) represent atmospheric pressure decreasing with elevation. Figure 2.1 (b) shows refraction of light through the atmosphere assuming a single homogeneous layer ($z_0 = z_1$) of refractive index n. Here the observer is at O and the zenith angle is given by z_0. If we apply Snell's law of refraction at the upper boundary (space and atmosphere), we get

$$n \sin z_1 = \sin z_2. \tag{2.1}$$

Now lets consider more parallel layers, as shown in Fig. 2.1 (a). Applying Snell's law on the successive refraction of light through each layer, gives us a relationship between the upper layer and at the point of observation. Conservation of angles using Snell's law, lets us to rewrite the previous

(a)

Upper layer

Ground layer

(b)

z_2

z_1

z_0

O
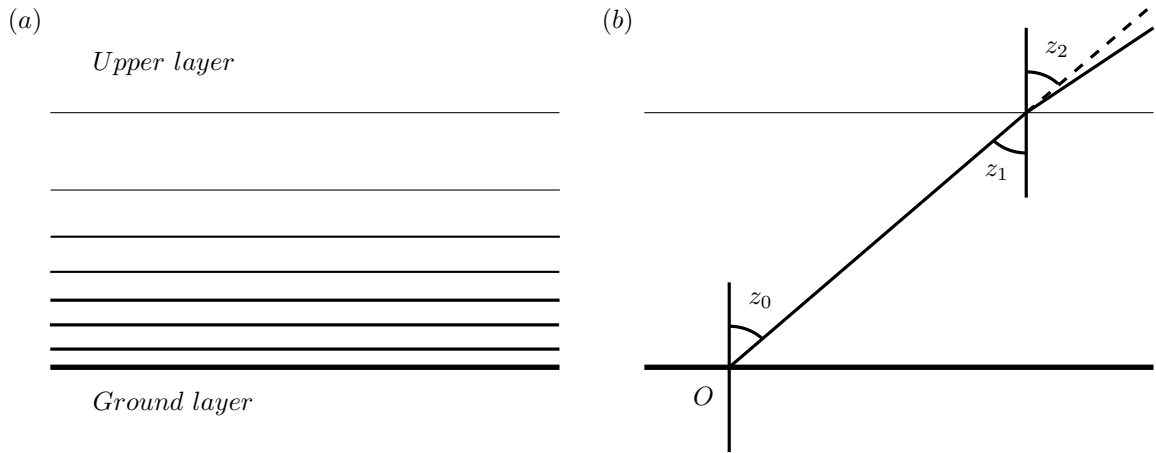
Figure 2.1: Schematic showing atmospheric refraction through plane parallel atmosphere. (a) Earth's atmosphere as a parallel layers, atmospheric pressure increases from upper to ground layer. (b) Refraction of light assuming a single homogeneous layer of atmosphere.

equation as,

$$n \sin z_0 = \sin z_2. \tag{2.2}$$

The atmospheric refraction is defined as the deviation of the light through atmosphere ζ, given by

$$\zeta = z_2 - z_0. \tag{2.3}$$

After rearranging we get,

$$z_2 = z_0 + \zeta. \tag{2.4}$$

Now putting the above equation in Eq. 2.2, we get

$$n \sin z_0 = \sin(z_0 + \zeta). \tag{2.5}$$

Using the trigonometric expansion of $\sin(A + B)$, we get,

$$n \sin z_0 = \sin z_0 \cos \zeta + \cos z_0 \sin \zeta. \tag{2.6}$$

From observation we know that, except for large zenith angles, atmospheric refraction is small, $\zeta << 1$. So we can do the approximation $\sin \zeta \approx \zeta$ and $\cos \zeta = 1$, which reduces the above equation to,

$$n \sin z_0 \approx \sin z_0 + \zeta \cos z_0. \tag{2.7}$$

After rearranging we get,

$$\zeta \cos z_0 \approx (n - 1) \sin z_0. \tag{2.8}$$

Therefore the atmospheric refraction using plane parallel model is given by,

$$\zeta_{pp} \approx (n-1)\tan z_0, \tag{2.9}$$

where $n-1$ is the refractivity at the observer and n is the refractive index of air, which is an important parameter for the calculation of atmospheric refraction. The parameters required for the calculation of refractivity of air include temperature, pressure, humidity and CO_2 content (for second order estimation). The calculation of refractive index has been studied for the past two centuries, which has lead to very accurate determination that offers a precision of 1 part in 10^8. Equation 2.9 can be rewritten using the refractivity value of 28240.48×10^{-8} for a wavelength of 574 nm, at 15° C, 1005 hPa, 80% relative humidity (RH) (Ciddor, 1996),

$$\zeta_{pp} \approx 28240.48 \times 10^{-8} \times 206265 \tan z_0 (arcsec). \tag{2.10a}$$
$$\approx 58.25 \tan z_0 (arcsec). \tag{2.10b}$$

Using the above equation atmospheric refraction at wavelength 574 nm for moderate zenith angles z_0 can be calculated. For large zenith angles, next concentric spherical shell model is discussed.

2.3.2   Concentric spherical shell model

In this section, we extend the formalism used to derive atmospheric refraction in the section 2.3.1. This model assumes that the atmosphere consists of a stack of homogeneous concentric spherical shells. Figure 2.2 shows refraction of light through the atmosphere under the concentric spherical shell model. However, Earth's atmosphere is not perfectly spherical, but this has a negligible effect on the calculation of the refraction model. With this assumption, Snell's law can be applied at the boundary layers between the shells and using the conservation of angles at each layer, we can write the refraction between space and the upper layer of the atmosphere (Left hand side of Eq. 2.11) and the observer (right hand side of Eq. 2.11)

$$nr \sin z = n_0 r_0 \sin z_0. \tag{2.11}$$

Terms in the equation include: n is the refractive index, r is the distance of shell from the center of the Earth, z is the angle between incident ray and the normal to a shell and subscript 0 indicates value of n, r and z at observer, see Fig. 2.2 (left). Next derivation of the differential equation for refraction at given layer is presented, which follows closely from Young (2004).

Differential equation for refraction

The derivation of the differential equation for the refraction follows schematic on the right side of Fig. 2.2, which shows refraction at the nth layer of the atmosphere. The path length of light traveled in this layer is given by ds, which corresponds to the increment dr from the center of the Earth C. The angle at the boundary of the layer is given by z at a distance r from C and $z + dz$ at $r + dr$. The change in the angle of the ray $d\zeta$ is not equal to dz, because the angle of the incident ray is curved by $d\theta$ (the angle at the center of the Earth) from its initial incidence angle. The deviation of the ray is given by,
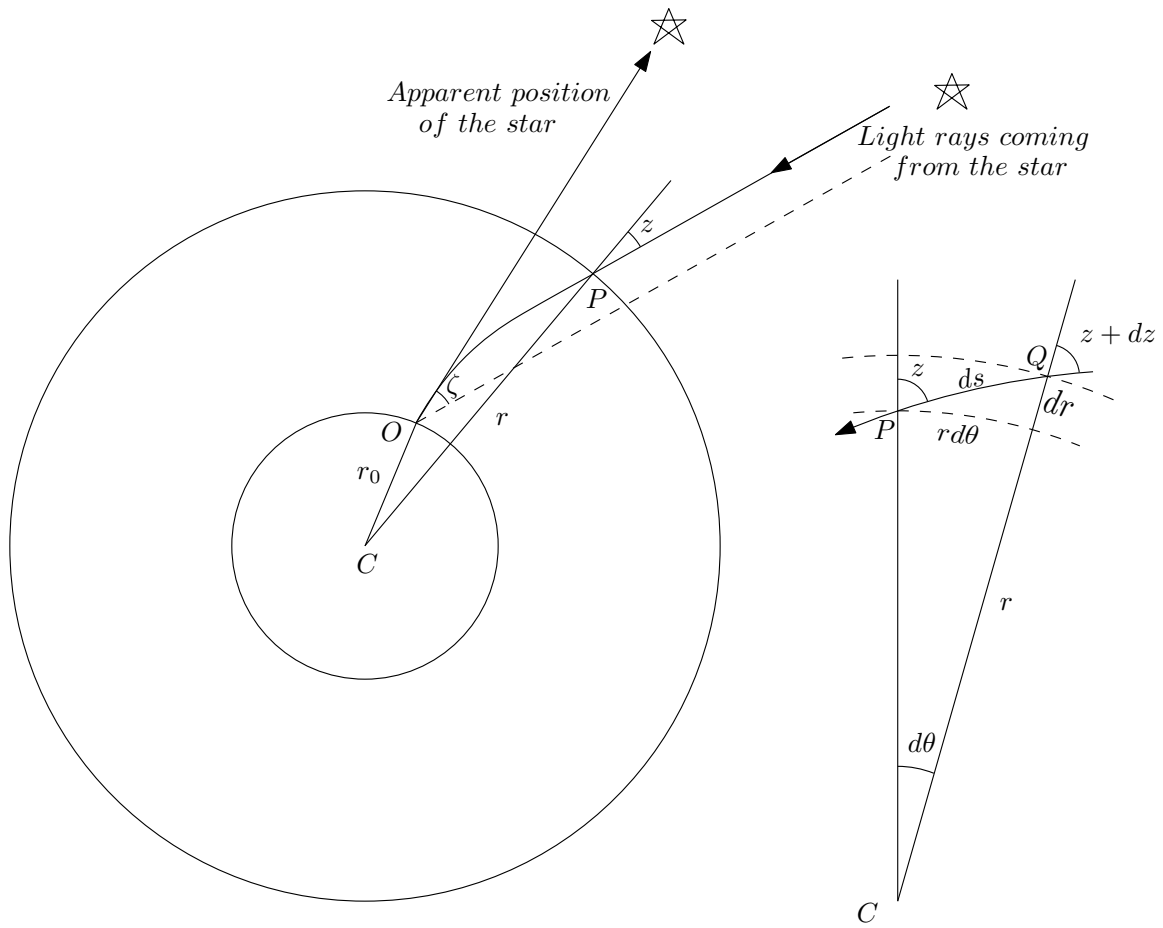
Figure 2.2: Schematic showing the propagation of light through the atmosphere under the concentric spherical shell model.

$$d\zeta = dz + d\theta. \tag{2.12}$$

After rearranging,

$$d\theta = d\zeta - dz. \tag{2.13}$$

From the differential triangle,

$$\frac{dr}{rd\theta} = \cot z, \tag{2.14}$$

after rearranging

$$\frac{dr}{r} = \frac{d\theta}{\tan z}. \tag{2.15}$$

As we saw in the section 2.3.1, refraction through layers is invariant, so we can write,

$$nr\sin z = const. \tag{2.16}$$

Taking the logarithmic differential of the previous equation,

$$\frac{dn}{n} + \frac{dr}{r} + \frac{d(\sin z)}{\sin z} = 0, \tag{2.17a}$$

$$\frac{dn}{n} + \frac{dr}{r} + \frac{\cos z}{\sin z} dz = 0, \tag{2.17b}$$

$$\frac{dn}{n} + \frac{dr}{r} + \frac{dz}{\tan z} = 0, \tag{2.17c}$$

$$\tag{2.17d}$$

Now putting the values of dr/r from Eq. 2.14 and $d\theta$ from Eq. 2.13,

$$\frac{dn}{n} + \frac{d\zeta - dz}{\tan z} + \frac{dz}{\tan z} = 0, \tag{2.18}$$

After simplifying the above equation we get,

$$d\zeta = -\frac{(\tan z)dn}{n}. \tag{2.19}$$

The refraction differential above shows what happens to refraction as the zenith angle z increases, $\tan z$ also increases and becomes infinite when observing near horizon. Now the total angular deviation, ζ of the ray falling on the telescope mirror due to atmospheric refraction can be computed by integrating all the layers between the observer and space. The equation becomes then

$$\zeta = \int_1^{n_0} \frac{\tan z}{n} dn, \tag{2.20}$$

where n_0 is the refractive index at telescope site and 1 is the refractive index of space. To compute the integral numerically, a polytropic atmosphere (a model of the atmosphere in hydrostatic equilibrium with a constant nonzero lapse rate) modeling the refractive index $n(r)$ as a function of altitude is used. Provided the refractive index $n(r)$ and dn/dr at any radial distance r from the center of the Earth, the value of ζ can be calculated from the Eq. 2.20 for any value of zenith angle z. The evaluation of the integral analytical is complicated, especially at large zenith angles.

However, the calculation of refraction is straightforward using numerical quadrature (numerical integration), except at large zenith angles when the integrand becomes very large. As recommended by Auer and Standish (2000), numerical difficulties at $z = 90°$ make it preferable to use zenith angle z itself as the variable of integration. Following the derivation in Auer and Standish (2000), Eq. 2.20 can be rewritten in terms of $\log(n)$ as,

$$\zeta = \int_1^{\log(n_0)} \tan z \, d(\log n). \tag{2.21}$$

Using the logarithmic derivation of the Eq. 2.11,

$$\log(nr) = \log(n_0 r_0 \sin z_0) - \log(\sin z). \tag{2.22}$$

Rearranging the previous equation,

$$\frac{d(\log(rn))}{dz} = -\frac{1}{\tan z} \tag{2.23}$$

Putting the above equation in Eq. 2.21

$$\zeta = -\int_1^{ln(n_0)} \frac{dz}{d(\log(rn))} d(\log n).$$
(2.24)

Further substituting equations below into Eq. 2.21

$$d(\log(rn)) = d(\log(r)) + d(\log(n)),$$
(2.25a)

$$\zeta(\log n_0) = \zeta(z_0)).$$
(2.25b)

We get,

$$\zeta = -\int_0^{z_0} \frac{d(\log n)}{d(\log r) + d(\log n)} dz$$
(2.26a)

$$= -\int_0^{z_0} \frac{\frac{d(\log n)}{d(\log r)}}{1 + \frac{d(\log n)}{d(\log r)}} dz,$$
(2.26b)

which is Equation (3) from Auer and Standish (2000). Further making the following substitutions,

$$\frac{d(\log n)}{d(\log r)} = \frac{rdn}{ndr}$$
(2.27)

We get the refractive integral, which is well behaved at $z = 90°$.

$$\zeta = -\int_0^{z_0} \frac{r\frac{dn}{dr}}{n + r\frac{dn}{dr}} dz.$$
(2.28)

The above equation of angular refraction can be evaluated using numerical quadrature by equal steps in z and calculating the values of r, $n(r)$ and dn/dr for each value of z. The value required can be obtained by solving the Eq. 2.11, by finding the root of $F(r) = 0$, when $F(r)$ is given by,

$$F(r) = nr - \frac{n_0 r_0 \sin z_0}{sinz},$$
(2.29)

where $n(r)$ is a known function of r and the values of n_0, r_0, z_0 and z are all known. The root can be evaluated numerically using Newton-Raphson method (Ypma, 1995),

$$r_{i+1} = r_i - \frac{F(r_i)}{F'(r_i)}$$
(2.30a)

$$= r_i - \left[\frac{n_i r_i - n_0 r_0 \frac{\sin z_0}{\sin z}}{n_i + r_i \frac{dn_i}{dr_i}} \right]$$
(2.30b)

The convergence of the above equation is rapid and only requires four steps. In the next section, we will discuss the model of the atmosphere, which is required to derive the radial variation of refractive index and its derivative.

2.3.3   Model of the atmosphere

Garfinkel (1944, 1967) in the past have provided a polytropic piecewise model of the atmosphere. Here the same model of the atmosphere is discussed provided by (Sinclair, 1982) and (Hohenkerk and Sinclair, 1985), the results from the same model are discussed, a full description of the model is beyond the scope of this chapter. The physical assumptions made in the model for the Earth's atmosphere is as follows:

1. The temperature decreases at a constant rate with the elevation until the troposphere and then above the temperature remains constant (in the stratosphere).

2. Perfect gas law, for mixture of dry air and water vapor, and for the dry air and water vapor separately.

3. Hydrostatic equilibrium of the atmosphere.

4. Constant relative humidity in the troposphere, equal to its value at the observer.

5. The Gladstone–Dale relation, $n - 1 = a\rho$, which relates the refractive index n and the density ρ, where a is a constant which depends only on the local physical properties of the atmosphere.

The following parameters are required to describe the variation of temperature and pressure:

z_0 the observed zenith angle

h height of observer above the geoid (m) (see level)

ϕ latitude of observer

h_t height of tropopause above geoid(m) ($\approx 11,000$ m)

h_s height at which refraction is negligible (space, say $80,000$ m)

P_0 total atmospheric pressure at observer (mb)

P_{w0} partial pressure of water vapor at observer (mb), given by $P_{w0} = RH(T_0/247.1)18.36$ (RH is relative humidity)

T_0 temperature at observer (K)

α temperature lapse rate K°/m (≈ 0.0065)

δ exponent of temperature dependence of water vapor pressure, typical value $18 - 21$.

λ wavelength of light in μm

Constants:

i) Universal gas constant: $R = 8314.32 \, J/(moleK)$

ii) Molecular weight of dry air: $M_d = 28.9644 \, g/mole$

iii) Molecular weight of water vapor: $M_w = 18.0152 \, g/mole$

iv) Acceleration due to gravity, $\bar{g} = 9.78(1 - 0.0026\cos 2\phi - 0.00000028h)$

Calculated values using constants defined above:

i) Total height of the observer: $r_0 = 6378120 + h_0$.

ii) Total height of the troposphere: $r_t = 6378120 + h_t$.

iii) Total height of the stratosphere: $r_s = 6378120 + h_s$.

iv) $\gamma = \bar{g}M_d/(R\alpha)$

v) $A = \left(287.604 + \frac{1.6288}{\lambda^2} + \frac{0.0136}{\lambda^4}\right)\frac{273.15}{1013.25}$

The equations for total pressure, water vapor pressure, temperature, refractive index n and dn/dr in the troposphere ($r_0 < r < r_t$), are given below,

Temperature variation in the troposphere is given by,

$$T = T_0 - \alpha(r - r_0). \tag{2.31}$$

Water vapor pressure as a function temperature in the troposphere is given by,

$$P_w = P_{w0}(T/T_0)^\delta. \tag{2.32}$$

Pressure as a function of constants discussed previously,

$$P = \left[P_0 + \left(1 - \frac{M_w}{M_d} \right) \frac{\gamma}{\delta - \gamma} P_{w0} \right] \left(\frac{T}{T_0} \right)^\gamma - \left(1 - \frac{M_w}{M_d} \right) \frac{\gamma}{\delta - \gamma} P_w. \tag{2.33}$$

Refractive index,

$$n = 1 + 10^{-6}(AP - 11.2684 P_w)/T. \tag{2.34}$$

Derivative of refractive index,

$$\frac{dn}{dr} = -\frac{(\gamma - 1)\alpha A 10^{-6}}{T_0^2} \left[P_0 + \left(1 - \frac{M_w}{M_d} \right) \frac{\gamma}{\delta - \gamma} P_{w0} \right] \left(\frac{T}{T_0} \right)^{\gamma - 2} \tag{2.35}$$

$$+ \frac{(\delta - 1)\alpha 10^{-6}}{T_0^2} \left[A \left(1 - \frac{M_w}{M_d} \right) \frac{\gamma}{\delta - \gamma} + 11.2684 \right] P_{w0} \left(\frac{T}{T_0} \right)^{\delta - 2}. \tag{2.36}$$

Now the above expressions for total pressure, water vapor pressure, temperature, refractive index n and dn/dr in the stratosphere $(r > r_t)$, are given by:
Temperature,

$$T = T_t \ (constant). \tag{2.37}$$

Water vapor pressure,

$$P_w = 0. \tag{2.38}$$

Pressure,

$$P = P_t \exp \left[-\frac{\bar{g} M_d}{R T_t} (r - r_t) \right]. \tag{2.39}$$

refractive index,

$$n = 1 + (n_t - 1) \exp \left[-\frac{\bar{g} M_d}{R T_t} (r - r_t) \right]. \tag{2.40}$$

Derivative of refractive index,

$$\frac{dn}{dr} = -\frac{\bar{g} M_d}{R T_t} (n_t - 1) \exp \left[-\frac{g M_d}{R T_t} (r - r_t) \right]. \tag{2.41}$$

The derivative of the refractive index in the troposphere is given by Eq. 2.36 and in the stratosphere by Eq. 2.41. These derivatives are then used to evaluate the refractive integral given by the Eq. 2.28, which is discussed next.

2.3.4   Numerical evaluation of the refraction integral

The model of the atmosphere discussed in the previous section has a discontinuity in the temperature gradient at the boundary of troposphere and stratosphere. So it requires the evaluation of the integral from Eq. 2.28 in two steps, in the troposphere and the stratosphere separately. The limits of the integral at the boundary of the two layers are then $z = z_s$ and z_t in the stratosphere, and from $z = z_t$ and z_0 in the troposphere, defined by

$$z_t = \arcsin\left(\frac{n_0 r_0 \sin z_0}{n_t r_t}\right),$$ (2.42)

and

$$z_s = \arcsin\left(\frac{n_0 r_0 \sin z_0}{n_s r_s}\right).$$ (2.43)

As shown by (Hohenkerk and Sinclair, 1985), 32 and 128 steps are required respectively in the troposphere and stratosphere to achieve a 0.01 arcsec precision in atmospheric refraction at $60°$ zenith angle. The next section will compare the plane-parallel and the concentric spherical shell model.

2.4   Comparison between both refraction models

The calculation of the angular refraction varies greatly for both refraction model. For the plane-parallel model, a very accurate value of refractivity at the observer is required to calculate the refraction. While for the concentric spherical shell model, an accurate model of the atmosphere is required. Though both models differ greatly, the calculation is very dependent on local atmospheric parameters: temperature, pressure, humidity and CO_2 content.

Table 2.1 shows the comparison for the calculation of the angular refraction for various zenith angles using the plane-parallel and the spherical shell models. As can be seen from the table, for small values of zenith angles, both models give similar results but results differ significantly at large zenith angles. The value of the refractivity $(n-1)$ used for the plane-parallel model is 28240.48×10^{-8} (Ciddor, 1996) for a wavelength of 574 nm, at $15°$ C, 1005 hPa, 80% RH. The next section discusses the theoretical calculation of atmospheric refraction for the Subaru Telescope at Maunakea, which will be compared to the measured on-sky values of refraction.

2.5   Atmospheric dispersion calculation for the Maunakea site

For on-sky measurements of the dispersion, we utilize y-H band (working wavelength of our internal NIR camera is $0.9 - 1.65~\mu m$), so to compare it accordingly, a theoretical calculation of the dispersion, which is the difference of refraction angle ζ between $0.9~\mu m$ and $1.65~\mu m$ is adopted. For this purpose, a dispersion model calculated by Olivier Guyon (Guyon et. al. in prep.) was used. It has a 10^{-8} accuracy in refractive index, and improves over previously reported values of refractivity. The model is superior to previous dispersion models because it accounts for the water absorption in the near-infrared and the effect of gases other than CO_2 in the atmosphere. The source code for the model can be found on his Github page. Table 2.2 presents angular refraction and

Table 2.1: Atmospheric refraction comparison between two models: plane-parallel and concentric spherical shell model (at sea level) (Spanò, 2014).

Zenith angle (degree)	Plane-parallel (arcsec)	Spherical shell (arcsec)
0	0.00	0.00
10	10.28	10.26
20	21.22	21.19
30	33.67	33.61
40	48.93	48.82
50	69.49	69.29
60	101.00	100.52
70	160.21	158.65
80	330.70	319.18

dispersion calculation for wavelengths of 0.9 and 1.65 μm. The table presents values of atmospheric dispersion as a function of zenith angle and varying atmospheric conditions. The values of zenith angles and atmospheric parameters presented in the table were recorded from on-sky observation using Subaru Telescope on the night of Dec. 13th, 2016.

The calculation of a look-up table consisting atmospheric dispersion values, as discussed in the beginning of this chapter, uses similar calculation as presented in the Table 2.2 except the values of atmospheric parameters are constants (depending on the telescope site).

Table 2.2: Atmospheric dispersion calculation in y-H ($0.9 - 1.65$ μm) band for Maunakea site.

Zenith angle (degree)	T (°C)	P (mbar)	RH (%)	ζ at 0.9 μm (arcsec)	ζ at 1.65 μm (arcsec)	Dispersion (mas)
4.57	0.7	618.0	8.6	2.950610	2.936147	14.463
9.12	0.7	617.9	7.5	5.925797	5.896751	29.046
14.29	0.8	617.9	7.4	9.401791	9.355707	46.084
22.85	0.5	617.7	7.9	15.551862	15.475633	76.229
23.78	0.7	617.8	7.2	16.261851	16.182142	79.709
27.15	0.6	617.7	7.4	18.924584	18.831824	92.759

2.6 Conclusion

Estimating the amplitude of atmospheric dispersion requires computing angular refraction as a function of wavelength. Angular refraction for different wavelengths can be calculated by using six local parameters: zenith angle (observation angle), altitude, latitude, temperature, pressure, humidity and CO_2 content. Theoretical models currently used for atmospheric dispersion correction are indeed precise enough for the requirements stipulated in the introduction of this chapter, however, these models are limited by the precision of the environmental parameters that are input into them. As an example, the atmospheric dispersion in H-band for Maunakea site (T=270K, P=614 mbar, RH=48%, CO_2=400 ppm) at a telescope elevation of $60°$ is 16.59 mas and it changes by 0.06 mas for a 1 K change and 0.6 mas for 10% change in RH. For ADC correction based on a look-up table, a change in temperature and RH can over- or under-compensate atmospheric dispersion.

For a very precise correction of dispersion, solely relying on the theoretical calculation is not good enough. The aim of this thesis is not to go into the details of the theoretical modeling of atmospheric refraction, but to present a technique that measures the residual dispersion in the science image after the look-up table based correction is applied, and correct this residual dispersion in closed-loop by driving the ADC. The next chapter discusses the concept behind the measurement of dispersion in the science image.

Measuring Atmospheric Dispersion

3.1 Introduction

In the last chapter, I discussed how atmospheric dispersion affects high-contrast coronagraphy, theoretical models used for calculating look-up table of atmospheric dispersion and their shortcomings. This chapter discusses, how to measure the presence of atmospheric dispersion in the final science image and its correction. First, image formation by a telescope is briefly described, then I discuss simulation of the PSF with WFE. After establishing the prerequisites, the concept behind the dispersion measurement is discussed. For verification of the concept, simulations were carried out, as explained in the section 3.3.1. Next, the dispersion measurement algorithm is established with the aid of simulations. And I conclude the chapter by providing the framework for calibration and correction of on-sky dispersion by an ADC.

3.2 Image formation by a telescope

The formation of an image $I(r)$ by a telescope with an unobstructed circular pupil of diameter D, at wavelength λ, is given by the Airy function (Born and Wolf, 1999),

$$I(r) = k \left[\frac{2J_1(r)}{r} \right]^2.$$

(3.1)

Here J_1 is the Bessel function of the first kind, order one, k is a normalization constant, and $r = D/2$ the telescope aperture radius (primary mirror). The angular radius of the dark ring that borders the Airy disk is $1.22\lambda/D$. The theoretical optimal resolution for the telescope is given by $1\lambda/D$, i.e. the smallest angular separation that allows us to distinguish two objects.

For simulations, Fourier transformation (FT) is used to propagate light to the focal plane to generate the PSF. An analytical FT is briefly discussed in the next section and its implementation is discussed in detail in later sections.

3.2.1 Fourier transform

The FT of a function $f(x,y)$ in 2-d Cartesian coordinates having two independent variables x and y is given by $F(u,v)$ such as (Goodman, 2005)

$$F(u,v) = \int \int_{-\infty}^{\infty} f(x,y)e^{-j2\pi(ux+vy)}dx\,dy$$

(3.2)

where u and v are spatial frequencies in x and y directions. This operation is often described in a shorthand manner as $\Im\{f(x,y)\} = F(u,v)$. Similarly, the analytic inverse FT is given by

$$f(x,y) = \int \int_{-\infty}^{\infty} F(u,v)e^{j2\pi(vx+uy)}du \, dv. \tag{3.3}$$

The shorthand notation for this operation is $\Im^{-1}\{F(u,v)\} = f(x,y)$. For the FT to be realizable, Eq. 3.2, f(x,y) must satisfy certain common conditions:

- f must be absolutely integrable over the infinite range of x and y;

- f must have only a finite number of discontinuities; and

- f must have no infinite discontinuities.

Fourier integral for a telescope

The diffraction limited image in the focal plane of any telescope with a circular aperture P is given by the square modulus of the FT of the complex amplitude of the pupil $P * e^{i\phi}$, i.e.

$$I(r,\phi) = \frac{k}{\pi^2} \left[\int_0^1 d\rho \int_0^{2\pi} d\theta \rho e^{i\phi(\rho,\theta)} e^{-i\pi r\rho \cos(\theta-\phi)} \right]^2, \tag{3.4}$$

where $\{r,\phi\}$ and $\{\rho,\theta\}$ are the radial coordinates, respectively in the image and the pupil plane. The phase component ϕ of the complex amplitude of the pupil describes the deviation of the wavefront from the ideal case, i.e. the WFE, and can usually be decomposed on a basis of orthogonal modes such as Zernike functions. At first order, the WFE is usually independent of the wavelength, but the resulting phase ϕ is scaled by a chromatic $2\pi/\lambda$ factor such as

$$\phi = \frac{2\pi}{\lambda}WFE. \tag{3.5}$$

Diffraction integral expressions are difficult to solve analytically except for a few simple aperture functions. Since it is impossible to simulate the infinite integral required for the FT, we usually use Discrete Fourier transform (DFT) techniques that integrate over a finite range of coordinates. The Fast Fourier Transform (FFT) is such a method, allowing fast computations. Since telescope pupils have generally finite boundaries, they are well suited for discretization. DFT implemented as a FFT provides an efficient framework to compute these integral for complex apertures numerically in a simplified and fast manner, which is discussed in the next section.

3.2.2 PSF simulation

In order to compute the PSF of a telescope, the FT of the telescope pupil is performed. For the FT relationship to hold between the pupil and image planes, paraxial optics are considered with error terms associated with Fresnel propagation. For an unobstructed pupil, the telescope aperture function can be expressed in polar coordinates as

$$P(r) = \begin{cases} 1 & if \ r < D/2 \\ 0 & otherwise \end{cases}. \tag{3.6}$$
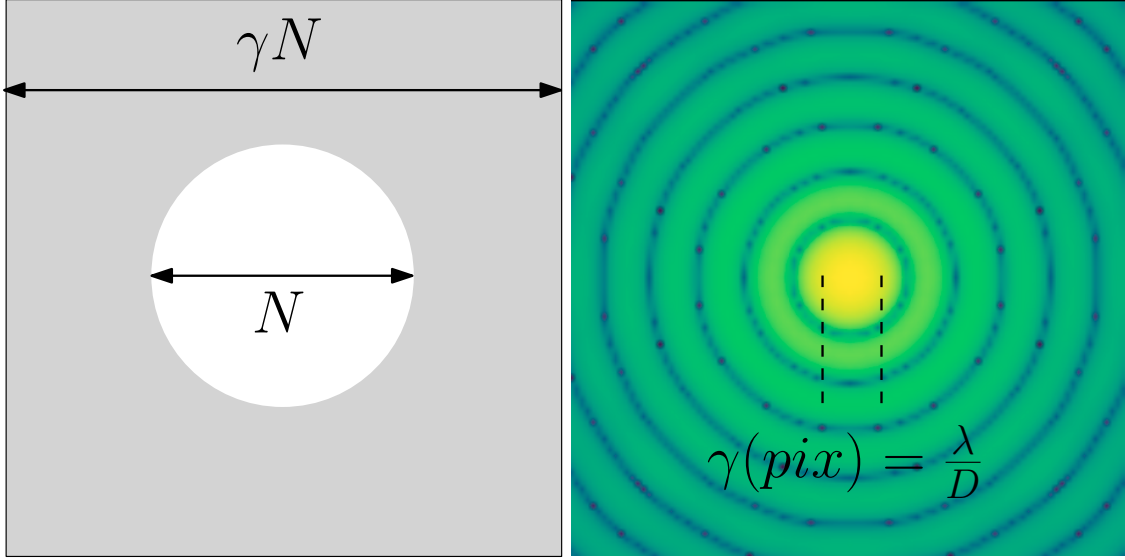
Figure 3.1: Sampling relationship between pupil (left) and image (right) plane using FFT. Left: pupil plane with a sampling of N pixels across the pupil with γN pixels for the pupil plane. Right: PSF corresponding to the pupil in left, each pixel in the image plane corresponds to $= \lambda/(\gamma D)$, where γ is the padding factor.

The image formed in the focal plane can be written as the square modulus of the FT of the telescope pupil function, which is given by $|\Im\{P(r)\}|^2$.

The following notations are adapted from Soummer et al. (2007a). Since the pupil function is centro-symmetric, the above computation of the FT in two dimensions can be broken into one dimension without loss of generality. Here we consider a 1D function $f(x)$ with $x \in [-\gamma D/2, \gamma D/2]$ and $f(x) = 0$ for $|x| > D/2$, where γ is a padding factor related to the resolution of the FT in the focal plane as shown in Fig. 3.1: the more padding is considered around the pupil, the better the sampling is in the image plane. Similar to a 2D FT integral given in Eq. 3.2, the FT of the function above can be written as an integral over finite boundaries

$$\hat{F}(u_k) = \int_{-\gamma D/2}^{\gamma D/2} f(x)e^{-i2\pi x u_k}dx, \tag{3.7a}$$

with u_k the pixel coordinates in the image plane. This integral can be discretized using a Riemann sum such as

$$\hat{F}(u_k) \approx \delta x \sum_{n=0}^{N-1} f(x_n)e^{-i2\pi x_n u_k}, \tag{3.8a}$$

where $x_n = (n - \gamma N/2)\delta x$, $n \in [0, \gamma N - 1]$, corresponding to the sampling points of $f(x)$, and $u_k = (k - \gamma N/2)\delta u, k \in [0, \gamma N - 1]$ are the sampled values of the FT. Since γN is the number of pixels sampling the pupil plane, γN is also the number of pixels sampling the image plane. Under the Riemann sum approximation, different sampling can be chosen for the pupil and image plane. In the case of same sampling is used in both the planes $= \gamma N$, the integration steps reduce to

$$\delta x \delta u = \frac{1}{N}. \tag{3.9}$$

The Riemann sum as shown in Eq. 3.8a is then,

$$\hat{F}(u_k) = \frac{\gamma D}{N}(-1)^{N/2-k} \sum_{n=0}^{N-1} (-1)^n f(x_n) e^{-i2\pi kn/N},$$ (3.10)

where the Riemann sum is now a DFT, which can be computed very efficiently using FFT algorithms. The constraint for using FFT comes from a fixed relationship between the focal and image plane sampling and the padding factor, forced by Eq. 3.9. The relationship between pupil and image plane is given by,

$$\delta u = \lambda/(\gamma D),$$ (3.11)

which is explained by the Fig. 3.1, using resolution corresponding to the wavelength and diameter of the pupil.

Monochromatic PSF

For calculating the PSF of an unobstructed telescope with an 8-m diameter for a single wavelength of 1μm, the sampling (number of pixels) across the pupil must be chosen first. The sampling number should be high enough to capture the high-frequency features such as the secondary mirror and its support structure (spiders). Usually, the sampling for a real telescope with a support structure is N$= 300 - 400$. The padding factor γ is calculated based on the telescope resolution for a particular wavelength and required plate scale in the image plane, as explained by the Eq. 3.11. As an example, the telescope resolution at 1 μm for a telescope diameter of 8 m is given by,

$$\Re = \frac{\lambda}{D}$$ (3.12a)

$$= \frac{1 \times 10^{-6}}{8} \ (radian)$$ (3.12b)

$$= 0.125 \times 10^{-6} \ (radian)$$ (3.12c)

$$\Re = 25.78 \ mas$$ (3.12d)

In the image plane, 1 pixel corresponds to $\lambda/(\gamma D)$. For the monochromatic PSF simulation ($\lambda = 1\mu$m and $D = 8m$) as shown in the Fig. 3.2, the plate scale of the image is chosen to be 1 mas/pixel. So the padding for the simulation will be equal to the telescope resolution.

Polychromatic PSF

The simulation of a polychromatic PSF can be done in a similar manner to the simulation of monochromatic PSF. A particular wavelength band can be sampled into a finite (small) number of discrete wavelengths. Monochromatic PSFs are then simulated for each discrete wavelength by varying the padding factor γ for a fixed plate scale in the image plane.

After calculating the monochromatic PSFs for all the wavelengths, polychromatic PSF is calculated by taking an average by superposition of all monochromatic PSFs. The result of such a simulation is shown in Fig. 3.4. The polychromatic PSF corresponds to H-band PSF for Subaru Telescope with a plate scale of 16.7 milliarcsecond/pixel.
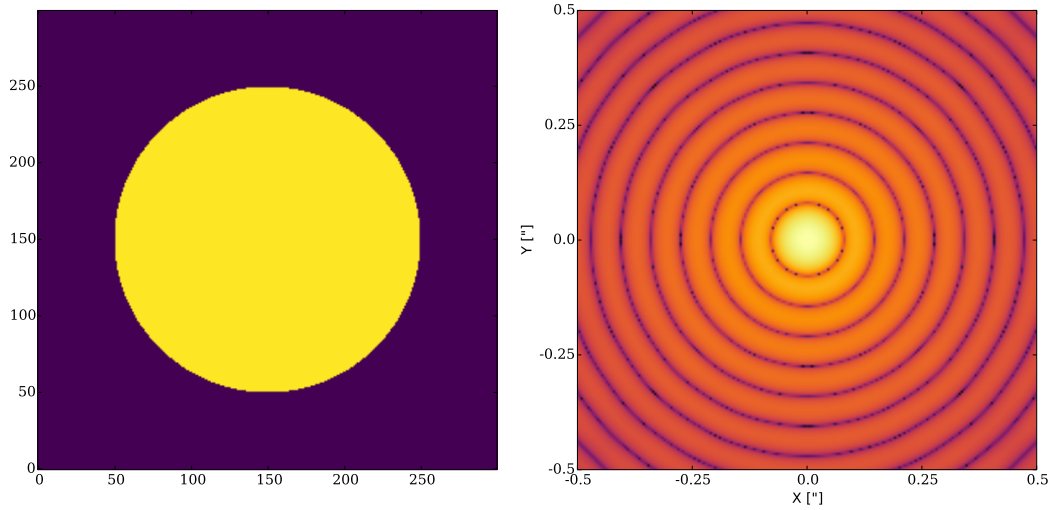
Figure 3.2: Monochromatic PSF simulation corresponding to an unobstructed 8 m telescope at a wavelength of 1 μm. Left: telescope pupil with a sampling of N = 200 across the pupil. Right: resulting PSF using a padding factor $\gamma = 25.78$.

3.2.3   Subaru telescope's PSF

To calculate the PSF delivered by the Subaru Telescope, the actual telescope pupil geometry was utilized. The Subaru Telescope beam has a central obstruction (due to the secondary mirror) and 4 spiders vanes (due to the support structure for the secondary mirror). The pupil geometry, as measured from an image acquired on the telescope, is shown in Fig. 3.3. The parameters estimated from the telescope pupil are; pupil diameter: 7.92223 m, spider thickness: 224 mm, central obstruction: 2.285 m and spider angle: $\beta = 51.75°$. The measured parameters here were taken into consideration while simulating the pupil for the Subaru Telescope.

Figure 3.4 shows the theoretical H-band PSF simulated using the geometry described above. For the simulation, sampling across the pupil was chosen to be N= 300 to get a sufficient sampling for the telescope spiders. The padding factor γ changes for each wavelength across the H-band $(1.5 - 1.8 \ \mu$m) depending on the number of steps used for the simulation. Suppose 20 steps were taken to calculate the H-band PSF with the required plate scale of 16.7 mas/px, the γ will change from $\Re_{1.5\mu m}/16.7$ to $\Re_{1.8\mu m}/16.7$ in 20 steps. Where $\Re_{1.5\mu m}$ and $\Re_{1.8\mu m}$ are the telescope resolution at wavelengths of, $\lambda = 1.5 \ \mu$m and 1.8 μm respectively.

3.2.4   Adding wavefront error to the simulations

The simulations presented above considered no WFE in the pupil, i.e. a constant phase. WFE can be added in simulations simply by adding the phase component ϕ in the complex amplitude of the pupil image. In this section, we will discuss the addition of two specific type of WFE, tip/tilt (or pointing of the telescope), and diffraction from a sine-wave function.

The tip-tilt function discussed here follows the notation and derivation from (David, 2011). If we assume a tilt of α is applied to a wavefront, as shown in the Fig. 3.5 (a), where the dashed line
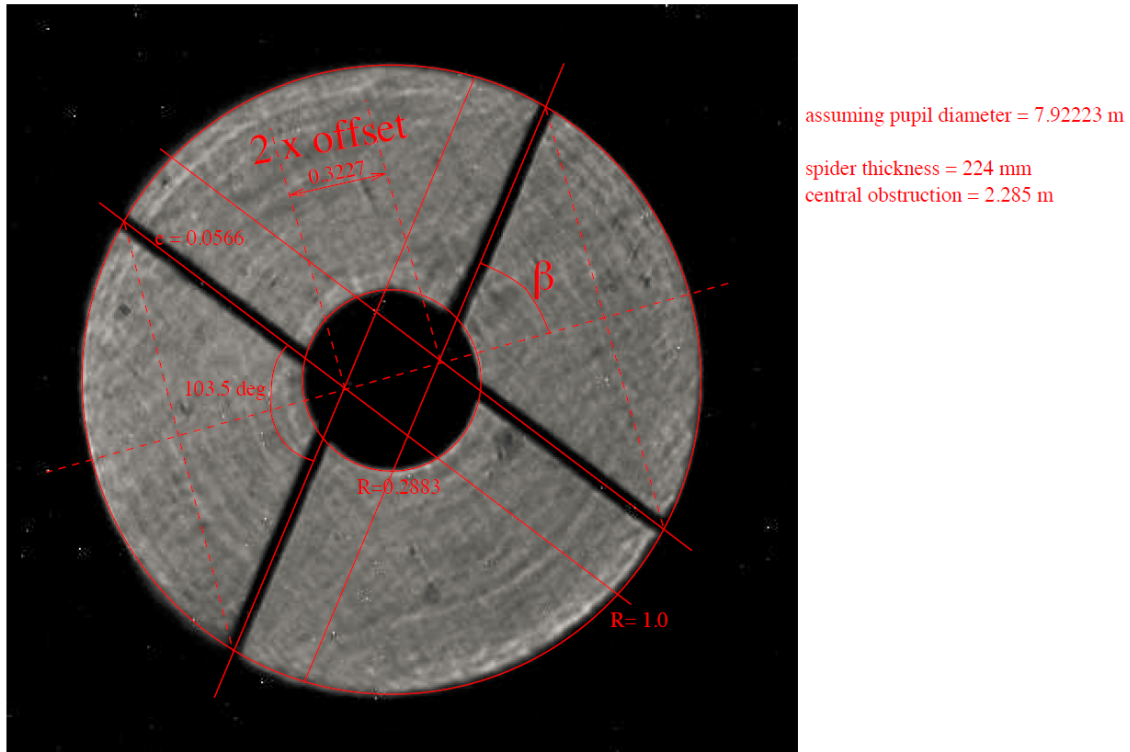
Figure 3.3: Subaru Telescope pupil geometry, showing the outer radius corresponding to the primary mirror and an inner radius indicating the size of the secondary mirror obstruction with support structures (telescope spiders).

represents the tilted wavefront of the beam and the arrow indicates the direction of propagation. The equation of the dashed line is given by,

$$z = -ky\tan\alpha. \tag{3.13}$$

The Eq. 3.13 for a tilt of angle α (pointing error of α along the y direction), the phase error is simply given by

$$\phi_Y(x,y) = ky\tan\alpha. \tag{3.14}$$

Were k is the wavenumber ($k = 2\pi/\lambda$). More generally, for a pointing (or tip/tilt) error of amplitude α and oriented with an angle θ in the $x - y$ coordinates of the pupil, the phase is then

$$\phi(x,y) = k(x\cos\theta + y\sin\theta)\tan\alpha \tag{3.15}$$

The expression for the phase front as given by Eq. 3.15 can be integrated into the pupil function $P(r)$. The complex pupil function for a tip/tilt is then given by

$$P'(x,y) = P(x,y) \times \exp\left[jk(x\cos\theta + y\sin\theta)\tan\alpha\right]. \tag{3.16}$$

The PSF can be diffracted in a similar manner to adding tip/tilt, as discussed previously by introducing a sine wave in the phase of the complex amplitude of the pupil, it acts as a diffraction grating that creates speckles around the central PSF. The pupil function can be expressed as,
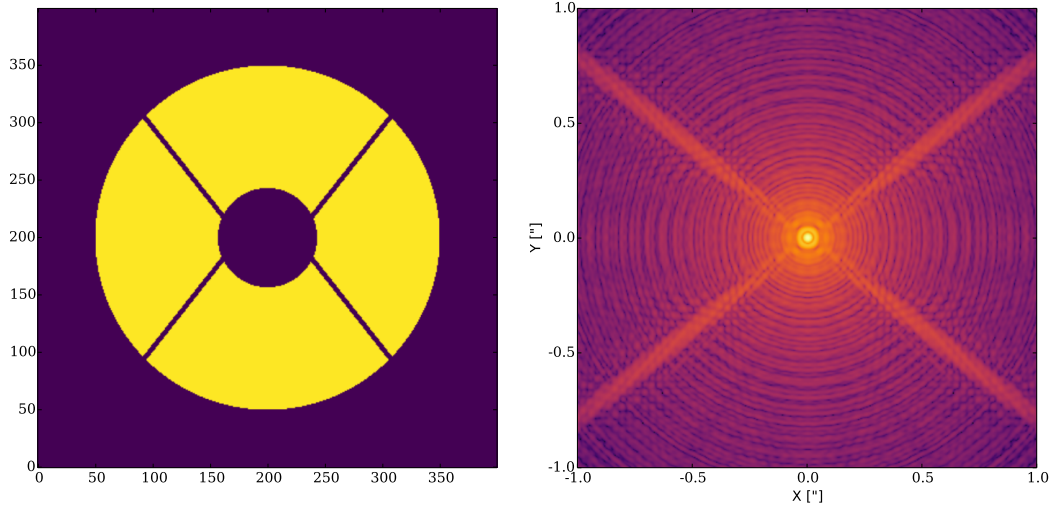
Figure 3.4: H-band PSF simulation corresponding to the Subaru telescope. Left: Subaru Telescope pupil geometry with a sampling of N = 300 across the pupil. Right: H-band PSF corresponding to the pupil geometry shown in the left and plate scale in the image is 16.7 mas/pix matching the sampling of the internal NIR of SCExAO.

$$P'(x,y) = P(x,y) \times \exp\left(jkg_x g_y\right), \tag{3.17}$$

where p, g_x and g_y are

$$p = telescope\_diameter/CPA \text{ (period of sine wave)} \tag{3.18a}$$
$$g_x = \sin(2\pi x/p) \text{ (sine wave in } x-\text{axis)} \tag{3.18b}$$
$$g_y = \sin(2\pi y/p) \text{ (sine wave in } y-\text{axis)}. \tag{3.18c}$$
$$\tag{3.18d}$$

Where *CPA* is the number of cycles per aperture (CPA) across the pupil. As CPA increases, the speckles separation from the main PSF core also increases (similarly to a transmission grating, where a higher number of lines increases the grating diffraction angle). After establishing the prerequisites, the next section discusses the concept of the measurement of dispersion in the PSF using satellite speckles.

3.3 Concept behind the measurement of dispersion

The concept behind the measurement of dispersion utilizes the chromatic scaling of speckles in the focal plane, explained with the aid of the schematic in Fig. 3.6. It features a visible broadband PSF (blue, green and red) with conveniently placed symmetric off-axis diffraction features (speckles). The speckles are generated by diffracting the PSF horizontally and vertically in a similar manner to diffraction with or by a grating. Unlike the core of the PSF, off-axis diffraction features are
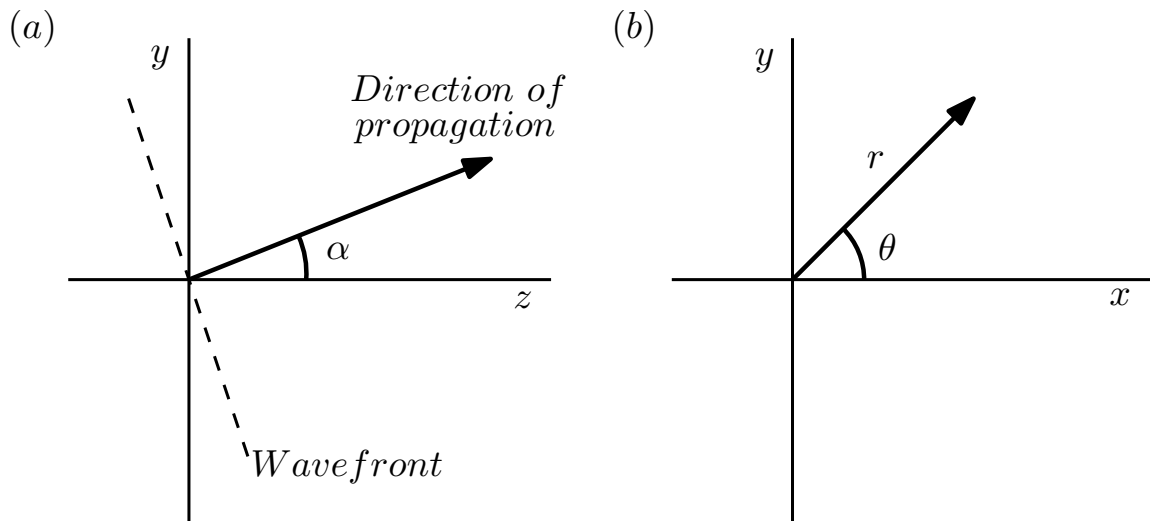
Figure 3.5: Schematic showing propagation of wavefront. (a) This schematic corresponds to the situation when the wavefront falls on the primary mirror of the telescope at an angle of α, the direction of propagation is shown by the arrow. (b) Schematic showing direction of tilt in pupil $(x - y)$ plane by angle θ..

wavelength dependent and appear spectrally dispersed, longer wavelengths (red) diffract more compared to shorter wavelengths (blue), as shown in the Fig. 3.6. In the next paragraph, I show how speckles are affected by the presence of dispersion in the PSF. In the case of the PSF with no dispersion (corresponding to a pointing of the telescope at zenith), all the wavelengths (blue, green and red) are co-focused at a single location. The speckles are dispersed radially away from the PSF, pointing towards its location. Hence, by extrapolating the direction of a given speckle as a function of wavelength, it is possible to determine the location of the PSF when there is no dispersion present (cf. Fig. 3.6 (a)). The location where the speckles seem to radiate from is called the radiation center, which coincides with the PSF core in the absence of dispersion (cf. Fig. 3.6 (a)). When the PSF is affected by the presence atmospheric dispersion, the speckles no longer radiate from the PSF core (cf. Fig. 3.6 (b)), but from the radiation center, offset from the PSF core. The offset of the radiation center from the PSF core is directly proportional to the presence of dispersion in the PSF. The relationship between the amount of dispersion to the deviation of the radiation center from the PSF core can be established by an empirical relationship, which is discussed in section 3.3.2. After establishing the relationship, the amount of dispersion present in the PSF can be estimated by measuring the distance between the radiation center and the PSF core. The next section presents simulation of the atmospheric dispersion in a PSF to verify the concept explained here.

3.3.1 Atmospheric dispersion simulation

In this section, I will describe the simulations of atmospheric dispersion with the Subaru Telescope pupil that I performed using the tools described above. The dispersion can be simulated using two methods. Both methods rely on a discretization of the band into a small number of wavelengths and taking the average of the resulting images, as described in Sec. 3.2.2.

The dispersion can be introduced in the PSF in two ways, first: in the form of tilt as a phase in the telescope pupil, second: shifting the monochromatic PSFs in the image plane. Both techniques
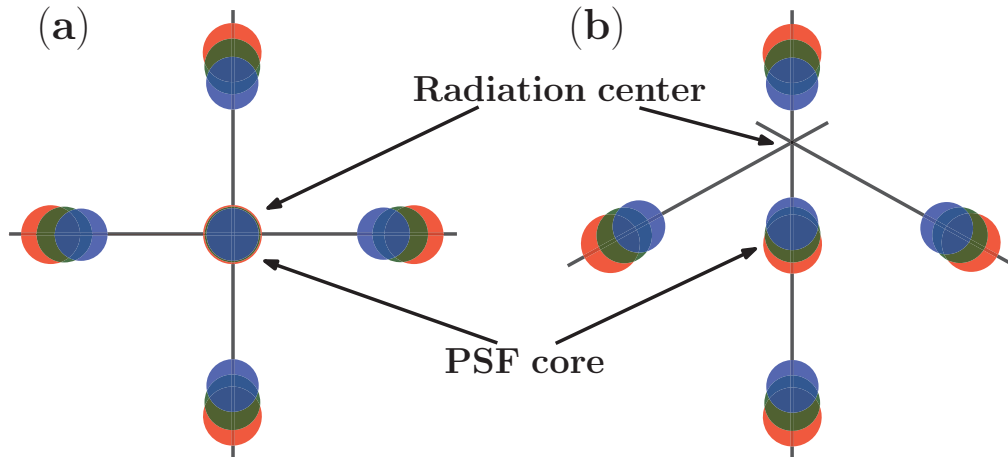
Figure 3.6: Concept of the measurement of atmospheric dispersion: The on-axis PSF is diffracted to generate speckles. (a) No dispersion, each wavelength is focused at the same point on-axis, and the lines joining the diffracted speckles meet at the PSF core. (b) With atmospheric dispersion, the different wavelengths are no longer focused at a point, and the lines joining the diffracted speckles meet at the radiation center.

require computation for individual wavelengths and adding dispersion in an incremental manner and then taking an average to produce a polychromatic PSF with dispersion. Below both techniques are described as follows:

- The first method adds a tip/tilt WFE for each individual wavelength before the FFT. For each individual wavelength, a tip/tilt angle α is added using Eq. 3.16, so that the difference for the extreme wavelengths correspond to the desired dispersion. For example, a 50 mas of dispersion, the range of tip/tilt will be, α in $[-25\ mas,\ 25\ mas]$ and direction of dispersion is controlled by θ.

- The second method shifts the individual simulations after FFT. Each wavelength is simulated with a perfect wavefront, and shifted with a sub-pixel precision, again so that the difference in position for the extreme wavelength corresponds to the desired dispersion.

To perform a measurement of the dispersion as explain in Sec. 3.3, I also add satellite speckles in the image, using Eq. 3.17. Low-amplitude sinusoidal modulations were added to the pupil to produce pairs of off-axis speckles along the diagonals of the x and y axes. The result of such a simulation is presented in the Fig. 3.7. It shows a H-band simulation for the Subaru Telescope geometry with satellite speckles. Due to the chromatic nature of satellite speckles, they appear elongated and present a low-resolution spectra in the H-band. Figure 3.7 (a) presents the case without dispersion, and the spectrally dispersed off-axis speckles appear to radiate from the core of the PSF. In panel (b), a 50 *mas* dispersion is simulated in the PSF. The radiation center clearly does not overlap with the PSF core anymore.

The simulation shown in the Fig. 3.7 does indeed confirm the concept explained in section 3.3. The presence of dispersion in the PSF can be measured by establishing an empirical relationship between the deviation of the radiation center from the PSF core and amount of dispersion in the PSF. In an ideal case, the location of the radiation center can be estimated by fitting lines to speckles
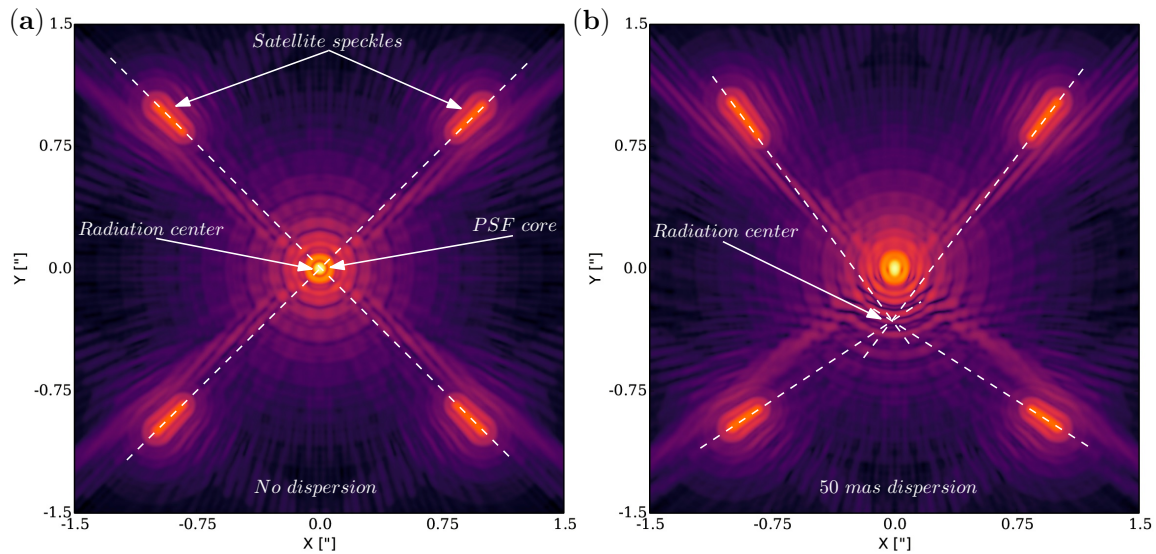
Figure 3.7: Simulated H-band PSF with artificial satellite speckles: (a) With no atmospheric dispersion, i.e. telescope pointing at zenith, speckles point to the PSF shown by over-plotted lines. (b) PSF with 50 mas atmospheric dispersion in the vertical direction.

and finding their intersection. But in practice, on-sky speckles suffer from various WFE and water absorption between y- and H-band, which is discussed in detail in section 5.3.1. So fitting line to speckles does not provide a reliable measurement of the radiation center on-sky. To find the precise location of the radiation center, an algorithm was developed, which is discussed in the next section.

3.3.2 Extracting atmospheric dispersion

In order to estimate the amount of residual dispersion in a given image, the distance between the core of the PSF and the radiation center must be measured precisely. Even with some prior knowledge, the careful mapping of non-symmetric structures is a non-trivial task in practice. I have however empirically developed an algorithm that provides satisfactory performance which is summarized in Fig. 3.8:

- Panel (a) shows a schematic representation of an image affected by residual dispersion with satellite speckles. We use d_x and d_y to refer to the horizontal and vertical offset between the PSF core and the radiation center respectively.

- Panel (b) shows a similar representation for which the PSF core has been masked out. The initial guess is that the PSF core corresponds to the radiation center (i.e. there is no residual dispersion). The original speckles (blue) are then radially stretched from the location of the original PSF core by a finite amount (in red, stretched speckles). One can observe that for a sufficiently large stretch factor (of the order of 20% in practice), the spectrally dispersed structures present in both images (the blue and the red) no longer overlap. This difference can be quantified by the L1 norm of the difference between the two images $\mathscr{L}$.

- The next step is to shift the assumed center of radiation, and re-stretch the original image to find the point at which the norm $\mathscr{L}$ is minimized (i.e. the speckles from the original image
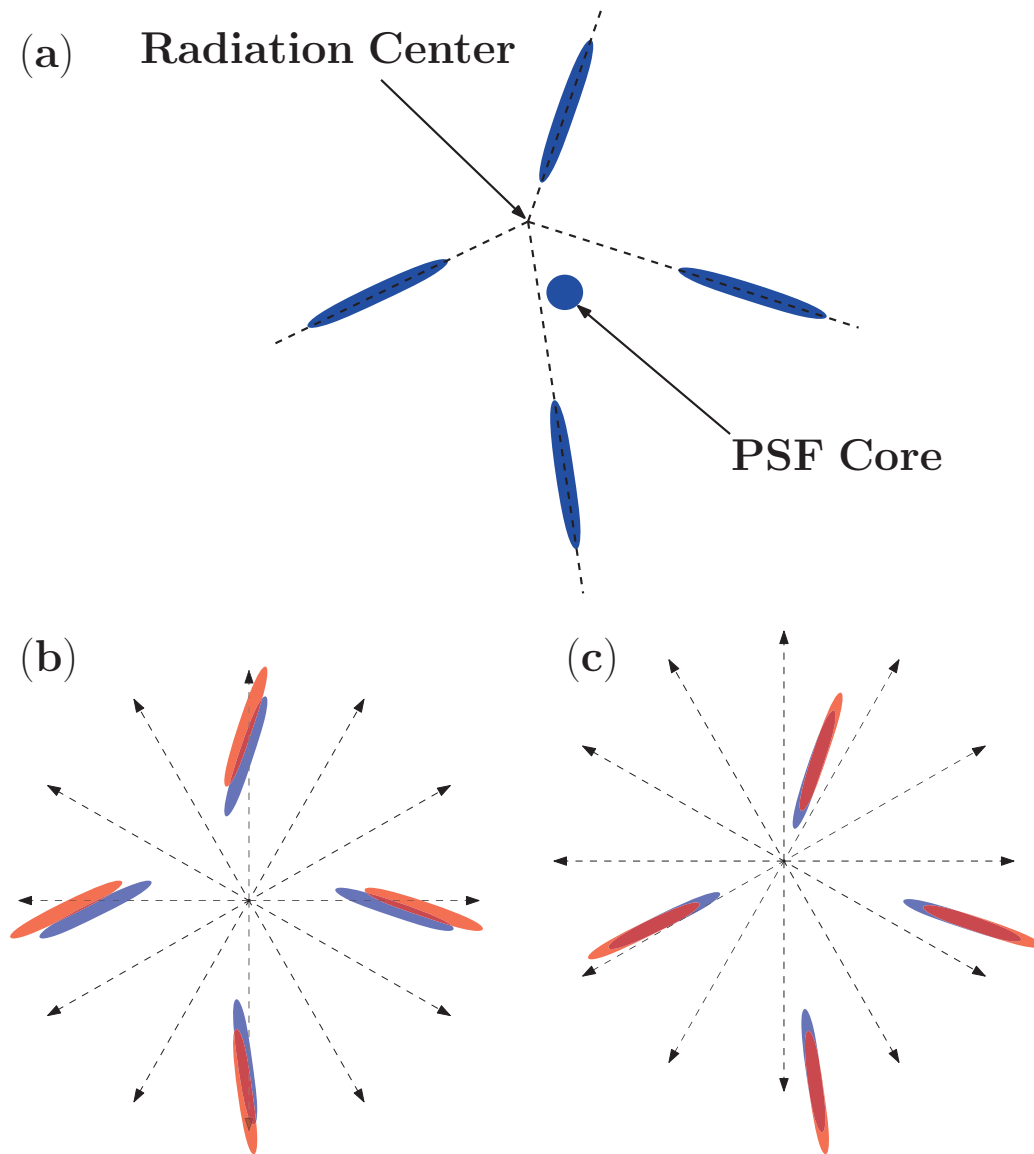
Figure 3.8: (a) PSF core and speckles with the presence of atmospheric dispersion. The elongated speckles meet at the radiation center. (b) Speckles only with PSF core removed. The blue speckles represent the original speckles, while the red ones are the same speckles, stretched radially from the PSF core. (c) Same schematic as in (b), except the stretch is done from the actual radiation center. In (c) stretched (red) and original speckles (blue) overlap significantly compared to (b).

and those from the stretched image overlap most). In this case, a raster scan is conducted but other scanning algorithms could also be used.

- Panel (c) shows a final case featuring both the original (blue) and the stretched (red) speckles, only this time, the latter was stretched from the correct radiation center: the speckles now have a significant overlap and our criterion of minimizing $\mathscr{L}$ is satisfied, which gives us a precise location of the radiation center.

The pseudo code and algorithm to find the location of the radiation center is given as,

$$For\ i\ \in -20,20$$
$$\qquad For\ j \in -20,20$$
$$\qquad\qquad x_0,y_0 = x_c + i,\ y_c + j$$
$$\qquad\qquad \mathscr{L}(x_0,y_0) = \sum_{x,y} |Im(x,y) - Im((x-x_0)\alpha + x_0, (y-y_0)\alpha + y_0)|.$$

Where x_0, y_0 are coordinate of the stretch, which are centered around the PSF core position (x_c, y_c) and α is the amount of stretch. For the practical purpose, the value of α used was 1.2 (20%). The reason for a stretch factor of $\approx 20\%$, which results in a better extraction of the radiation center compared to other stretch factors, is inherent in the algorithm used. For example, if a stretch factor is small 5%, original and stretched images (speckles) overlap and subtract throughout the raster scan, giving a low signal for the difference images, and for a high stretch factor 50%, original and stretched images overlap less again resulting in a poor signal.

The result of such a computation is shown in Fig. 3.9 for three cases, in the absence of residual dispersion shown by panel (a), with 10 mas of dispersion in the negative x-axis in panel (c) and with 40 mas of dispersion in the negative x-axis in panel (e). As expected in the first case, $\mathscr{L}$ is minimum when the PSF core and the radiation center are identical i.e. $d_x = 0$ and $d_y = 0$. In the second scenario, (d) the location of the minimum of the $\mathscr{L}$ is offset by $d_x = -2.0$ and $d_y = 0$. In the third case, (f) the location of the minimum of the $\mathscr{L}$ is offset by $d_x = -7.0$ and $d_y = 0$. The results of further simulations are summarized in the Table 3.1. The table shows the direction and amount of dispersion introduced in the PSF and the measured location of the radiation center in the image plane. The relationship between the residual dispersion and the location of the radiation center, $\mathscr{L}(d_x, d_y)$ can be written as,

$$|\vec{r}| = \frac{ps}{\alpha}\sqrt{d_x^2 + d_y^2}. \tag{3.19}$$

Where $\vec{r}$ is the vector representing the dispersion present in the PSF, ps is the plate scale of the camera, d_x and d_y are the offset positions of the radiation center in the camera plane given in pixels and α is the scaling factor.

The value of α was estimated based on the Eq. 3.19 and is summarized in Table 3.1. As can be seen from the table the value of α is twice for the amount of dispersion introduced and this relationship holds for small values of dispersion < 30 mas in y-H band. For larger dispersion speckles are no longer linear as shown in the Fig. 3.9 (e) and results in a poor measurement of the location of the radiation center.
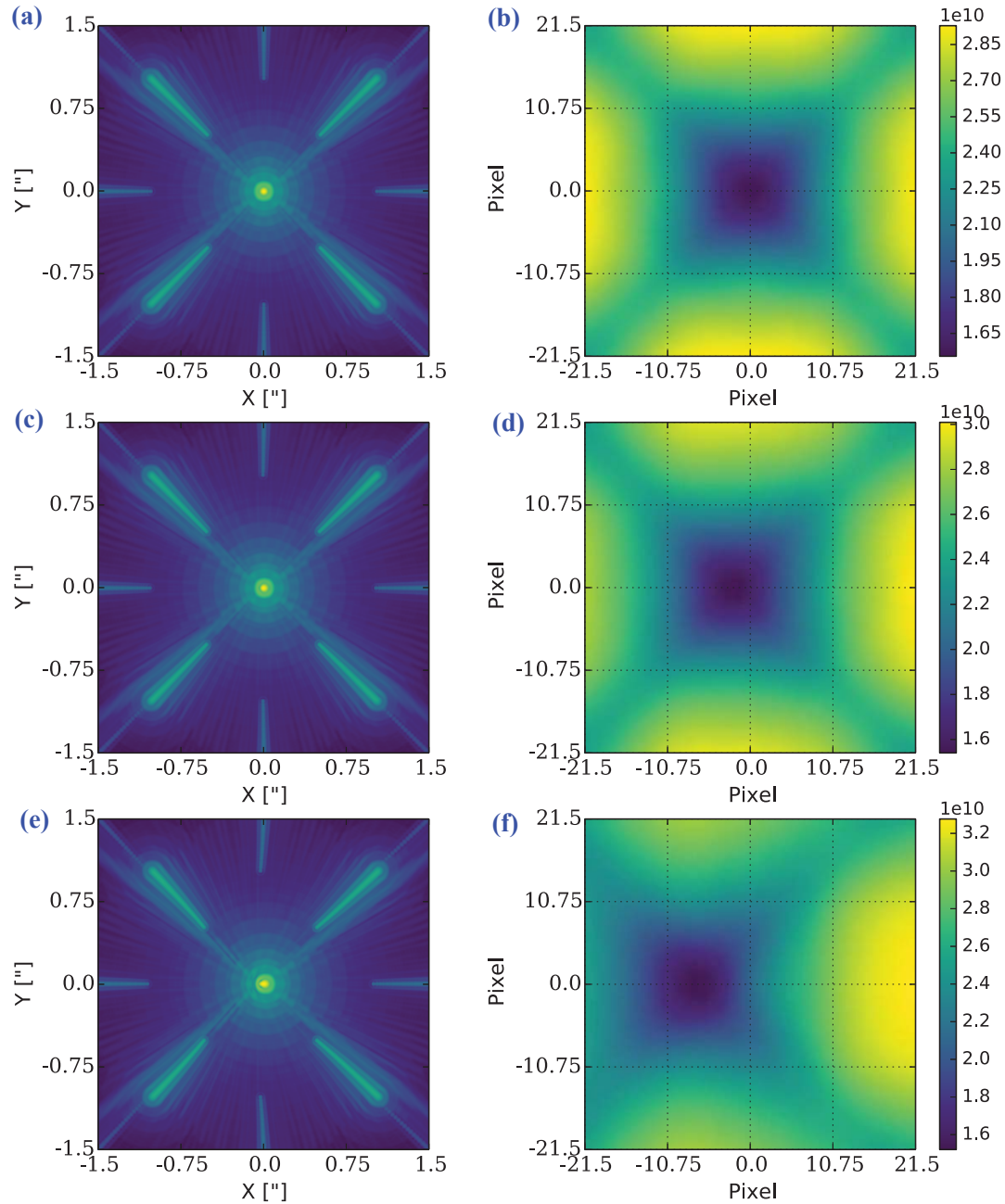
Figure 3.9: Left: simulated y-H band PSFs with satellite speckles, plate scale 10 mas/px. Right: offset of the radiation center represented by $\mathscr{L}$ (from position $(0,0)$ in image plane), with the color bar representing the relative intensity: (a) PSF with no atmospheric dispersion, (b) radiation center lies on the top of PSF core, (c) PSF with 10 mas atmospheric dispersion in y-H band, (d) radiation center lies 2 px left of the PSF core, (e) PSF with 40 mas atmospheric dispersion in y-H band, (f) radiation center lies 7 px left of the PSF core.

Table 3.1: Offset of the radiation center from the PSF core in a simulated y-H band PSF. The direction of dispersion is given with respect to the *y*-axis. (Plate scale is 10 mas/pix)

Introduced dispersion (mas)	Direction of the dispersion (°)	d_x(px)	d_y(px)	α
0	0.0	0.00	0.00	-
5	90.0	-1.01	0.00	2
5	00.0	0.00	1.00	2
10	90.0	2.00	0.00	2
20	00.0	0.00	4.00	2
60	90.0	-11.01	0.00	1.835

For small dispersions the empirical relationship between dispersion and offset of radiation center from the PSF can be written as,

$$r_i \simeq ps \times \frac{d_i}{2} \quad i \in [x, y].$$ (3.20)

The above relationship is used to calculate the on-sky dispersion in the PSF. By this method one can measure the residual dispersion down to sub-pixel accuracy (d_x and d_y).

3.4 Correcting dispersion

The previous section describes how to measure the dispersion in a PSF with high precision. In this section, I discuss various components of the dispersion present in an on-sky PSF and how they can be calibrated to close the loop on residual dispersion in the PSF.

Figure 3.10 shows a simulation of an H-band PSF affected by 60 mas of dispersion at $-45°$. The dispersion in the PSF can be represented as a vector $\vec{r}$, shown in the figure. The vector represents the amount and direction of the dispersion in the PSF. The next section discusses various sources of dispersion in an on-sky PSF.

3.4.1 Possible sources of dispersion

The presence of dispersion in an on-sky PSF can have various sources including the atmosphere, the ADC (if used) or an instrumental dispersion.

Each of the components can be represented as a vector, with a specific amplitude and direction, as shown in Fig. 3.11. The final dispersion in the PSF is then the vectorial sum of the various sources, i.e.

$$\vec{r}_{on-sky} = \vec{a}_{ADC} + \vec{s}_{atmosphere} + \vec{d}_{internal\_optics},$$ (3.21)

where, $\vec{s}_{atmosphere}$ is the dispersion from the atmosphere, $\vec{a}_{ADC}$ is the ADC dispersion vector to compensate for the on-sky dispersion, $\vec{d}_{internal\_optics}$ is the dispersion vector due to internal optics
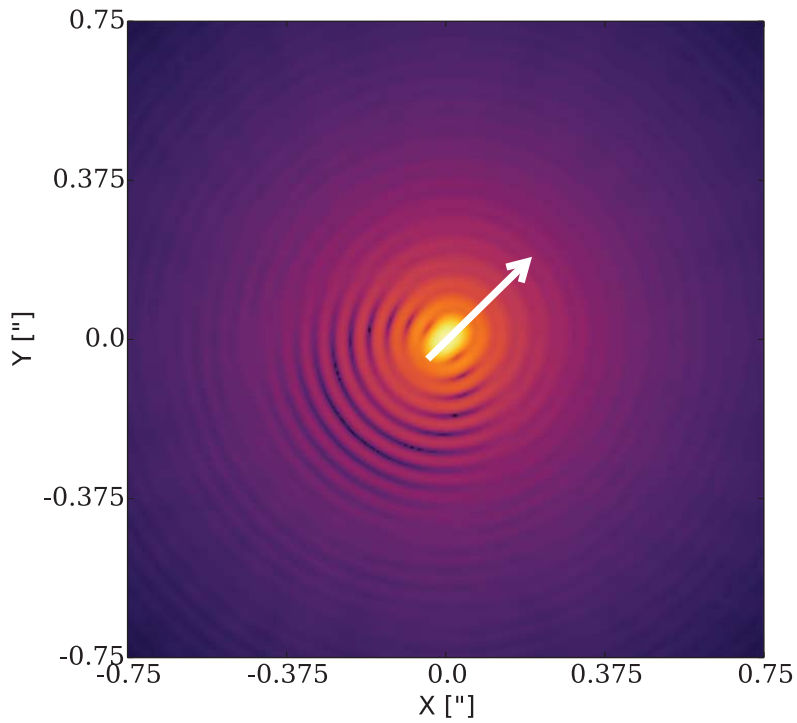
Figure 3.10: H-band PSF with 60 *mas* of dispersion in direction of 45° from *x*− axis. The dispersion can be represented as a vector whose length is given by the magnitude of the dispersion.
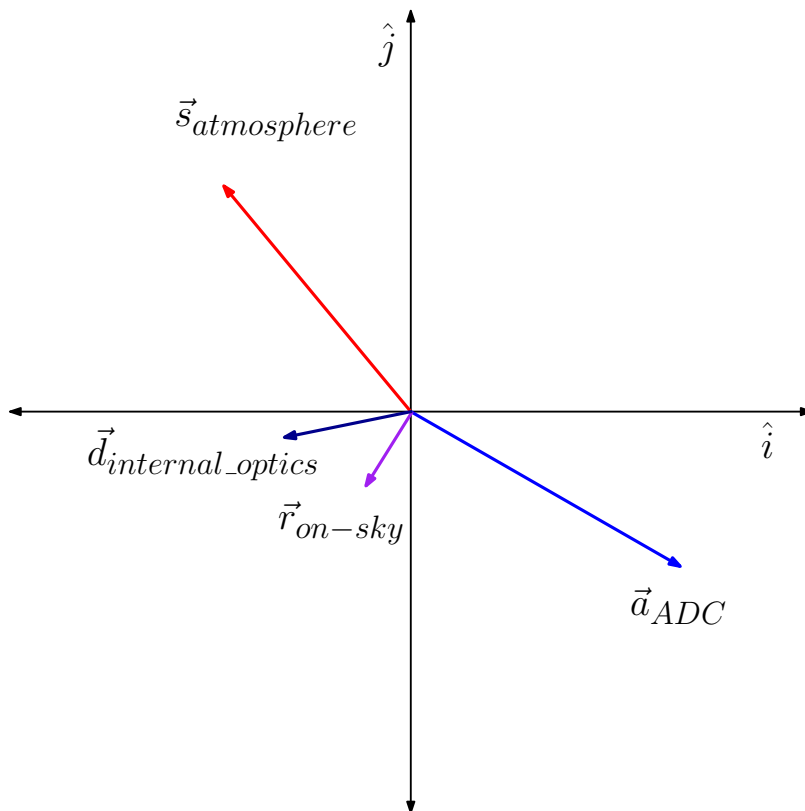
Figure 3.11: Various sources of dispersion, represented as a vector in the focal (camera) plane. The directions $\hat{i}$ and $\hat{j}$ are arbitrarily defined by the orientation of the camera. All possible dispersion vectors, present in an on-sky PSF are shown.

and $\vec{r}_{on-sky}$ is the total residual dispersion, which may not be zero due to imperfect compensation. The only non time-varying component in Eq. 3.21 is $\vec{d}_{internal\_optics}$, which is a constant. So we can conveniently define an on-sky dispersion vector, which is the sum of the atmospheric and internal optics, given by

$$\vec{d}_{on-sky} = \vec{s}_{atmosphere} + \vec{d}_{internal\_optics}. \tag{3.22}$$

Equation 3.21 can be rewritten as,

$$\vec{r}_{on-sky} = \vec{a}_{ADC} + \vec{d}_{on-sky}. \tag{3.23}$$

Since we know the orientation of the ADC, and we measure $\vec{r}_{on-sky}$ using the method described earlier, the only unknown parameter is $\vec{d}_{on-sky}$. The goal of the correction is to find the correct position for the ADC so $\vec{a}_{ADC}$ compensates the $\vec{d}_{on-sky}$, to have the smallest residual $\vec{r}_{on-sky}$. In the next section, I discuss the estimation of the on-sky dispersion vector and the calibration of the ADC dispersion vector by measuring the residual dispersion in the PSF.

3.4.2 On-sky calibration of dispersion

Figure 3.12 shows a vector based representation of the dispersions given by Eq. 3.23. The axes correspond to Cartesian coordinates in the image plane. The on-sky dispersion vector, i.e. the direction in which the PSF is elongated due to dispersion from the atmosphere and internal optics, is designated with the symbol $\vec{s}$ (from now $\vec{d}_{on-sky}$ is replaced by $\vec{s}$ for simplicity) in the figure. The dispersion vectors for the two prisms of the ADC are given by $\vec{p_1}$ and $\vec{p_2}$. They have equal dispersion magnitudes and add together to generate the total ADC vector $\vec{a}$, which is also dependent on orientation and is given by

$$\vec{a} = \vec{p_1} + \vec{p_2}. \tag{3.24}$$

If p is the dispersion magnitude of each prism, and θ_1 and θ_2 their orientation angles, then the two individual prism dispersion vectors are decomposed in the image coordinate system as

$$\begin{cases} \vec{p_1} &= p\cos(\theta_1)\hat{i} + p\sin(\theta_1)\hat{j} \\ \vec{p_2} &= p\cos(\theta_2)\hat{i} + p\sin(\theta_2)\hat{j} \end{cases}. \tag{3.25}$$

The ADC provides a maximum dispersion when the two prisms are aligned. When one prism is rotated 180 degrees relative to the other (anti-aligned), the ADC results in zero compensation.

In the case of an incomplete compensation, what is left is the residual atmospheric dispersion vector $\vec{r}$, as shown in Fig. 3.12, given by

$$\vec{r} = \vec{a} + \vec{s}. \tag{3.26}$$

The goal is to measure the residual dispersion and offset the ADC to minimize the dispersion, in a closed-loop operation. The steps involve calibration of the response of the ADC prisms (prism dispersion magnitude p) and calculation of on-sky dispersion. If we assume that the ADC prism
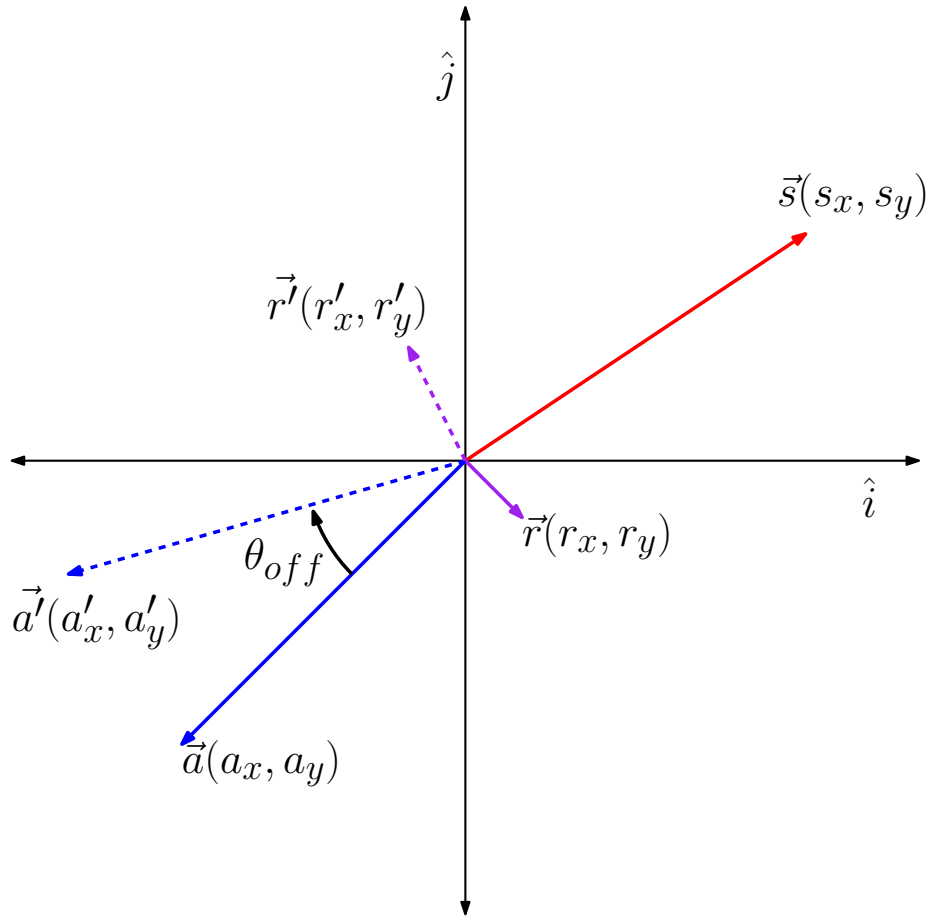
Figure 3.12: Principle of the ADC: the dispersion vector $\vec{s}$ is partially canceled by the ADC vector $\vec{a}$ and the residual vector is given by $\vec{r}$. ADC vector $\vec{a'}$ is generated when $\vec{a}$ is offset by an angle θ_{off}, resulting in a new residual vector $\vec{r'}$.

angles are known at all the time, then the components in the image coordinate system can be written as

$$
\begin{cases}
a_x & = p\cos(\theta_1) + p\cos(\theta_2) \\
a_y & = p\sin(\theta_1) + p\sin(\theta_2)
\end{cases} .
\tag{3.27}
$$

In the same coordinate system, the residual vector can be decomposed into

$$
\begin{cases}
r_x & = s_x + a_x \\
r_y & = s_y + a_y.
\end{cases} .
\tag{3.28}
$$

To calibrate the response of the ADC prisms, we assume that, over small timescales, the on-sky dispersion vector $\vec{s}$ is constant. As shown in Fig. 3.12, by making two measurements of residual $\vec{r}$ and $\vec{r'}$ using two known positions of ADC, we can eliminate the atmospheric contribution $\vec{s}$. By

rotating the ADC by an angle θ_{off}, the new ADC vector $\vec{a'}$ is given by

$$\begin{cases} a'_x & = p\cos(\theta_1 - \theta_{off}) + p\cos(\theta_2 - \theta_{off}) \\ a'_y & = p\sin(\theta_1 - \theta_{off}) + p\sin(\theta_2 - \theta_{off}) \end{cases}. \tag{3.29}$$

The new residual vector $\vec{r'}$ is then decomposed into

$$\begin{cases} r'_x & = s_x + a'_x \\ r'_y & = s_y + a'_y \end{cases}. \tag{3.30}$$

By subtracting Eq. 3.30 from Eq. 3.28, we get

$$\begin{cases} r_x - r'_x & = a_x - a'_x \\ r_y - r'_y & = a_y - a'_y \end{cases}. \tag{3.31}$$

Substituting the Eqs. 3.27 and 3.29 into Eq. 3.31, we get

$$\begin{cases} p \times l & = r_x - r'_x \\ p \times m & = r_y - r'_y \end{cases}, \tag{3.32}$$

where l and m are given by

$$\begin{cases} l & = \cos(\theta_1) + \cos(\theta_2) - \cos(\theta_1 - \theta_{off}) - \cos(\theta_2 - \theta_{off}) \\ m & = \sin(\theta_1) + \sin(\theta_2) - \sin(\theta_1 - \theta_{off}) - \sin(\theta_2 - \theta_{off}) \end{cases}. \tag{3.33}$$

By solving Eq. 3.32, we get

$$p = \left(\frac{(r_x - r'_x)^2 + (r_y - r'_y)^2}{l^2 + m^2} \right)^{\frac{1}{2}}. \tag{3.34}$$

Since we know the prism angles θ_1 and θ_2, and the offset applied to the prisms θ_{off}, the value of l and m can be deduced using Eq. 3.33. Then by substituting the values of the measured residual dispersion (r_x, r_y), (r'_x, r'_y), and l and m into Eq. 3.34, the magnitude of the prism dispersion vector p can be calculated.

Once p is determined from the measurements, the vector $\vec{a}$ is known for any ADC angle using Eq. 3.27. For any measurement of the residual vector $\vec{r}$, we can deduce the on-sky dispersion vector $\vec{s}$ using Eq. 3.26. Finally, once we know the on-sky dispersion $\vec{s}$, we can determine the new ADC position by using the Eq. 3.35. To completely minimize the residual dispersion in the PSF, the new ADC dispersion vector should be equal and opposite to the on-sky vector. As given by the Eq. 3.35, θ'_1 and θ'_2 are the new prisms angles to compensate the on-sky dispersion vector, such as

$$\vec{a}_c = -\vec{s} \tag{3.35a}$$
$$\vec{a}_c = -(\vec{s}_x + \vec{s}_y) \tag{3.35b}$$
$$\vec{a}_c = p \left[\cos(\theta'_1) + \sin(\theta'_1) + \cos(\theta'_2) + \sin(\theta'_2) \right]. \tag{3.35c}$$

In the next section, I am presenting ADC simulations that I used to verify the concepts presented here.
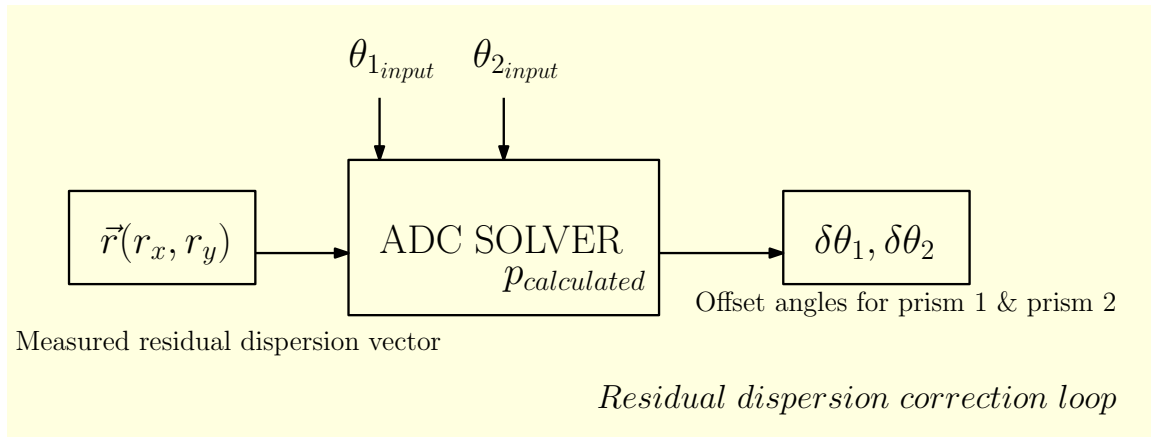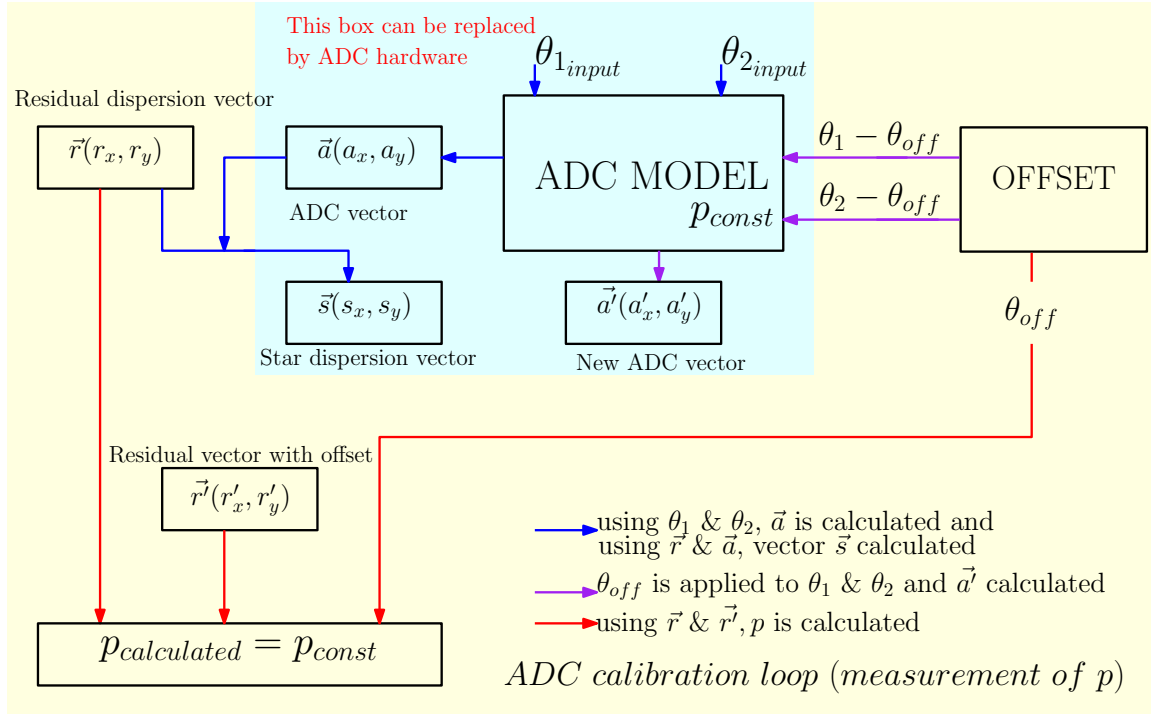
Figure 3.13: Schematic of the control loop, used for calibration of the ADC and calculating the offset angles of the prisms, and for correcting the on-sky dispersion.

3.5 ADC simulation

I simulated the operation of an ADC to test the extraction of the on-sky dispersion by measuring the total dispersion in a simulated PSF. Using the simulations presented in Sec. 3.3.1, I introduced a constant on-sky dispersion in the PSF and a varying ADC dispersion vector. The magnitude and direction of the ADC vector can be varied by changing the direction of prisms, θ_1 and θ_2, as given by the Eq. 3.25. The simulation presented here follows the steps explained in the previous section.

The top chart in the Fig. 3.13 shows the steps involved with the calibration of the ADC, as explained below in details.

1. First step: the ADC model takes the prism angles θ_1 and θ_2 as an input, as well as the magnitude of the prism dispersion vector p, which is an unknown constant. Using these input parameters, the dispersion vector due to the ADC was calculated, which was then output as $\vec{a}(a_x, a_y)$. The measured residual dispersion vector $\vec{r}(r_x, r_y)$ from the PSF is sum of the ADC and on-sky dispersion vectors.

2. Second step: the ADC model is rotated by an angle θ_{off} to both the prism angles θ_1 and θ_2, which gives us a new ADC dispersion vector $\vec{a}'(a'_x, a'_y)$. The change in ADC vector changes the residual dispersion in the PSF to $\vec{r}'(r'_x, r'_y)$. Now using the Eq. 3.34 and inputing values for the residual vectors $\vec{r}$, $\vec{r}'$, θ_1, θ_2 and the offset angle θ_{off}, the prism dispersion magnitude p can be calculated, giving $p_{calculated}$.

In the second part of the simulation, as shown by the bottom flow chart in Fig. 3.13. The value $p_{calculated}$ was then used to calculate the ADC vector $\vec{a}$ in any orientation, using Eq. 3.27. By using the measured vectors $\vec{r}$ and $\vec{a}$, the on-sky dispersion vector $\vec{s}$ can be calculated. Now the ADC solver was used to calculate offset angles $\delta\theta_1$ and $\delta\theta_2$, that will give a better correction of dispersion by offsetting the prisms by these angles.

3.6 Summary

In this chapter, I discuss in detail simulation of a PSF from telescope pupil geometry, adding WFE to the PSF, generating focal plane satellite speckles. The concept for the measurement of dispersion using calibration speckles and simulations (PSF with the atmospheric dispersion and broadband focal plane speckles) were carried to verify the concept. An algorithm which consists of a raster scan was developed to measure the dispersion using calibration speckles. Also, the framework for correcting the residual dispersion with the aid of an ADC was developed. The framework was developed in a way, that ADC prisms could accept offsets to correct for residual dispersion in addition to look-up table based correction.

In conclusion, with the aid of simulations and algorithms, I established a framework using focal plane based calibration speckles for the measurement and correction of atmospheric dispersion. In the next chapter, I discuss the instruments SCExAO and AO188, which are used for the measurement and correction of atmospheric dispersion on-sky.

Experimental Setup

The measurement and correction of atmospheric dispersion utilizes modules of SCExAO and the Subaru Telescope facility adaptive optics system, AO188. The measurement of dispersion utilizes focal plane calibration speckles generated using the DM and internal NIR camera in SCExAO and the correction of dispersion is carried out by driving the science path ADC inside of AO188. This chapter briefly describes SCExAO, AO188 and the science path ADC of AO188.

4.1   SCExAO

The SCExAO instrument (Jovanovic et al., 2015b), currently undergoing commissioning at the Subaru Telescope is a multipurpose high-contrast instrument designed for the discovery and detailed characterization of exoplanets. The instrument is equipped with an ultra-fast visible PyWFS operating at 2 kHz, which drives a 2000-actuator DM and LLOWFS to stabilize the PSF on the coronagraph. SCExAO offers other wavefront control capabilities such as speckle control, as well as numerous other imaging and spectroscopic instrument modules, which include the integral field spectrograph CHARIS (Brandt et al., 2014), VAMPIRES (Norris et al., 2015) and FIRST (Huby et al., 2012). SCExAO is optimized for very small IWA observations down to 1 λ/D, unlike other high-contrast instruments like the GPI (Macintosh et al., 2014b), SPHERE (Beuzit et al., 2008b; Bonnefoy et al., 2016) and P1640 (Dekany et al., 2013). The ultimate science goal of SCExAO is the direct imaging of extrasolar planets around stars at a separation corresponding to the diffraction limit of the telescope in the NIR, y-K-bands ($0.95 - 2.4\mu$m).

As shown in Fig. 4.1, SCExAO is located after AO188 where it benefits from the first stage of wavefront correction by that system. AO188 provides a PSF with a Strehl ratio of about $20-40\%$ in the H-band in median seeing, which SCExAO further improves upon pushing the Strehl ratio to $80-90\%$.

The HCI capability of SCExAO is achieved in four ways:

- Visible PyWFS, (700-900 nm): it corrects the WFE at speeds up to 3.5 kHz, using a 2000-actuator DM, for spatial frequencies up to 22.5 λ/D (Esposito and Riccardi, 2001; Guyon, 2005).

- Small IWA and high-throughput coronagraphs: A large choice of highly efficient coronagraphs such as PIAA, the vortex, 8-octant phase mask, coronagraphs are used to cancel most of the starlight reaching the science detector, see section 4.1.4.

- A Lyot-based Low-Order Wavefront Sensor (LLOWFS): for ultra-fine pointing control of the coronagraphic PSF in the NIR, low-order aberrations upstream of the phase mask can be
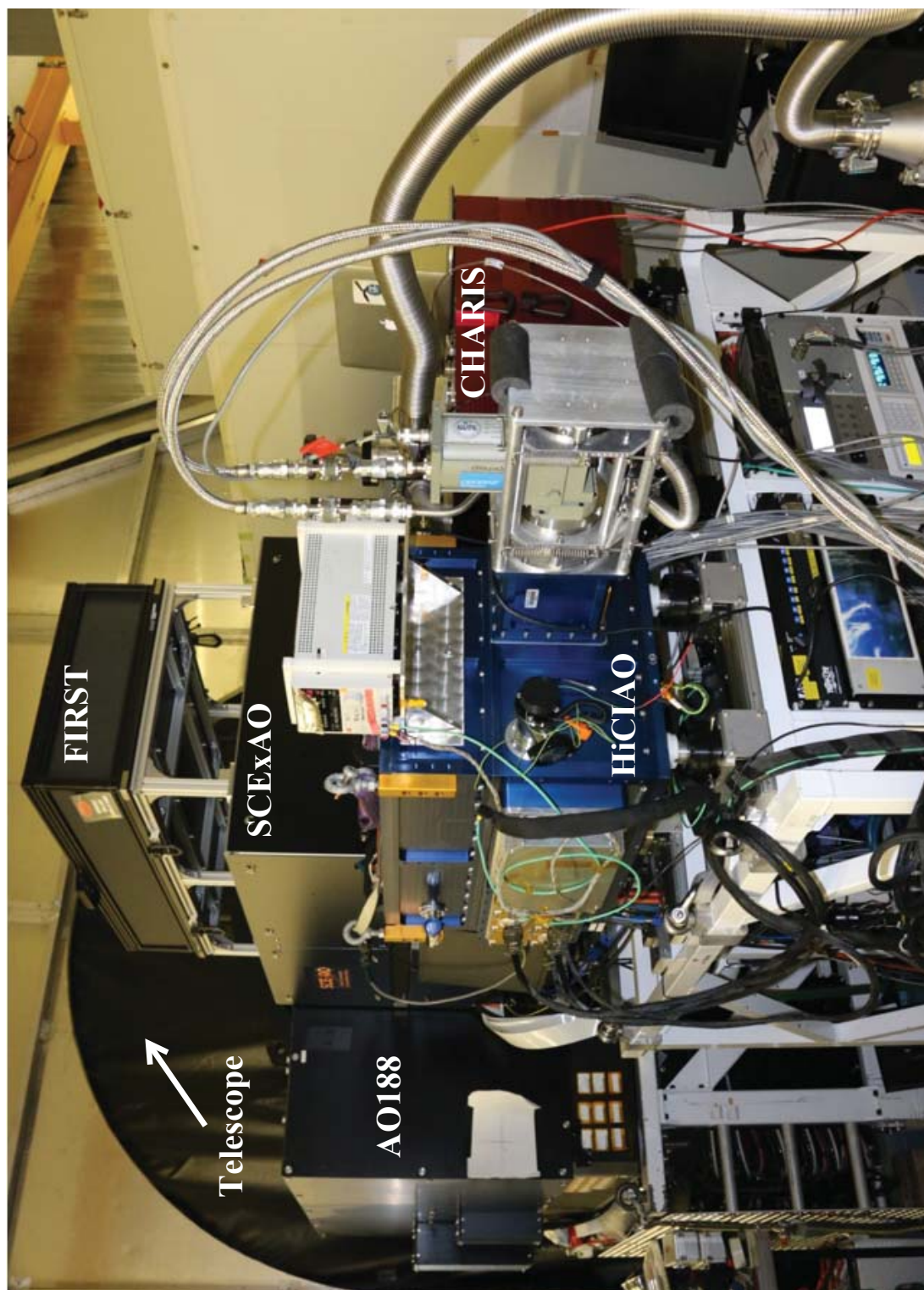
Figure 4.1: SCExAO at the Nasmyth platform of the Subaru Telescope. It sits behind the facility AO instrument AO188 which injects the light into SCExAO. Science imagers CHARIS and HiCIAO are shown on the right. The FIRST recombination bench sits at the top of the SCExAO bench. Image courtesy of Nemanja Jovanovic.
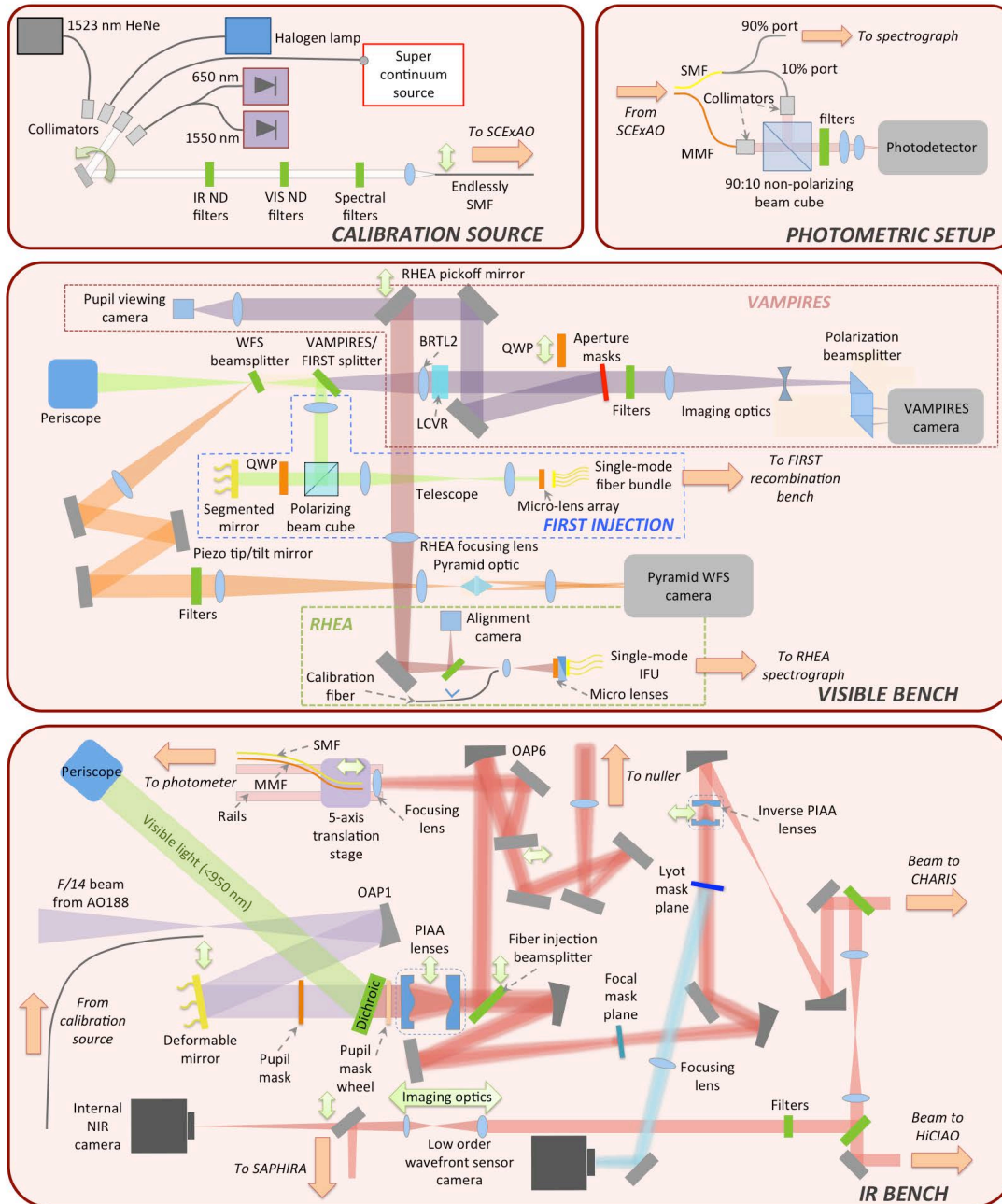
Figure 4.2: Optical layout of the SCExAO instrument. Dual green arrows indicate that an optical component can be removed or translated along the beam. IR bench, which takes input light from AO188 and sends the visible light to the visible bench (middle box). The visible bench sits on top of the IR bench and FIRST recombination bench sits on the top of the visible bench as shown in Fig.4.1. Image courtesy of Nemanja Jovanovic.

measured using the rejected starlight and to drive a control loop that fine tunes the tip/tilt as well as a few dozen Zernike modes at the coronagraphic focal plane (Singh et al., 2015b).

- Fast NIR speckle control: Using a fast NIR camera and speckle probing techniques that use commands sent to a DM to probe the speckle halo, it is possible to calibrate and remove residual speckles on one half of the image plane, down to 2 λ/D. The control is implemented by sending offsets to the PyWFS control loop (Martinache et al., 2014b).

4.1.1 SCExAO's modules

As shown in Fig. 4.1 and 4.2, the SCExAO instrument consists of two main benches. The bottom bench analyzes the IR part of the spectrum, between y- and K-band, while the top bench analyzes the optical part of the spectrum, between 600 and 950 nm. The bottom bench hosts the DM, coronagraphs, and a low order WFS known as the LLOWFS while the top bench hosts the PyWFS, VAMPIRES and FIRST. Each module is discussed briefly below, for a full description readers are encouraged to see papers on each of the modules.

The light coming from AO188 is first collimated and the pupil re-imaged on the 2k-actuator DM. A dichroic then separates the visible and IR light (cutoff at 940 nm). The visible light is then sent to the top bench using a periscope. After passing through the dichroic, the NIR light can either go through various coronagraphs —consisting of optional PIAA lenses apodizing the beam, focal plane masks, and Lyot stops— or be injected into a single mode fiber for high-resolution spectroscopy (Jovanovic et al., 2014, 2016).

After propagating through the bench, there are a number of science detectors employed by SCExAO, which utilize the NIR light:

1. The internal NIR detector: a fast (170-Hz) detector used mainly for lab testing (alignment and characterization of the bench) and on-sky focal plane wavefront control (speckle nulling and measurement of dispersion).

2. Coronagraphic High Angular Resolution Imaging Spectrograph (CHARIS): an integral field spectrograph developed by Princeton University, which has been commissioned. It will provide high-resolution spectra in J, H or K bands, or a low-resolution spectrum spanning from J- to K-band in a single shot (McElwain et al., 2012).

3. High Contrast Instrument for the Subaru Next Generation Adaptive Optics (HiCIAO): used for longer exposures of a given target (Hodapp et al., 2008).

4. SAPHIRA: currently undergoing on-sky testing. It is a fast (> 1-kHz) photon-counting detector in the NIR (H-band), developed by the Institute for Astronomy (IfA) in Hilo, Hawaii (Atkinson et al., 2014). It will be used for focal plane wavefront control when fully commissioned.

5. MKID Exoplanet Camera (MEC): a photon-counting energy-discriminating camera developed by University of California Santa Barbara (Mazin et al., 2012). Microwave Kinetic Inductance Detector (MKID) arrays are one of the most advanced detector types, with the capability to wavelength-resolve the light while photon counting at kHz speeds with no read-out noise. Most importantly, the fast and continuous readout of MKIDs allows for focal plane speckle control at kHz speed. The spectral resolution provides additional information to enable speckle control in broadband, removing the current dominant noise-source in direct imaging instruments, see Chapter 1.

SCExAO's top bench (visible light) is used by the following modules:

1. The PyWFS (800 − 900 nm): it is used for the high order wavefront correction using a pair of roof prisms to simulate the pyramidal optic as well as a high-frame rate (up to 3.5 kHz) EMCCD detector (FirstLight Imaging, OCAM2k).

2. The Visible Aperture Masking Polarimetric Interferometer for Resolving Exoplanetary Signatures (VAMPIRES, 600 − 800 nm): It is an interferometric imager utilizing the aperture masking technique to enable diffraction-limited imaging in the visible combined with polarimetric capabilities. VAMPIRES can detect faint structures at a few *mas* from the star, like dust shells and protoplanetary disks.

3. The Fibered Imager for a Single Telescope (FIRST, 600 − 800 nm): it is a visible light instrument that is based on a novel principle combining the techniques of aperture masking and spatial filtering of the wavefront using single mode fibers. FIRST can detect very close companions like brown dwarfs and giant planets at a few *mas* of the main star once fully commissioned.

4.1.2 The deformable mirror

The 2000-actuator DM used in SCExAO as shown in the Fig. 4.3 (a) is based on MEMS technology manufactured by Boston Micromachines Corporation. The DM sits inside a sealed chamber in order to control the humidity level around the DM. The window of the DM is optimized for transmission across 550 − 2500 nm, which is the operating range of the SCExAO instrument. The 18 mm-diameter pupil of SCExAO is sampled by 45 actuators across. The number of actuators across the pupil is important as it defines the control region of the wavefront control system in the focal plane (highest spatial frequency controlled by the DM). The 45 actuators across the pupil diameter means spatial frequencies up to 22.5 λ/D from the PSF can be addressed. This is achieved by controlling spatial frequencies which go up to the Nyquist frequency of the DM (i.e. every actuator pistoned π out of phase), which corresponds to 22.5 cycles across the aperture. In the focal plane 22.5 λ/D translates to a control region of 0.9″ in H-band. The total number of actuators illuminated inside the Subaru Telescope pupil is ∼ 1200 (excluding actuators behind the spiders and central obstruction).

SCExAO's DM control software consists of 12 channels, which allows a combined offsets from the channels to the DM independently. This enables lab testing and on-sky implementation of various wavefront control techniques, including LLOWFS, speckles nulling, the calibration grid and the measurement of dispersion.

The lab testing using the DM involves injecting phase errors to simulate a dynamical turbulence using Kolmogorov phase screens. These phase screens can also be filtered to mimic the effects of the low and high spatial frequencies for various lab tests. The simulated turbulence can run in one of the channels of the DM and corrections can be injected independently using another channel. The final applied voltage map to the DM is the sum of the injected phases (in μm) in the 12 channels of the DM. As an example Fig. 4.3 (b) (bottom) shows diffraction of the PSF using a sine-wave, which acts as a grating in the pupil plane (Fig. 4.3 (b) top) diffracting the PSF in the focal plane. The first and second order diffraction features can be clearly seen from the figure.
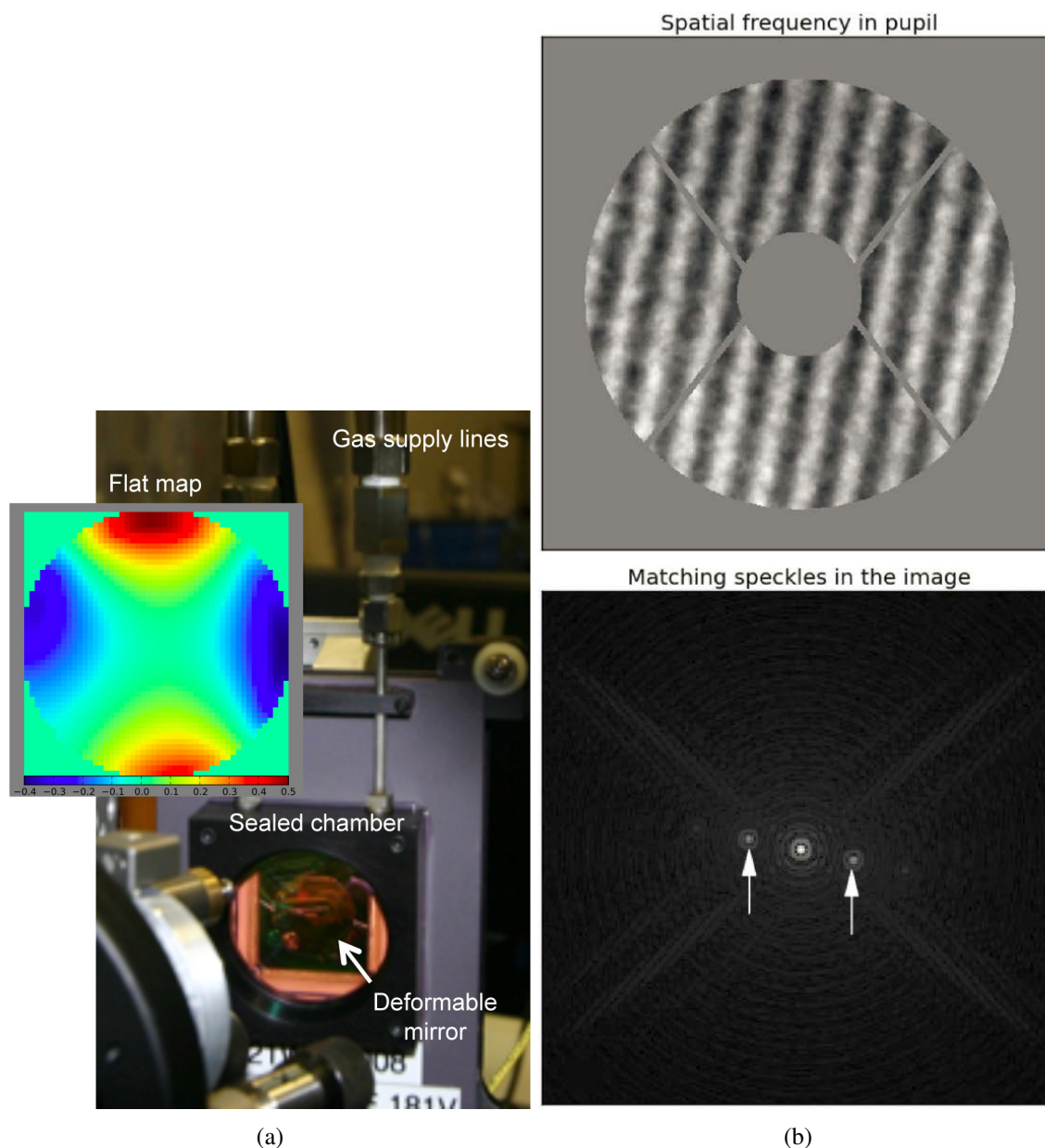
Figure 4.3: (a) The 2k actuator DM of the SCExAO instrument with 50 actuators in diameter. The inset shows the DM flat map in micron required to flatten the DM. (b) Top: a single spatial frequency (a sine-wave) applied to the DM to create a grating. Bottom: corresponding PSF, 1st and 2nd orders of diffraction features can be seen. Image courtesy (Martinache et al., 2014a).

4.1.3   Internal camera

SCExAO's internal NIR science camera is an Axiom Optics's (model number, OWL SW1.7HS) camera based on an InGaAs CMOS detector with wavelength coverage from $0.9 - 1.7 \mu$m. The pixel size is 30 μm. The camera is mounted on a translation stage allowing it to be conjugated to the focal or pupil planes. This sensor has a size of 320×256 pixels and runs at a high frame rate of 170 Hz.

The camera has the following quantum efficiency in various bands: 58% (y-band), 73% (J-band) and 73% (H-band). The plate scale of the camera is 16.7 mas/px.

For the measurement of the dispersion, the internal NIR camera was used. It was used as this is the only working camera in the NIR (SAPHIRA is being tested for on-sky deployment), which had a high enough frame rate for the measurement and correction of the dispersion. Due to the high readout noise of NIR camera ($114\ e^-$), the measurement of dispersion was limited to bright targets in this work.

4.1.4 Coronagraphs

The SCExAO's capability to image exoplanets at the diffraction limit of the telescope is achieved by employing low IWA coronagraphs, as explained in Chapter 1. These coronagraphs include: PIAA (Guyon et al., 2010), which exhibits an IWA close to $1\lambda/D$, the Vortex (Mawet et al., 2010), Four-Quadrant Phase Mask (FQPM) (Rouan et al., 2000) and 8-Octant Phase Mask versions (8OCM) (Murakami et al., 2010). The PIAA coronagraph employed in SCExAO was designed to provide a raw-contrast of 10^{-6} at $1.5\lambda/D$. In this thesis work, the vortex coronagraph has been used extensively. Chapter 6 presents theory, lab characterization and simulations for the vortex coronagraph employed by the SCExAO. Table 4.1 summarizes various coronagraphs employed by SCExAO with their IWA and waveband of operation.

Table 4.1: Summary of SCExAO coronagraphs.

Coronagraph type	PIAA	Vortex	8OPM	Shaped pupil
Inner working angle (λ/D)	1.5	1	1	3
Waveband(s)	y-K	H	H	y-K

4.1.5 Preliminary science results

SCExAO is currently undergoing commissioning and so are some of its modules. At present, the extreme AO loop is not yet fully commissioned but still it has started to provide a consistent PSF with Strehl-ratio of $70-90\%$ (H-band). Currently one of the major limiting factors faced by SCExAO is telescope vibrations, which are being resolved (Lozi et al., 2016). Despite this, SCExAO has started producing science results which are summarized below.

Figure 4.4 shows a recent science image of Neptune taken by CHARIS during one of its commissioning nights. As CHARIS is an integral field spectrograph (IFS) it can take a low-resolution image from J-K band, which is shown in Fig. 4.4. Figure 4.5 shows some science images taken using SCExAO/HiCIAO during its engineering/science runs. Figure 4.5 (a) presents an image of the HR8799 system with its four planets b, c, d, and e clearly visible. Panel (b) shows the giant planet/brown dwarf Andromedae b, as a clear detection with a Signal-to-Noise Ratio (SNR) of 100. Panel (c) shows a debris disk around HD 36546, recently discovered by SCExAO (Currie et al., 2017). Panel (d) shows a 5σ contrast curve comparing the performance of SCExAO/HiCIAO to GPI and AO188/HiCIAO. The images taken by HiCIAO/SCExAO are about 3 times better in IWA and SNR than with HiCIAO/AO188 alone.
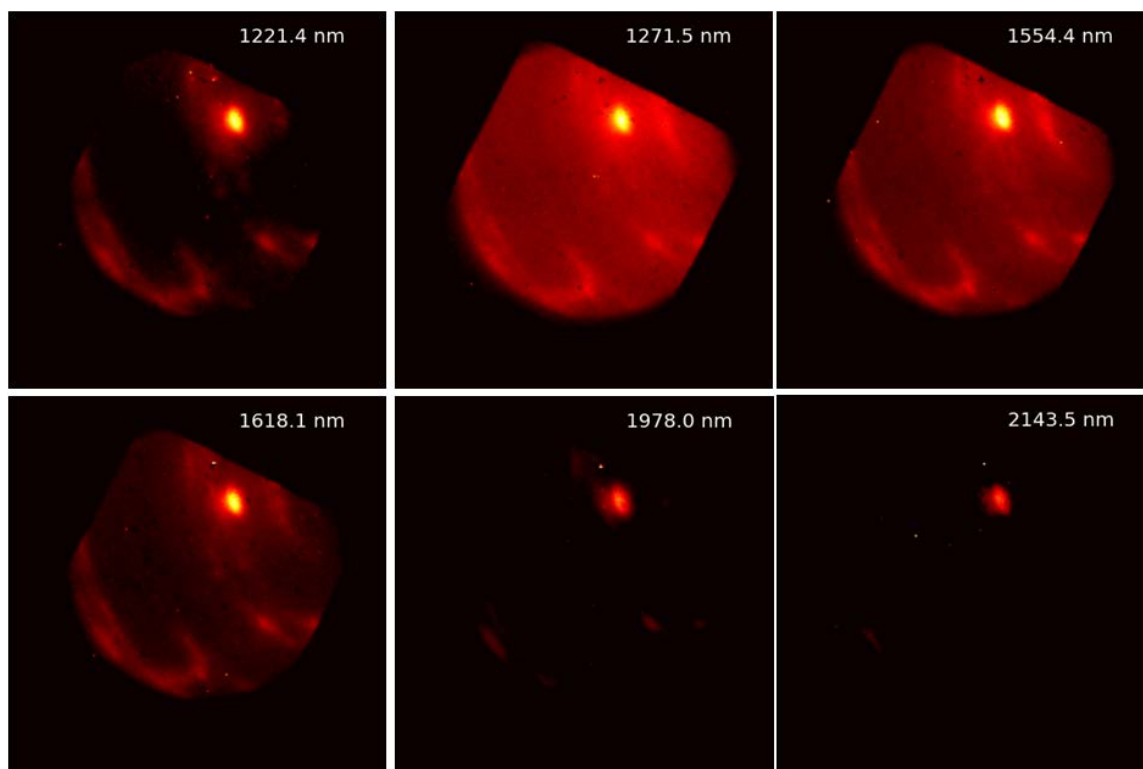
Figure 4.4: A recent result from SCExAO taken using CHARIS: image of Neptune in waveband J-K, during one of the commissioning night. Image courtesy Timothy Brandt

4.2 Subaru Telescope facility adaptive optics system, AO188

AO188 has a curvature based WFS and is a second-generation AO system of the Subaru Telescope (Takami et al., 2004; Minowa et al., 2010). It uses a 188 element DM, which was an upgrade from the precursor instrument that used 36 elements (Takami et al., 1998). It can operate with a natural guide star (NGS) or with a laser guide star (LGS) (Hayano et al., 2008; Saito et al., 2010). AO188 saw its first light in late 2006 with IRCS and it was offered for open use since October 2008. AO188 is a classical single conjugate AO system, in which the DM is optically conjugated to the ground layer of the turbulence. The specifications of AO188 in NGS and LGS modes are summarized in Table 4.2. SCExAO does not require a large field of view (FOV), $< 10''$ maximum, and is used in NGS mode only.

Figure 4.6 shows the optomechanical design of AO188, it shows various parts of AO188 like the DM, ADC, K-mirror (AOIMR), high and low order wavefront sensors (HOWFS and LOWFS). The figure shows the path of the light beam from the telescope through AO188 to the science instruments. AO188 has a science path ADC before the DM to compensate for the atmospheric dispersion in both the visible and IR ($0.45 - 2.2\ \mu$m) for the science instruments and WFS. The beam is split by a dichroic, which reflects the optical light between $0.4 - 0.64\ \mu$m for wavefront sensing and transmits the optical and NIR light $> 0.64\ \mu$m to SCExAO.

The AO188 DM is a Bimorph mirror with 188 elements, which is made of two PZT (piezoelectric material) plates with a diameter of 130 mm (beam size 90 mm) and a total thickness of about 1.9
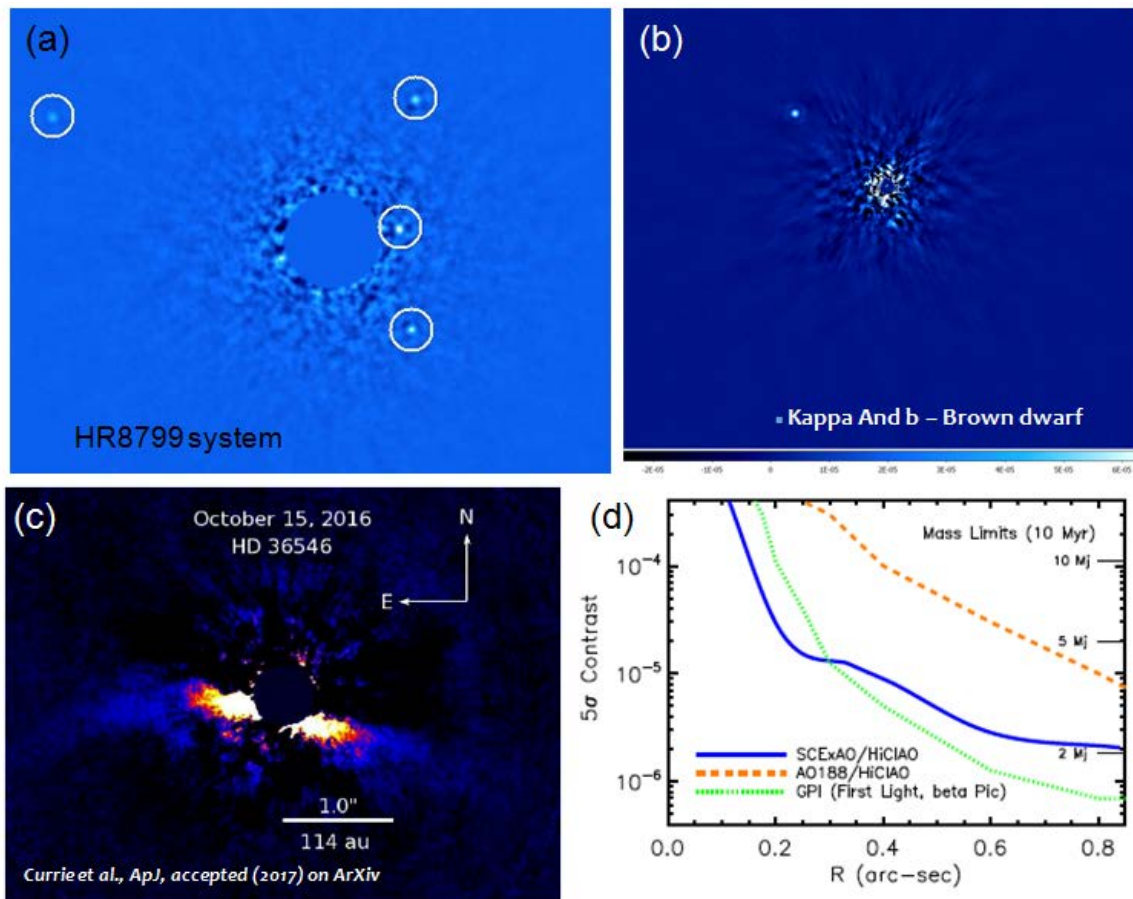
Figure 4.5: Recent results from SCExAO taken using HiCIAO: (a) the HR8799 system with all the four planets b,c,d, and e clearly visible. (b) The Kappa And b brown dwarf. (c) The debris disk around HD 36546. (d) A contrast curve of SCExAO/HiCIAO compared to GPI and AO188/HiCIAO. Image courtesy (Currie et al., 2017).

mm. The control electrodes are located between the two plates. A curvature WFS with 188 elements is used for the wavefront sensing. Optical fibers are employed to feed light from the focus of each sub-aperture to 188 photon-counting APDs. RTC is used to analyze the wavefront measurements from the WFS to reconstruct a response matrix, the control vector is then sent to the DM, running at a speed of 1 kHz to correct for the WFE.

The performance of AO188 is summarized in Table 4.3. It shows the Strehl ratio in NGS and LGS modes under various observing conditions. The Strehl ratio measurement was done for K-band, which is centered at 2.2 μm. AO188 typically provides 60% Strehl for mR < 10 in K-band under good seeing conditions ($0.4 - 0.6''$). In H-band under moderate seeing, the Strehl ratio is in between $20 - 40\%$ and the total wavefront residual is < 200 nm RMS. Which is a typical WFE observed by SCExAO during on-sky observations.
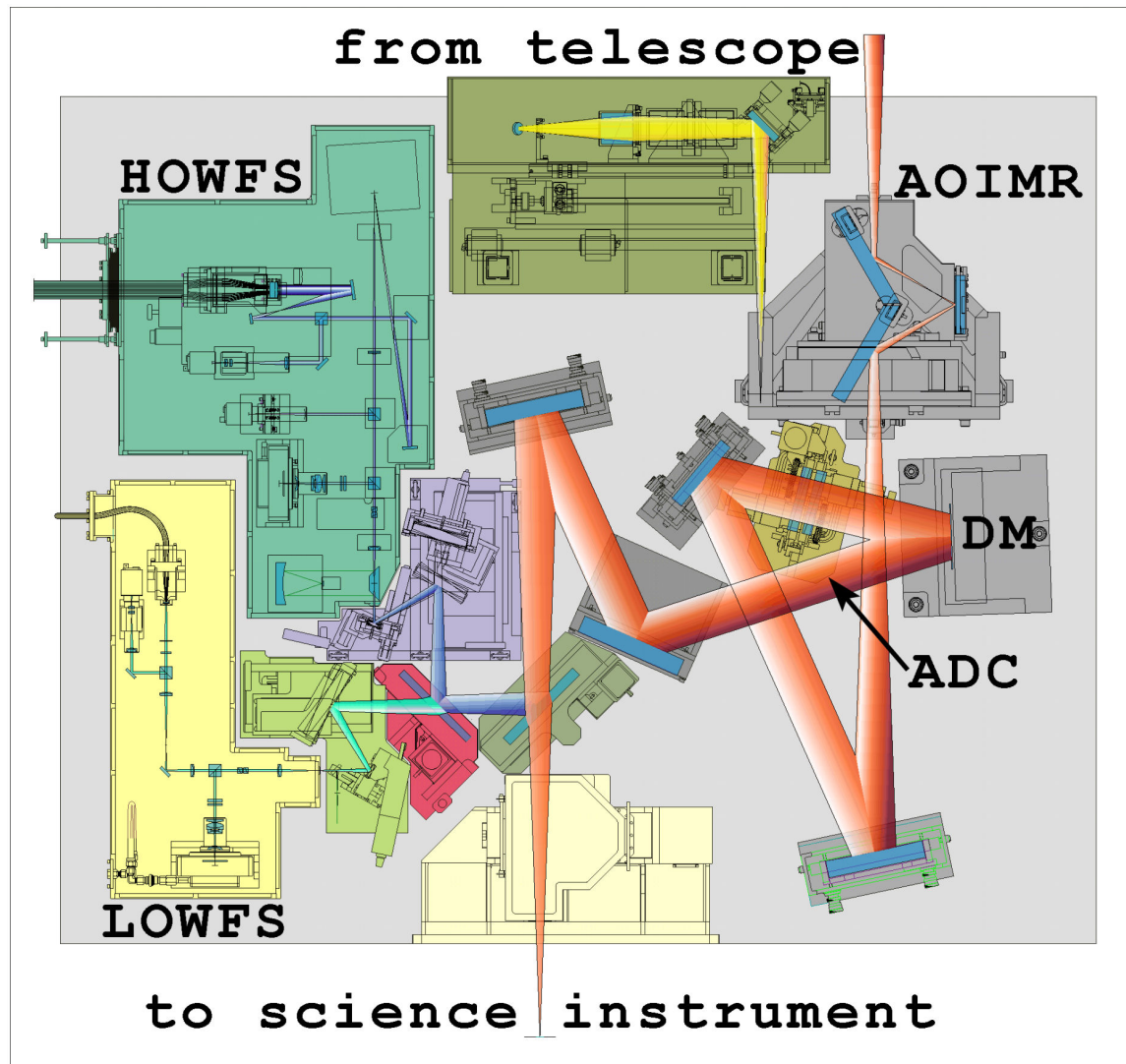
Figure 4.6: Optomechanical design of AO188. Various elements of AO188 are shown and the path of the light beam coming from the telescope to the science instrument is highlighted. Image courtesy Egner et al. (2010)

Table 4.2: Summary of AO188 NGS/LGS mode specifications. Courtesy of Subaru Telescope

Location of the system	Nasmyth focus (IR)
Spectral coverage	$0.9 - 5.3 \, \mu$m (JHKLM)
Field of view	$2'.7$ (arcsec)
Main optics throughput	70%
Guide star magnitude	$-1 < R < 16.5$ (NGS)
Tip/tilt mount stroke	± 5
High-order WFS	Curvature sensor with 188 photon counting APDs
Low-order WFS	2×2 Shack-Hartman sensor with 16 photon counting APDs
Control bandwidth	> 100 Hz, 1000 corrections/sec
TTGS magnitude	$R < 18$
NGS isoplanatic field	$1'$ in diameter
Deformable mirror	Bimorph mirror with 188 elements
TTGS isoplanatic field	Not determined
Laser	Sum frequency generation 4.0W (on-sky) at 589nm (generates R= 11 LGS)
Laser beam transfer optics	Single mode photonic crystal fiber
Laser launching telescope	50cm telescope attached behind the secondary
Real time computer	4 Xeon CPUs (2.0GHz) with real time Linux OS
Science instrument	IRCS, HiCIAO, SCExAO

Table 4.3: Summary of Strehl-ratio performance by NGS and LGS modes of AO188 under various observing conditions in K-band.

Observing condition	Strehl-ratio (K-band)	Guide star (V-mag)	Separation from guide star	Sky coverage
NGS (best)	$\approx 70\%$	8	$< 30''$	$< 0.1\%$
NGS (moderate)	$\approx 40\%$	12	$< 30''$	1%
NGS (worst)	$\approx 10\%$	16	$< 30''$	30%
LGS (best)	$\approx 45\%$	14	$< 80''$	30%
LGS (moderate)	$\approx 30\%$	16	$< 80''$	50%
LGS (worst)	$\approx 10\%$	19	$< 80''$	100%
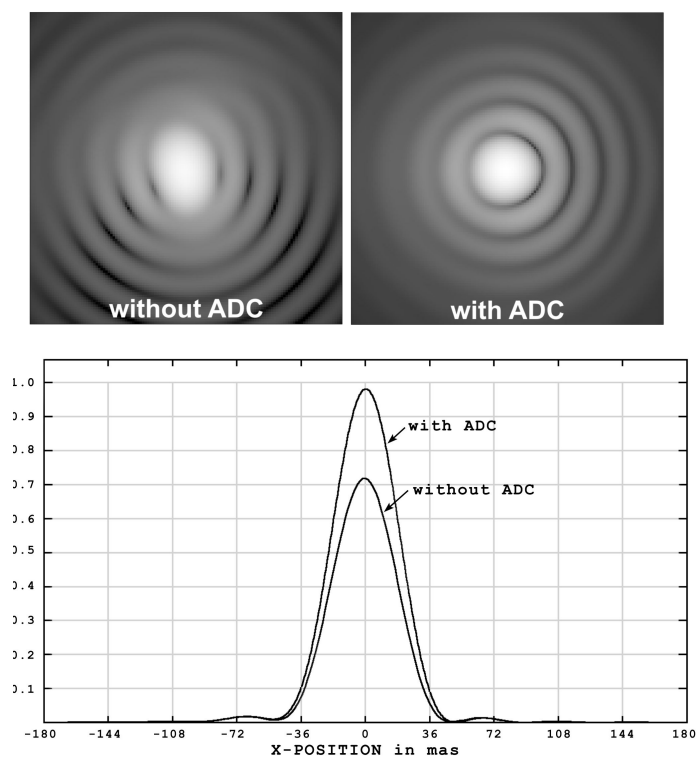
Figure 4.7: AO188 lab PSF (no central obstruction or spiders of the telescope) in H-band with and without the correction of the dispersion by the ADC unit. The Strehl ratio drops from 98% to 72% with and without the ADC unit. Image courtesy Egner et al. (2010)

4.3 The atmospheric dispersion compensator of AO188

In AO188 the atmospheric dispersion is compensated using a science path ADC (Egner et al., 2010) as shown in Fig. 4.6. As mentioned previously AO188 is used by two facility science instruments. Firstly, it is used by IRCS (infrared camera and spectrograph), which is an IR imager with J, H, K', K, L and M-band imaging that can also perform spectroscopy with a spectral resolution of up to 20000. Secondly, it is used by HiCIAO, a coronagraphic imager with three observing modes: direct imaging, polarization differential imaging, and spectral differential imaging. The science path ADC of AO188 was designed in consideration with the above two mentioned instruments. To achieve a diffraction limited PSF and a good Strehl ratio performance, compensation of atmospheric dispersion using an ADC is essential for both angular resolution and coronagraphic contrast.

The impact of atmospheric dispersion on Strehl ratio is shown in the Fig. 4.7. The figure presents a PSF taken of the internal source in the H-band with no central obstruction or telescope spiders. The PSF with atmospheric dispersion (corresponding to a zenith distance of $60°$ where the PSF elongates by a factor of 1.6) and no ADC correction can be seen in the top left panel of Fig. 4.7. The top-right panel shows the PSF with the ADC correction applied and a small amount of the coma aberration due to the dichroic mirror inside AO188. The presence of atmospheric dispersion affects the Strehl-ratio by $\approx 30\%$, as it dropped from 98% to 72% with and without the ADC unit.
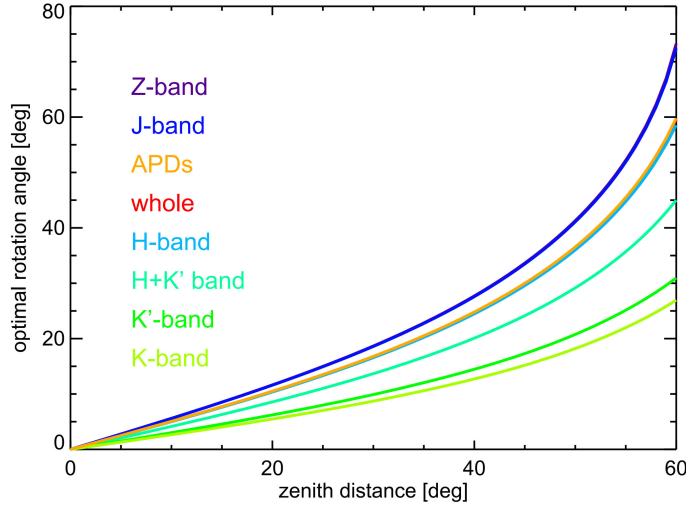
Figure 4.8: The optimal rotation angle α_{ad}, for the ADC prisms for various science filters as a function of the zenith distance. "Whole" stands for optimized rotation angle for broadband observation. Image courtesy Egner et al. (2010)

4.3.1   Requirement

The goal of the science path ADC was set by the IRCS and HiCIAO instruments, to achieve a good correction of dispersion in the optical for wavefront sensing and in the NIR for science observations, the following specifications of the ADC prisms were set (taken from Egner et al. (2010)):

1. Residual spot elongation after correction (imaging/spectroscopy): $< 10\%$ of diffraction-limited PSF.

2. Residual spot elongation after correction (coronagraphy): $< 1/30^{th}$ of diffraction-limited PSF diameter.

3. Spot motion during rotation: < 2 arcsec.

4. Working zenith distances: 0 to 63 deg.

5. Wavelength range: 0.45 to 2.2 micron.

The requirements are much tighter for HiCIAO as compared to normal ADC operation. To achieve the requirements outlined, a dedicated correction for each science filter of HiCIAO was necessary. A function c_f, optimized for each filter is given by Eq. 4.1 and is also shown in the Fig. 4.8. The function of the rotation angle (α_{ad}) of the prisms of ADC to correct for the dispersion is given by,

$$\cos\alpha_{ad} = c_f \tan z, \tag{4.1}$$

where z is the zenith distance, and c_f is the calibration factor, which depends on the science filter used. The rotation angle for various science bands is shown in Fig. 4.8.

Optical Design

The AO188 science path ADC unit consists of two identical prisms, placed close to the pupil plane in the collimated beam as shown in Fig. 4.6. The transmission curves of both the prisms are shown in the Fig. 4.9, which shows identical transmissive properties. The amount and direction of the compensation of dispersion are adjusted by rotating both prisms about the optical axis, in the same direction and with respect to each other.
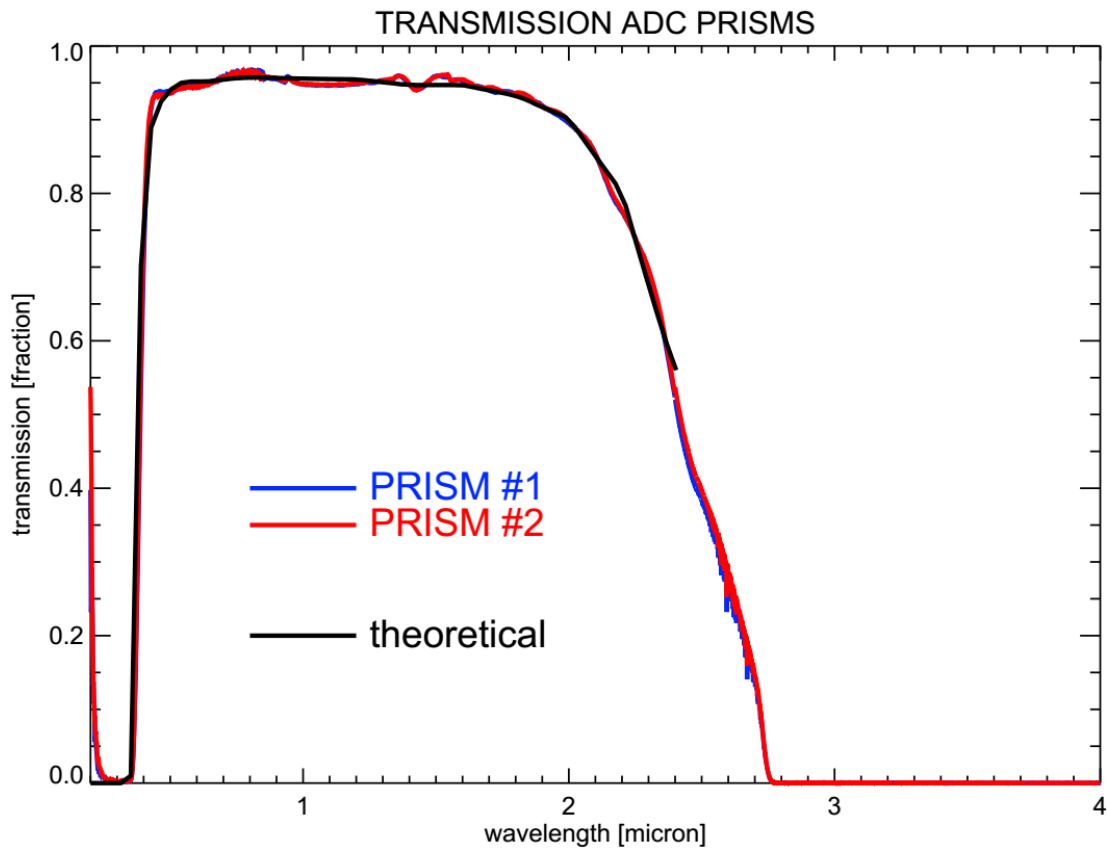
Figure 4.9: Transmission curve for both the prisms of AO188 science path ADC.

Mechanical design

To achieve a high-precision correction of the atmospheric dispersion places tight constraints on the mechanical structure of the ADC. Below are the critical specifications of the mechanical structure of the ADC unit (taken from Egner et al. (2010)):

1. insert / retract the unit within 20 seconds

2. repeatability of rotation: better than 0.087 deg

3. step size of rotation: less than 0.087 deg

4. backlash of rotation: less than 0.2 deg

5. maximum rotation velocity: more than 3.75 deg/sec

6. separation tolerance on prisms: better than 0.5 mm

7. tilt of prisms: less than 1.0 deg

8. tilt of entire unit: less than 1.0 deg

9. clear aperture: more than 120 mm
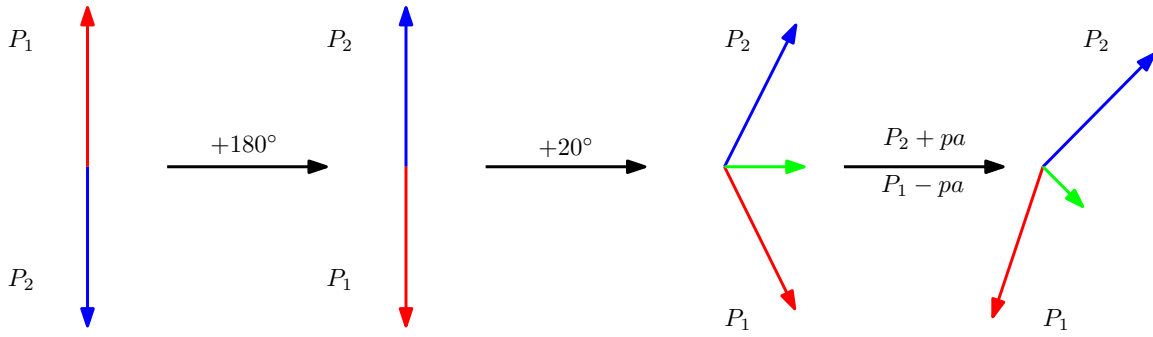
Figure 4.10: States of the ADC prisms P_1 and P_2 with various orientations. The green arrow shows the dispersion compensation vector implemented by the ADC prisms. The first position corresponds to the base position of the ADC. The second, to the telescope pointing at zenith. The third, for a certain zenith angle. The Fourth position corresponds to SCExAO's mode of observation (see description).

4.3.2   Operation of the ADC

To correct the atmospheric dispersion in closed-loop it is important to understand the how the ADC works and its correction procedure, so that correct offsets to the prisms of the ADC can be applied to correct the residual dispersion. Figure 4.10 shows states of the two ADC prisms for various orientations. Initially, the prisms P_1 and P_2 are parked in a position called the base position as shown in the first schematic in the figure. Prisms P_1 and P_2 rotate anti-clockwise and clockwise respectively. After 180° of rotation, they interchange their position and this configuration corresponds to the telescope pointing at zenith. Note that the two prisms are oriented opposite one another canceling each other out as there is no contribution of dispersion from the atmosphere at zenith. As the telescope points away from zenith, the prisms change their orientation to generate a compensation vector. For a 20° prism offset, the compensation vector is given by the green arrow as shown in the third schematic in Fig. 4.10. SCExAO operates in fixed pupil mode and internal mask of SCExAO is rotated by −39° (to mask the dead actuators of SCExAO's DM), which is adjusted by giving a pa offset of −39° to both the prisms, shown in the last schematic. The on-sky telescope elevation axis / atmospheric dispersion direction is always opposite green arrow in fixed pupil mode. The next aspect to consider is the rotation speed of the prisms. This was tested to determine the time taken to complete the rotation once the command was sent from SCExAO computer.

The result of such a speed test is summarized in the Table 4.4. From the mechanical specification mentioned above the prisms can rotate at a speed of 3.75 deg/sec but the prisms rotate one at a time (there is no independent rotation of the prisms). By inspecting the results in the table, it becomes clear that at present there is few seconds of time delay between when the command is issued from SCExAO's computer and the execution of the command by the AO188 computer. In future, this delay needs to addressed in order to drive the loop at high speed.

4.4   Experimental setup

The measurement of dispersion utilizes modules inside SCExAO and correction is done by driving the science path ADC inside AO188. The calibration speckles are generated by the DM of SCExAO as shown in Fig. 4.11 and images are acquired using internal NIR camera. The measurement

Table 4.4: Estimate of the time taken by ADC prisms to rotate by certain offsets, from the time command was issued from the SCExAO's computer.

P_1 offset (deg)	P_2 offset (deg)	Approximate time taken (sec)
1	2	4
3	2	5
0	5	4
5	0	4
5	5	5
10	0	7
0	10	7

of dispersion is done using the concepts explained in the previous chapter. Once the presence of dispersion is calculated (using SCExAO's computer), correction offsets are sent the AO188 computer, which is then applied to the ADC prisms. The detailed explanation is provided in the next section.

4.4.1 Control architecture

The control architecture behind the measurement and correction of dispersion is shown in the Fig. 4.12. The look-up table box shown in the Fig. 4.12 calculates the ADC prism angles θ_1 and θ_2 based on the elevation of the telescope and then these angles are sent to the ADC. Science image box in the figure represents the measurement of residual dispersion inside SCExAO using DM and internal NIR camera, as explained previously. The residual dispersion vector measured from the science image is then multiplied by the applied gain. The amount of residual dispersion needs to be corrected is the sent ADC solver (see section 3.5), which computes the ADC prism offsets $\delta\theta_1$ and $\delta\theta_2$. The correction offsets $\delta\theta_1$ and $\delta\theta_2$ are then sent to ADC prisms, which are applied as offsets to the look-up table based correction.

4.5   Software architecture

The software control behind the measurement and correction of dispersion is done using a combination of Python and bash languages. The measurement of dispersion is done using Python scripts and correction to the ADC of AO188 are applied using bash scripts. Various scripts behind the process were integrated into an ASCII based graphical user interface (GUI) for the ease of operation is shown in Fig. 4.13. With the aid of GUI, various scripts can be executed with low latency, which is explained in detail,

1. **Add Speckles:** It sends a command to the DM of SCExAO to generate calibration speckles and changes filter to y-H band.

2. **SYNC ADC with AO188:** Takes control of ADC from main AO188 control software so that ADC prisms can accept offsets from SCExAO computer.

3. **ADC Calibration:** Measures residual dispersion for two configurations of ADC and computes the ADC dispersion magnitude.
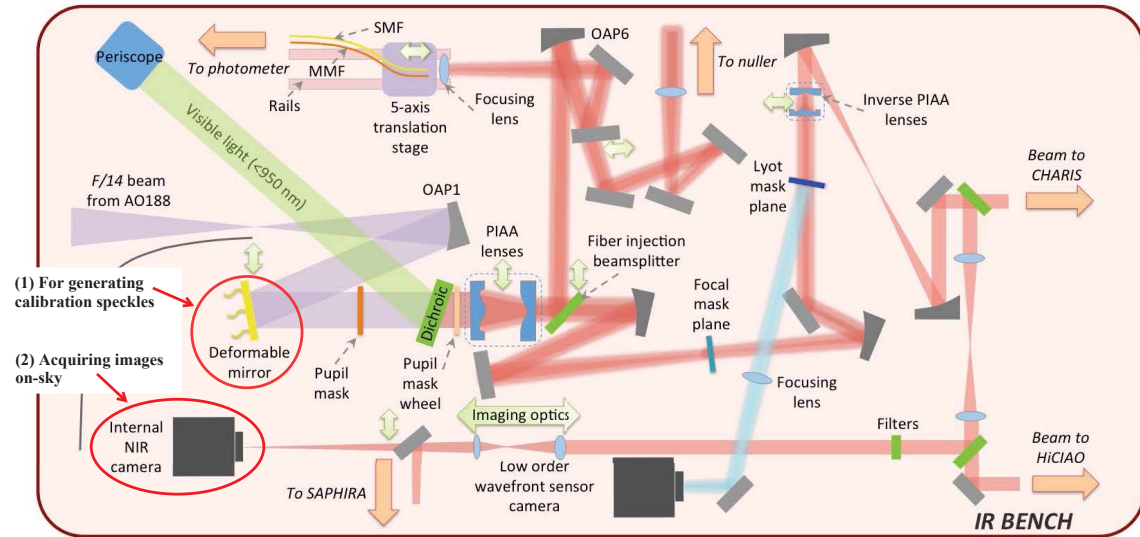
Figure 4.11: Schematic showing the IR bench of SCExAO, DM and internal NIR camera of SCExAO, which are used for the measurement of dispersion.

θ_1 & θ_2 are prism 1 and prism 2 angles calculated using look-up table.

$\vec{r}$ is measured residual dispersion.

$\delta\theta_1$ & $\delta\theta_2$ are offset angles for prism 1 and prism 2.

Closed-loop correction is represented by blue colored arrows.
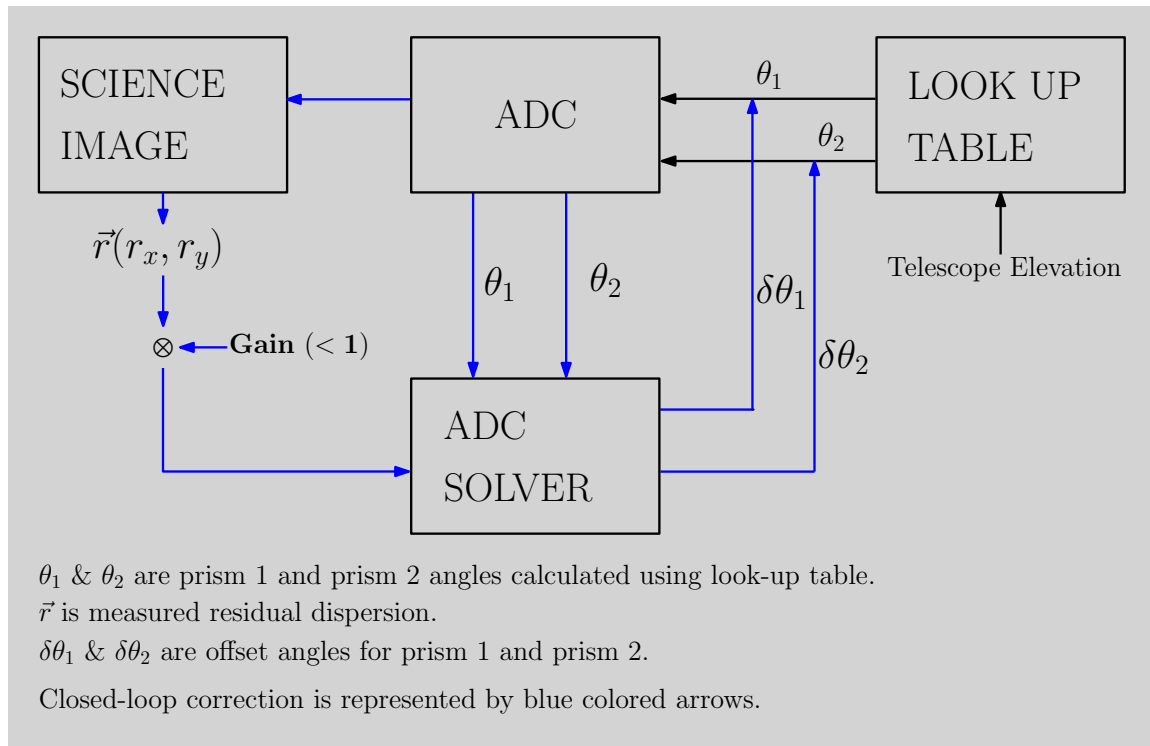
Figure 4.12: Schematic showing the control architecture behind the measurement and correction of dispersion.
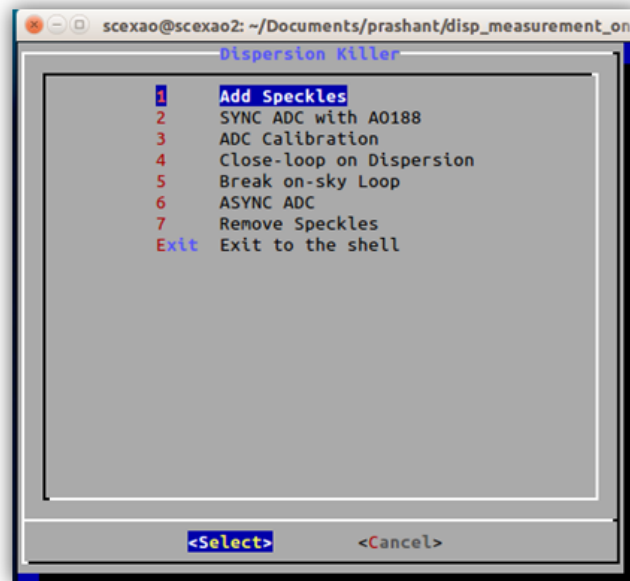
Figure 4.13: The graphical user interface for software control behind measurement and correction of dispersion.

4. **Close-loop on Dispersion:** Closes the loop on dispersion for an applied gain and sends offsets for correction to the prisms of ADC (to AO188 computer via ssh).

5. **Break on-sky Loop:** Breaks the closed-loop correction.

6. **ASYNC ADC:** Reverts the control of the ADC to AO188 control software.

7. **Remove Speckles:** Removes the calibration speckles applied using the DM of SCExAO.

4.6 Summary

In this chapter, I provided a description of the SCExAO and AO188 and their modules. I also discussed how the DM of SCExAO can be used to generate focal plane calibration speckles, which are used for the measurement of dispersion using the images taken by internal NIR camera of SCExAO. The science path ADC of AO188 was discussed in detail, which is used for the correction of dispersion after its measurement using SCExAO. With the concepts and algorithms discussed in the previous chapter and using the hardware tools presented in this chapter, the on-sky measurement and correction of the dispersion are discussed in the next chapter.

On-sky Validation

In this chapter, I present the measurement of dispersion using an adaptive calibration speckle grid. Previously, this ability to arbitrarily generate speckles has been used to systematically remove speckles in the PSF halo (Martinache et al., 2014a) and more recently for high precision astrometry using incoherent speckles (Jovanovic et al., 2015a). Here we present the measurement of on-sky dispersion using an adaptive speckle grid generated using the DM of SCExAO, which can be modulated to create a grating structure in the form of a sine wave. The distance between the PSF core and the resulting speckles is a function of the number of periods across the pupil. The more cycles per aperture the sine wave has, the further a speckle is projected from the PSF. With 45 actuators across the pupil, the furthest speckles can be placed is 22.5 λ/D from the PSF (Jovanovic et al., 2015b). The brightness of the speckles can be controlled by adjusting the amplitude of the sine wave.

5.1 Data acquisition

For all the on-sky testing, the data was collected using the Subaru Telescope facility AO system, AO188 (Minowa et al., 2010) and SCExAO. SCExAO receives light from AO188 and utilizes the partially corrected PSF fed by AO188. In closed-loop, AO188 offers Strehl ratios in the H-band between $20\% - 40\%$ and SCExAO boosts that Strehl ratio to $70\% - 90\%$. The following settings were used for the experiments throughout this chapter:

- Only AO188 correction was utilized. The ExAO correction was not used.

- The focal plane speckles were generated using the DM of SCExAO and positioned at 22.5 λ/D (separation from the PSF core), with a 100 nm RMS amplitude on the DM.

- Science path images were acquired using the internal NIR camera in SCExAO (320×256 pixels, InGaAs detector) for bandwidth spanning y-H bands.

- The measured residual dispersion was corrected by driving the ADC prisms located inside AO188 (Egner et al., 2010).

- For image processing, an averaged dark was calculated from a cube of 1000 dark frames, then subtracted from the science path images. The Hot pixels were also removed.

5.2 Presence of on-sky dispersion

To show the presence dispersion in an on-sky image, the data was collected on the target β Leo (spectral type A3, R-mag= 2.08, H-mag= 1.92) on SCExAO's engineering night of April 2nd, 2015.

An image was collected with a band spanning from y to H band, by the NIR camera. At the time of the test, the telescope elevation was $43°$ and no look-up table based ADC correction was applied to highlight the presence of atmospheric dispersion. As shown in Fig. 5.1, the speckles do not point to the PSF core and deviation of the radiation center confirms the concept and simulations presented in Chapter 3. The figure shows the approximate location of the radiation center with respect to the PSF core. The fact that these two are not co-located indicates that dispersion is present.

The calibration speckles in the image produce a low-resolution spectrum spanning y-H band, with shorter wavelength closer to the PSF and vice-versa. This wavelength dispersion in the off-axis speckles is a result of the wave (diffractive) nature of light. The water absorption due to the atmosphere can be seen as a gap between J and H-band. The presence of dispersion in the PSF can be estimated by accurately measuring the location of the radiation center from the PSF core, as explained in the Chapter 3. In the next section, I present the on-sky result for measurement of the radiation center and estimation of the dispersion in science images.
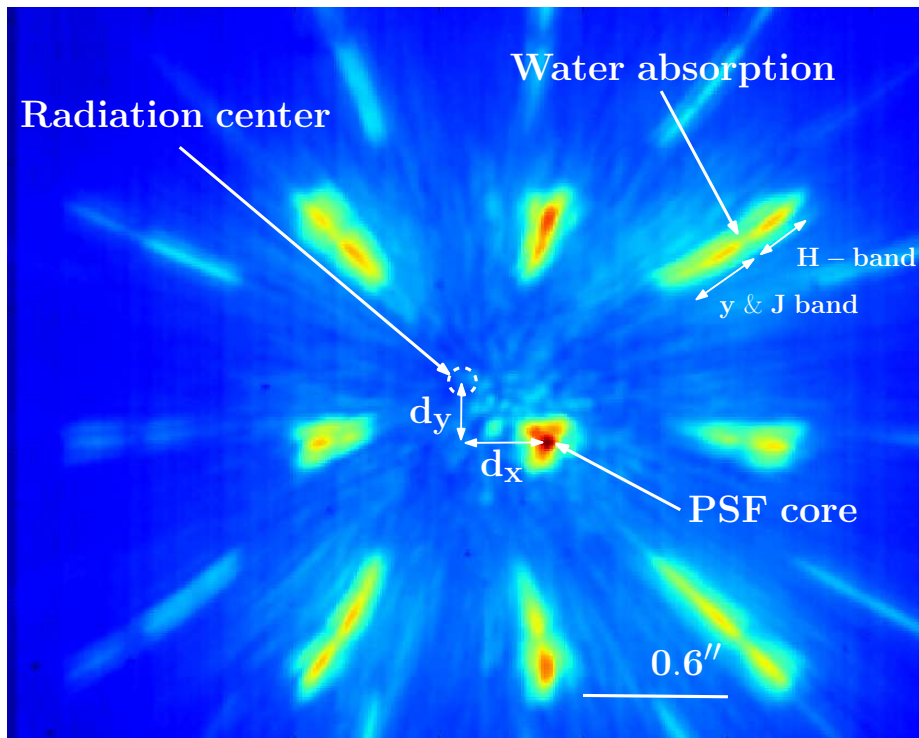
Figure 5.1: On-sky PSF, showing the radiation center and PSF core. The deviation of the radiation center from the location of the PSF core shows the presence of atmospheric dispersion.

5.3 Measuring dispersion

5.3.1 Fitting lines to speckles

To find the location of the radiation center, the first and obvious approach was to fit lines to the diagonal calibration speckles and find the closest point to all the four lines, as a proxy for the intersection between the lines (due to measurement noise, it is generally not possible to get all the lines to pass through a single point). To fit the lines to the speckles, a 1-D Gaussian was fitted to each

row across a given speckle, and the location of the peak value for each Gaussian was used to extract the orientation and position of each speckle. This method worked well for y-J band and H-band. As can be seen in Fig. 5.1, the on-sky speckles suffer from WFE and water band absorption, which made it difficult to fit a line robustly to each speckle. The speckle fitting process was contingent on the seeing and AO correction delivered by AO188. This method also relied heavily on the brightness of the speckles, which limited our measurement to bright targets only. This fitting technique was tested with on-sky data and did not yield reliable values for the location of the radiation center. So an alternate approach was developed, which proved to be precise and robust to poor AO corrections. The results of this technique are discussed in the following section.

5.3.2 Using raster scan

In Chapter 3, I outlined a technique to measure the radiation center, which is based on a raster scan around the PSF minimizing the norm of the difference between original and stretched images. Extraction of the radiation center for an on-sky data required additional image processing steps (like background removal, explained later) compared to that of the simulated PSF images. The following steps were used for the extraction of the radiation center from an on-sky data, first: the location of the PSF core was found by using the center of gravity method. After finding the PSFs location, it was masked by a square array to remove the PSF core (by setting the pixel values to zero). The image after masking consisted of eight speckles, which were then thresholded to remove the background and then a raster scan, as outlined in Chapter 3 was used to find the radiation center. The intermediate result of such a process is shown in the Fig. 5.2. The figure shows subtraction of original (speckles in green) and stretched (speckles in red) images (radially stretched copy of the original image), the green colorbar shows counts (positive) for the original image and red colorbar (negative counts) for the subtracted stretched image. Figure. 5.2 (a) represents a case when the stretch and subtraction were from a pixel coordinate closer to the radiation center and it can be seen from the figure (see red circle) original and stretched images overlap and in between the speckles there are regions with close to zero counts. Figure 5.2 (b) Shows subtraction of images from pixel coordinate far from the radiation center, original and stretched images do not overlap. The norm of the difference for Fig. 5.2 (b) will give higher counts of all pixels compared to the Fig. 5.2 (a).

The on-sky measurement of the radiation center and estimation of the dispersion in the science images was achieved on the target α Ari (spectral type K1, R-mag= 1.15, H-mag= -0.52) on SCExAO's engineering night of October 30th, 2015. Figure 5.3 (a) shows the satellite speckles and the PSF core, with superimposed lines (manually overdrawn), showing that the radiation center lies away from the PSF core. Figure 5.4 shows the results of the measurement of the radiation center on the science images shown in Fig. 5.3. Figure 5.4 (a) shows the offset of the radiation center (given by the minimum in the contour plot) from the PSF core (located at $(0,0)$ coordinate). The angles of the two prisms of the ADC at the time of the measurement of the radiation center were $\theta_1 = 141.8°$ and $\theta_2 = 219.8°$. Using the relationship between offset of the radiation center from the PSF core and dispersion given by Eq. 3.19, the dispersion in the PSF was estimated to be 20 $mas/\mu m$. Full results are summarized in the Table 5.1. After determining the dispersion, the ADC prisms were offset by $10°$ in the rotation and the dispersion was once again measured for the calibration of the ADC. By utilizing the measurements of dispersion pre and post ADC offsetting, the on-sky dispersion was estimated. Then a new position of the ADC prisms was calculated to cancel the estimated on-sky dispersion. The ADC prisms were driven to a new position to make the radiation center coincide with the PSF core. The new rotation angles were determined to correct for on-sky dispersion, $\theta_1 = 112.1°$
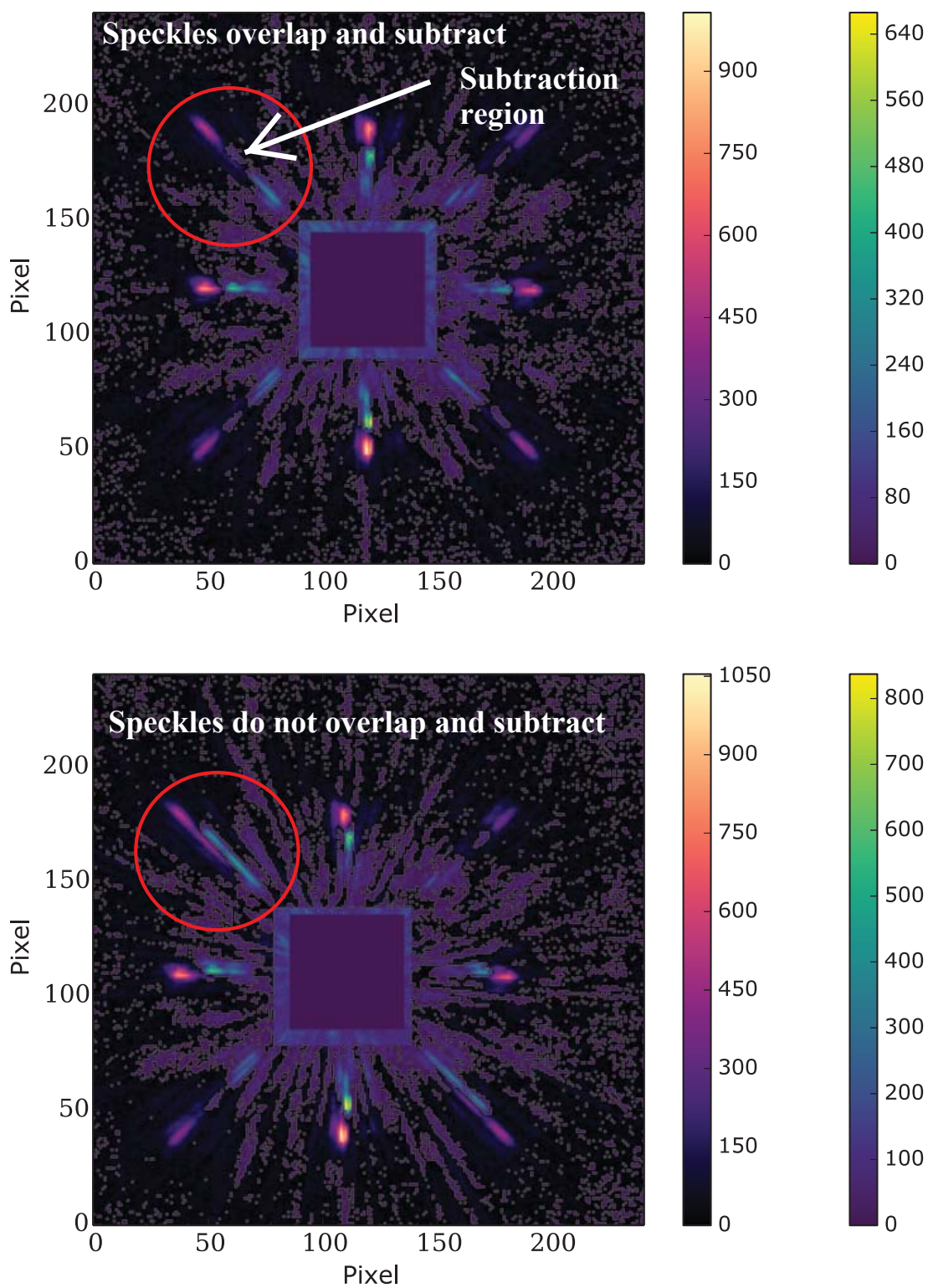
Figure 5.2: Subtraction of original (green) and stretched (red) images to find the location of the radiation center. (a) Subtraction of images from a pixel coordinate closer to the radiation center: original and stretched images overlap. (b) Subtraction of images from a pixel coordinate far from the radiation center: original and stretched images do not overlap. The color bar on the left represents negative values and one on the right for positive values.

Table 5.1: Measurement of the radiation center and estimation of the corresponding dispersion.

	d_x	d_y	PSF spread
	mas	mas	$mas/\mu m$
Without correction	-3.6 ± 8.3	41.6 ± 8.0	20.9
With correction	7.7 ± 6.5	-5.3 ± 8.4	4.7

and $\theta_2 = 255.4°$. After correction, the result is shown in Fig. 5.4 (b), which demonstrates that the PSF core now overlaps well with the radiation center, compared to the Fig. 5.4 (a). Figure 5.3 (b) shows the added speckles after correcting for residual dispersion. Here the intersection point lies close to the PSF core, as shown in the inset of the Fig.5.3 (b) compared to (a).

Table 5.1 summarizes the results of the measurement of the radiation center and the corresponding dispersion estimates from it, before and after correction. The values of d_x (x-axis) and d_y (y-axis) shown in the table represent the distance between the radiation center and the PSF core, in units of milliarcsecond converted from pixel values (using the known plate scale of 12.1 mas/pix in our NIR camera [1]). The values of d_x and d_y are then converted into PSF elongation by the relationship between distance and dispersion given in Eq. 3.19. Table 5.1 shows that in a single iteration, we have reduced the residual atmospheric dispersion from 20.9 $mas/\mu m$ to 4.7 $mas/\mu m$, which corresponds to 4.2 mas in the y-H band and 1.4 mas in H-band alone.

This section discusses the on-sky measurement and correction of the dispersion in a single iteration, which was published in Pathak et al. (2016). The next section discusses closed-loop measurement and on-sky correction of dispersion, which provided a superior correction of the dispersion than the single step correction.

5.4 Closed-loop

The on-sky closed-loop correction of residual dispersion was achieved on the target β Andromedae (spectral type M0, R-mag $= 0.81$, H-mag $= -1.65$) on the SCExAO engineering night of September 19th, 2016. The on-sky loop for measurement of the residual dispersion runs at a speed of 10 Hz but the correction loop speed is set by the AO188 ADC prisms rotation speed, which is ≈ 4 sec for a $5°$ rotation (see Table 4.4). Here an average of 20 measurements (exposure time for each measurement: 50 μsec) was used to average dispersion due to atmospheric tip-tilt, which is discussed in section 5.9.1. The presence of residual dispersion in the final science images is the sum of dispersion from the internal optics and imperfect compensation of the atmospheric dispersion by the ADC. More details about dispersion due to internal optics can be found in section 5.5. The residual dispersion (elongation in the PSF) from Eq. 3.21 can be written as a vector sum of its x and y components, $\overrightarrow{r}_{on-sky} = \overrightarrow{r_x} + \overrightarrow{r_y}$ in the focal plane. The closed-loop correction of residual dispersion was tested on-sky with two loop gains (20 and 50%). The vector components of residual dispersion after each iteration of the loop are shown in Fig. 5.5. The performance of the closed-loop test is analyzed by fitting the data points with an exponential function of the form $y = a \times \exp(-b \times x) + c$.

---

[1]Note: this plate scale value changes after SCExAO rebuild. A different plate scale value of the NIR camera is used in rest of the results.
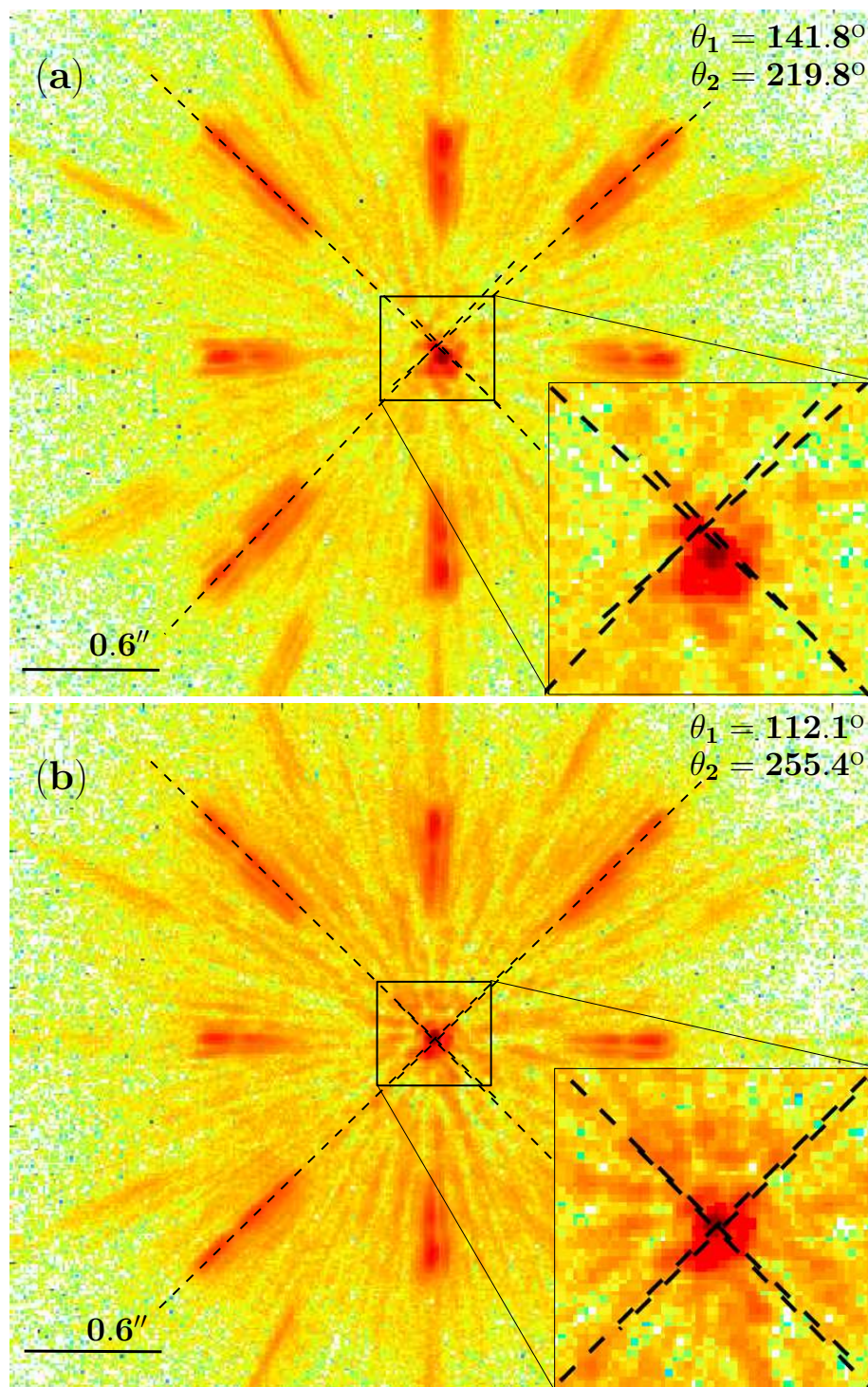
Figure 5.3: PSF with added speckles, θ_1 and θ_2 give the actual prisms angle. (a) Before correcting the residual atmospheric dispersion (fitted lines are over-plotted to show that the radiation center does not coincide with the PSF core). (b) After correcting the residual dispersion (the over-plotted lines show the radiation center coincides with the PSF core).
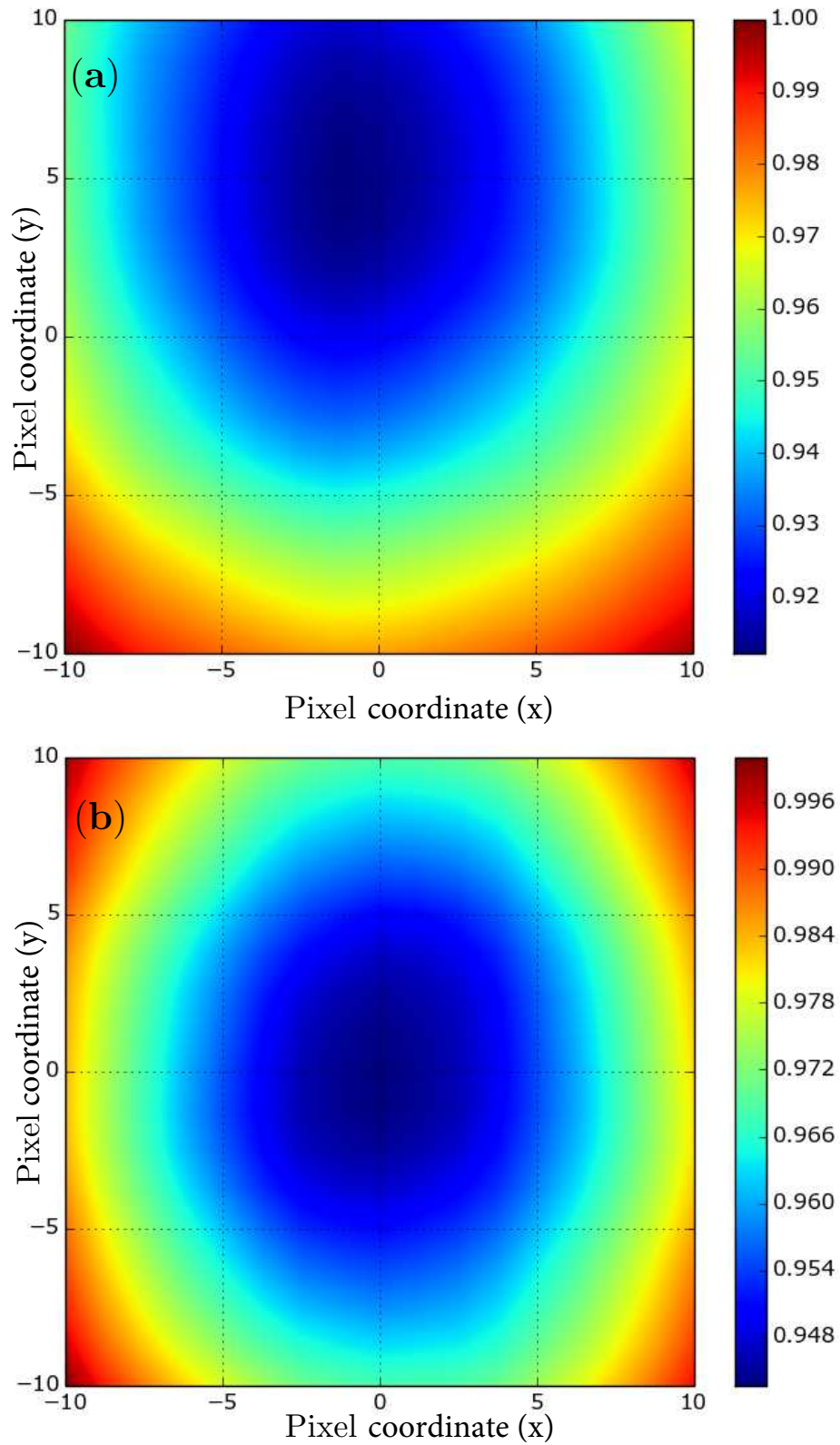
Figure 5.4: On-sky results: offset of the radiation center from the PSF core. The colorbar represents the relative intensity (see Sec. 3.3.2). (a) Before correcting the residual atmospheric dispersion. (b) After correcting the residual atmospheric dispersion.

Table 5.2: Closed-loop fitting parameters.

	a (mas/μm)	b (iteration^{-1})	c (mas/μm)
$r_x(20\%)$	-28.92	0.16	0.95
$r_y(20\%)$	-17.36	0.19	0.46
$r_x(50\%)$	-45.77	0.60	0.22
$r_y(50\%)$	-26.13	0.57	0.06

Exponential functions are adequate for fitting and analyzing performance of data, y reduces as a function of x (time or iteration), c is the final convergence point, b is the gain (each loop iteration reduces residual dispersion in this case by applied gain < 1.0), and a is starting value of y. The parameters of the fit for both the loop gains are shown in the Table 5.2.

The performance of both the loops can be estimated by parameter b and c. The parameter b shows the decrease in the residual dispersion as a function of iteration, for loop gains of 20% and 50% it is close to 0.2 (iteration^{-1}) and 0.5 (iteration^{-1}) respectively, which shows a reduction in the residual dispersion values as a function of applied gain. The loop converges faster for a loop gain of 50% as one would expect. The convergence performance of the loop is given by parameter c. Which should be equal to zero for an ideal closed-loop correction. The value of c are smaller for the loop gain of 50% compared to the loop gain of 20%, which shows a better convergence for a loop gain of 50% compared to 20%. This was due to the low number of iterations used for the test. However, the loop converges approximately to the same level of correction for both gains used. Here we demonstrate that in closed-loop we can correct for dispersion arising from the atmosphere as well as due to internal optics.

The result of the closed-loop test is presented with a scatter plot in the Fig. 5.6. Figure 5.6 shows the residual dispersion vector in the camera plane before and after closing the loop. The data points presented in the scatter plot represent 1000 individual measurements with 50 μsec exposure time. The plot clearly shows that after the loop was closed the average of the residual dispersion was centered around zero dispersion. The average value of atmospheric dispersion went from 26.64 ± 0.07 mas/μm to 0.95 ± 0.08 mas/μm, which corresponds to an average PSF elongation (dispersion) of 7.99 ± 0.02 mas to 0.28 ± 0.02 mas in H-band before and after the correction respectively. The limitation to the accuracy of measurement and correction consists of various error terms which are discussed in section 5.9.1.

5.5 Open-loop dispersion measurement

In this section I present the result of residual dispersion measurements ($\vec{r}_{on-sky}$ in Eq. 3.21), which are taken with look-up table based control of the ADC applied. The aims of the experiment are:

- Analyze the performance of the look-up table based ADC correction as a function of telescope elevation and varying atmospheric conditions.

- Estimate the presence of dispersion due to internal optics.
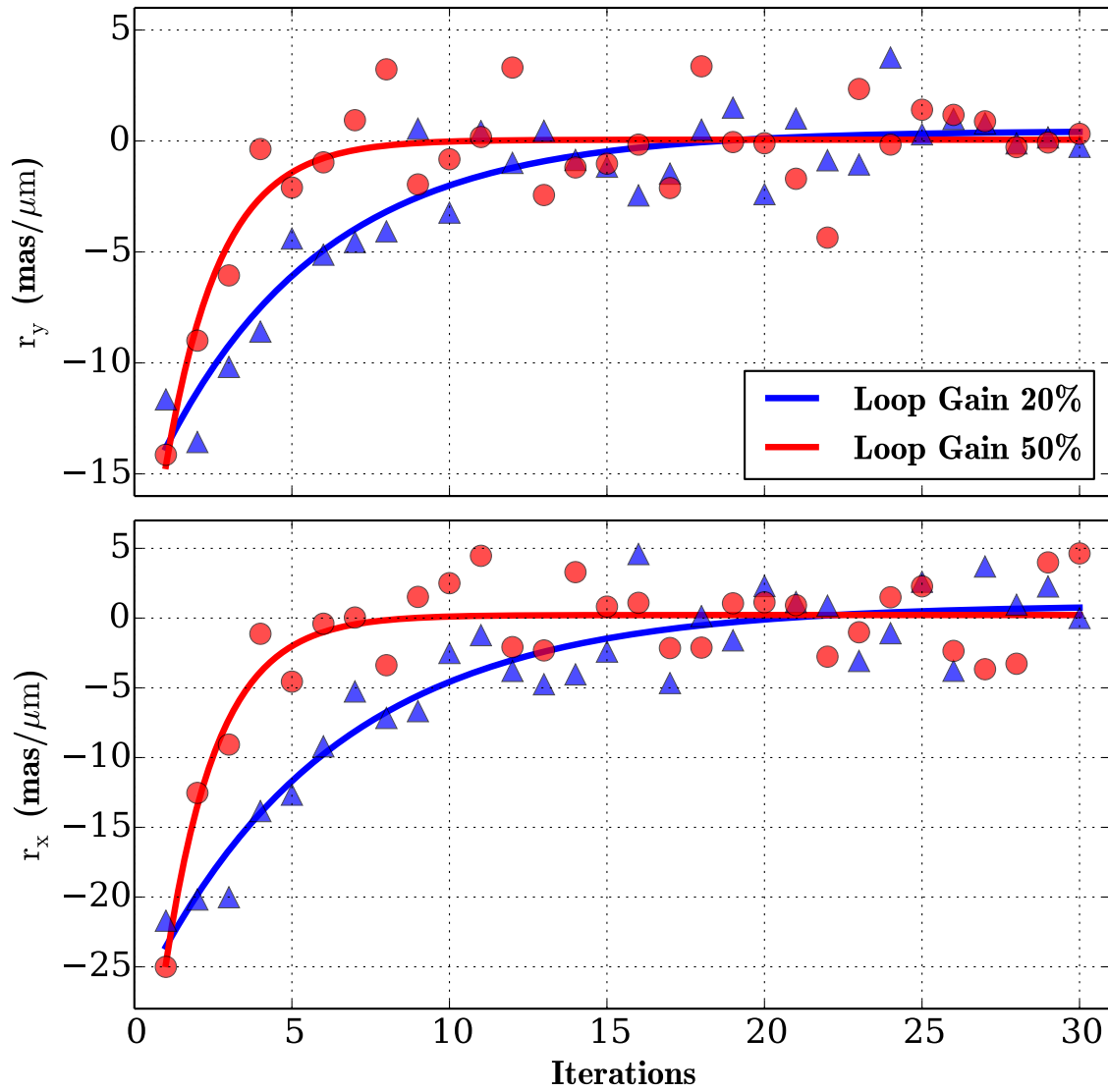
Figure 5.5: On-sky closed-loop correction of the residual dispersion vector for two loop gains. For the larger gain, the loop converges faster compared to the smaller gain.
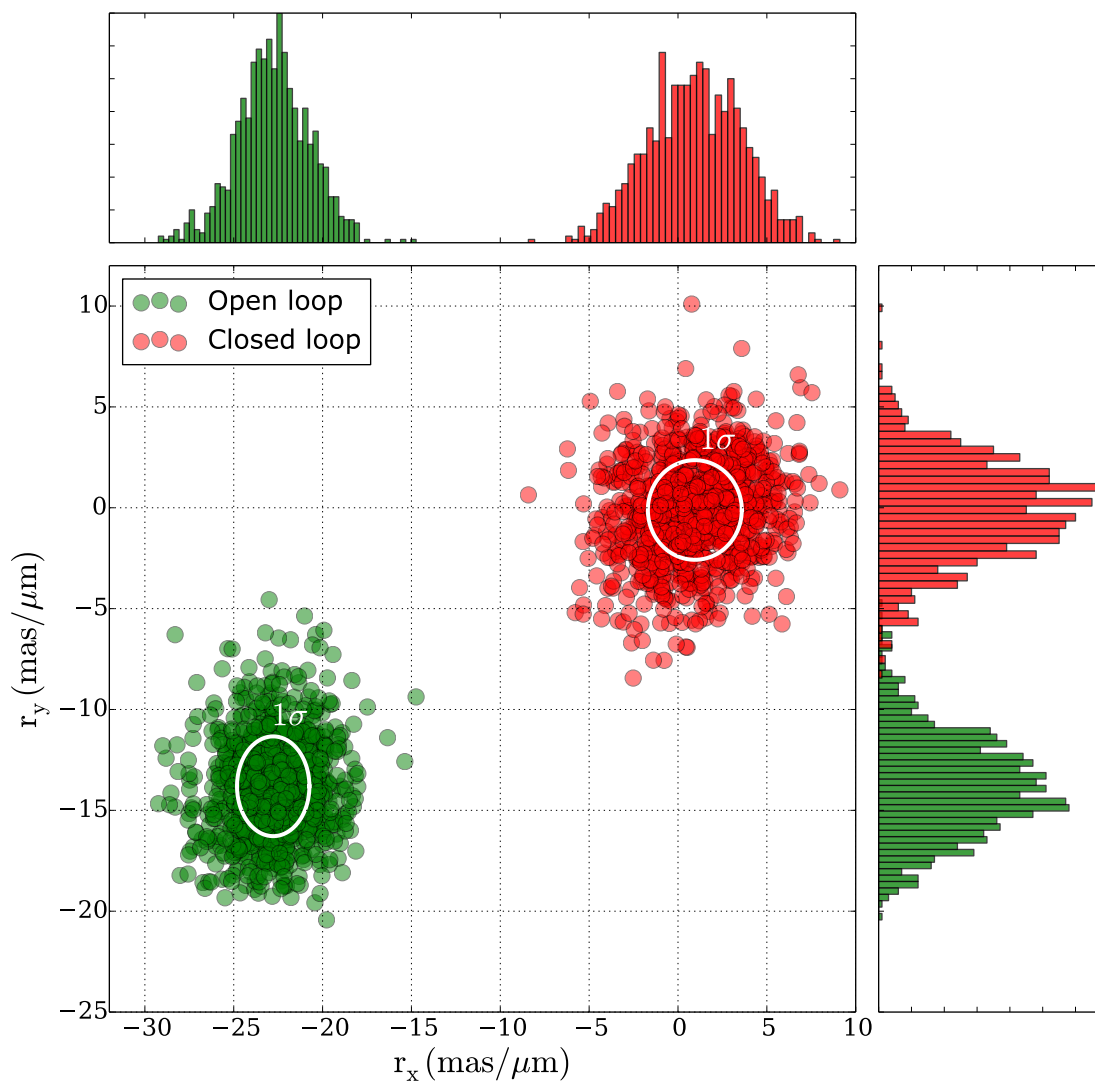
Figure 5.6: Scatter plot showing the position of residual dispersion vectors before and after closing the loop with respect to the pixel coordinate system of the NIR internal camera. In closed-loop, the residual dispersion vector is centered around zero dispersion.
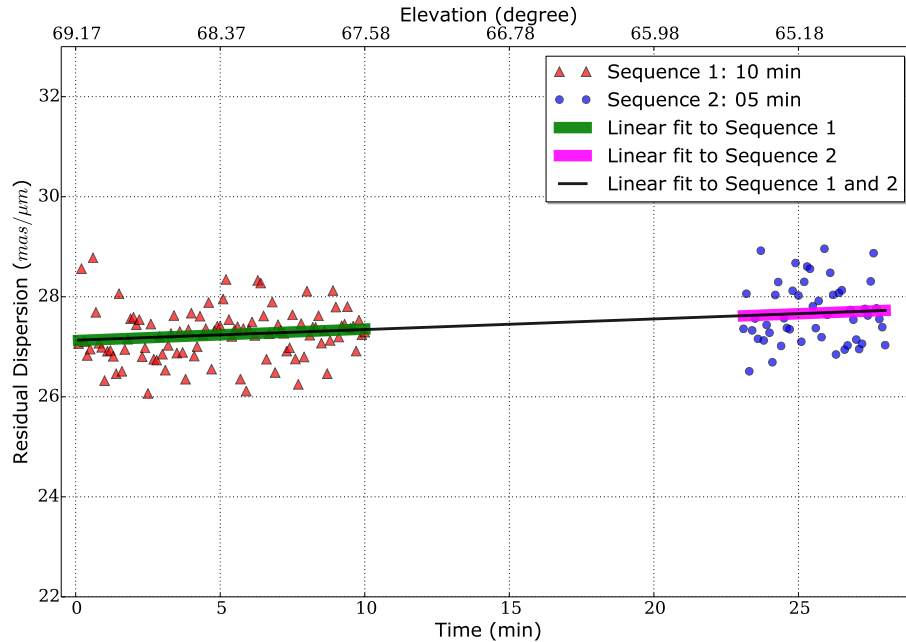
Figure 5.7: Measurement of the residual dispersion (using look-up table based correction) with a change in the telescope elevation for two time blocks of 10 and 5 minutes. The measured values of residual dispersion show an upward trend as the telescope elevation decreases.

- Understand sources contributing to the presence of residual dispersion in the final science image and how frequently dispersion needs to be corrected.

The on-sky measurement of residual atmospheric dispersion was performed on the target β Andromedae (spectral type M0, R-mag = 0.81, H-mag = -1.65) on a SCExAO engineering night on September the 19th, 2016. Figure 5.7 shows the measured residual dispersion as a function of time as well as pointing of the telescope (elevation). Two sequences of data were collected for 10 minutes and 5 minutes, separated by 13 minutes. Each sequence of data was fitted with a line (green color for sequence 1 and magenta for sequence 2), and a global fit was also calculated for the whole experiment, shown by the black line. It is clear that the global fit overlaps well with the two individual sequence fits, indicating that there a linear relationship between elevation angle and residual dispersion for short periods of time at least. During the 30 min window of data collection, we observed a relatively small increase in the residual dispersion as a function of decreasing elevation angle, which may be due to over- or under compensation of the dispersion by the ADC. To determine the effect of large elevation angle changes on the residual dispersion, the experiment was repeated and is discussed next.

5.6 Dispersion at different telescope elevation

In this section, I present the estimation of dispersion due to the atmosphere and internal-optics from measured values of residual dispersion as given by Eq. 3.21. We also show dispersion vectors of Eq. 3.21 for various telescope elevations in the arbitrary orientation of the internal NIR camera (telescope elevation axis is fixed). The motivation for using vector representation is that it allows
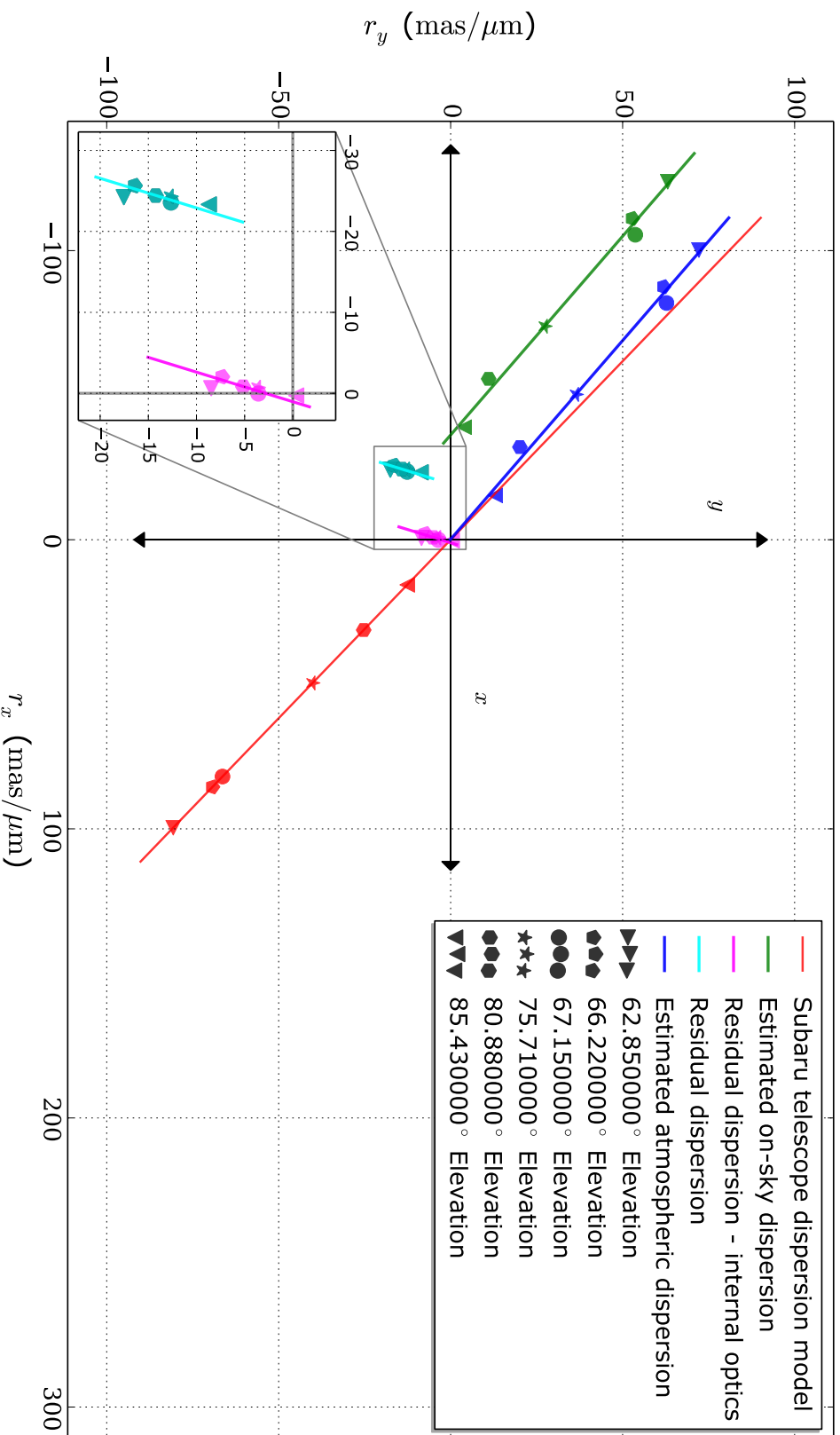
Figure 5.8: Vector representation of different dispersion (elongation in the PSF for y-H band) values in the arbitrary orientation of the internal NIR camera (telescope elevation axis is fixed) for the different telescope elevations (shown by different symbols). After correcting for the internal optical refraction, atmospheric dispersion vector becomes opposite to the ADC vector with small residual dispersion resulting from varying atmospheric conditions.

us to visualize and understand the various sources of dispersion, their magnitude, and direction in the focal plane of internal NIR camera, which we are most familiar with. The data was collected on December the 13th, 2016 on the targets α Ari (spectral type K1, R-mag = 1.15, H-mag = -0.52) and 51 Eri (spectral type F0, H-mag = 4.77) with significant changes in the telescope elevation. Figure 5.8 shows dispersion as a function of telescope elevation for several configurations (encoded by different symbols), each symbol represents the magnitude and direction of dispersion vectors. The on-sky residual dispersion vectors are shown in cyan symbols, the dispersion compensation vectors produced by the Subaru ADC in red symbols and the estimated on-sky dispersion vectors in green symbols. The estimation of these dispersion vectors is explained later in this section. The magnitude of the ADC compensation vector increases with decreasing telescope elevation to account for the increase in the dispersion. The SCExAO instrument operates in fixed telescope pupil mode so that imaging techniques such as ADI can be utilized. Due to the fixed pupil mode, the elevation axis of the telescope is fixed in the camera plane and it is oriented at 39° from the vertical direction. The red-line fitting ADC dispersion vectors show the direction of elevation axis in the internal NIR camera plane, which is indeed at 39° from the y-axis. The values of the on-sky dispersion were estimated by subtracting the ADC dispersion $\vec{a}_{ADC}$ from the residual dispersion $\vec{r}_{on-sky}$, as explained by Eq. 3.23. As can be seen from Fig. 5.8 the compensation of on-sky dispersion by the ADC WAS not optimum: the residual dispersion (cyan) and on-sky dispersion (green) values at 85.43°($\triangledown$) telescope should be ≈ 0. Also, the on-sky dispersion values $\vec{d}_{on-sky}$ have a constant offset, due to the presence of dispersion from the internal optics $\vec{d}_{internal}$, as explained in Eq. 3.22.

The presence of dispersion due to internal optics is best estimated when the telescope is pointing at the zenith. The static component of the atmospheric dispersion becomes zero, while the dynamic dispersion due to atmospheric tip-tilt remains, as well as the constant contribution from the internal optics. The dynamic contribution can be averaged to estimate only the dispersion due to internal optics and Eq. 3.21 reduces to,

$$\vec{r}_{on-sky} = \vec{d}_{internal\_optics}(at\ zenith). \tag{5.1}$$

The effect of atmospheric tip-tilt on dispersion is discussed in section 5.9.1 in greater detail.

The calculation of dispersion due to internal optics can be estimated by fitting a line to the values of on-sky residual dispersion as a function of elevation and finding the value of residual dispersion at an elevation of 90°. We estimated the dispersion due to internal optics to be 18.9 mas in the y-H band (elongation in the PSF). The estimated value of dispersion due to internal optics contains error terms due to varying atmospheric conditions and error in the measurement of residual dispersion at various telescope elevations. After the estimation of dispersion due to internal optics, it was subtracted from residual and on-sky dispersion values to give atmospheric and residual dispersion values (free from dispersion due to internal optics), which are shown in blue and magenta symbols respectively. As shown with magenta symbols, the residual dispersion increases with the decrease in the telescope elevation. We conclude from the figure that the presence of dispersion due to internal optics can lead to imperfect compensation, even when the theoretical look-up table utilized for compensation is accurate. This is expected as the model is not aware of any instrumental biases. The blue symbols show the estimated values of atmospheric dispersion (free from the component due to the internal optics), and it is clear that the data does not overlap with the red line used to fit the data points to the ADC compensation. This imperfect compensation creates the residual in magenta, which increases with decreasing telescope elevation. This is due to varying atmospheric conditions during the night of observation and its effect increases with decreasing telescope elevation.
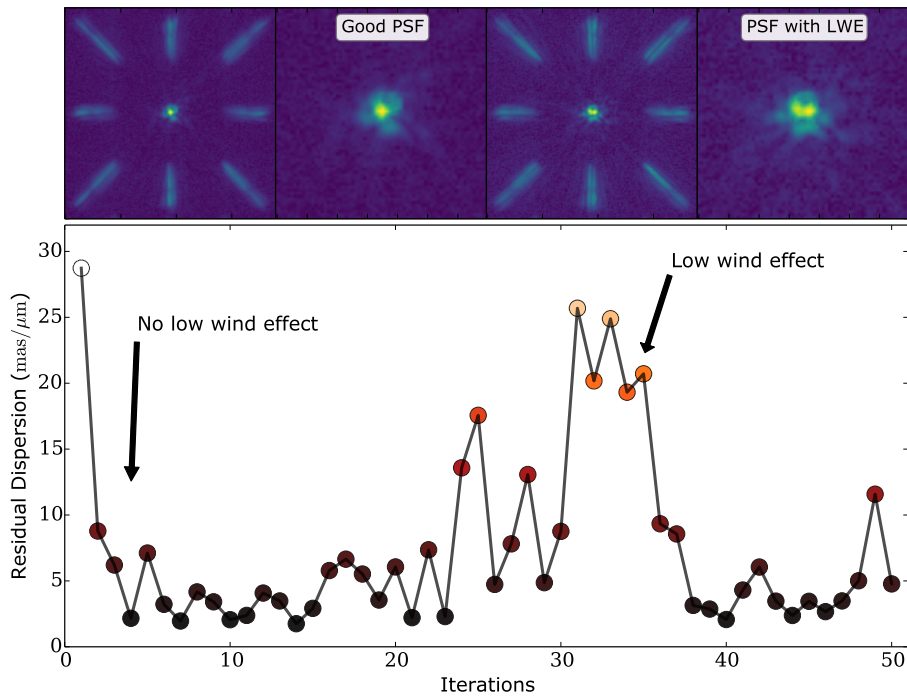
Figure 5.9: Closed-loop atmospheric dispersion correction in the presence of the low wind effect. In the presence of the LWE the PSF breaks up which affects the performance of the loop.

The results from the Fig. 5.8 show that the presence of instrumental dispersion can limit the final dispersion compensation and how varying atmospheric conditions can also have a large effect on the compensation. These aspects need to be taken into consideration when a high precision correction is required. The effect of low wind speed in the ground layer on the measurement accuracy of residual dispersion is discussed in the next section.

5.7   Effect of LWE on the PSF

The low-wind effect (LWE) is one of the newly discovered phenomena experienced by most high-contrast instruments including SCExAO. The LWE occurs in the presence of low wind speed ($\lesssim 1$ m/s at the ground layer) and it can significantly degrade the achievable PSF quality. The effect was firstly investigated by the SPHERE team (Sauvage et al., 2016). They concluded that, there is radiative cooling between the telescope spiders and the sky background, decreasing the temperature of the telescope spiders. This can create an optical path difference of up to 800 nm for a temperature difference of $1°$ between the air and the spiders over a spider height of 1 m (see Sauvage et al. (2016) for more details).

Here we show the impact of the LWE on the closed-loop performance of the dispersion correction. The effect was observed on the target λ Peg (spectral type G8, R-mag = 3.16, H-mag = 1.462) on the SCExAO engineering night of September 19th, 2016. For data collection and processing the same procedure was followed as explained in the subsection 5.4. The closed-loop test was performed with a loop gain of 50% and the result are shown in the Fig. 5.9. As can be seen from the figure, the loop had converged after 5 iterations and began to diverge around the 20th iteration before it

recovered by the 35th iteration. The divergence of the loop is associated with the breaking up of the PSF due to the LWE, which in turn affects the residual dispersion measurement. The inset of Fig. 5.9 shows a PSF with artificial speckles with and without the presence of the LWE, which deteriorated the PSF.

5.8 Noise terms limiting the measurement of dispersion

There are numerous elements that contribute to the accuracy with which the residual dispersion can be measured and subsequently corrected. Some terms limit the ability to measure the residual dispersion, while other dynamical terms limit the ability to correct the dispersion. Here we highlight some terms that should be considered for future implementations of this method.

The presence of strong wavefront aberration is one example of a limitation to the measurement accuracy. Telescope vibrations and the LWE (see Sec. 5.7) blur out the speckles, making it difficult to precisely locate the PSF core and the radiation center at times. From these two locales, the residual dispersion can be determined and hence if there are errors associated with estimating either, the residual dispersion measurement accuracy will be affected. The effect of the camera read noise on the measurement accuracy is discussed next.

5.8.1 Read noise

The internal NIR camera of the SCExAO has a readout noise of 114 e^- RMS. The readout noise for a NIR camera in ADU can be measured by,

$$\sigma_{image} = \frac{\sigma_{image1-image2}}{sqrt(2)}, \tag{5.2}$$

where σ_{image} is the standard deviation in a single image and $\sigma_{image1-image2}$ is the standard deviation in counts for difference of two images. Using the Eq. 5.8.1, the readout for internal NIR camera was measured to be 10 ADU. Using the readout noise in ADU, the gain for the camera will be 11.4. The analysis for the effect of read noise on an on-sky data was carried out by introducing additional read noise (ADU). A single on-sky image was used and read noise was added then measurement of the dispersion was carried out. The variance in measurement was calculated by repeating the process for each introduced read noise. The result of such an analysis is presented in Fig. 5.10. The figure represents the variance in the measurement of the dispersion as a function of read noise in ADU. The conclusion from the analysis is that read noise of the camera affects the measurement of the dispersion, which is at 2 $mas/\mu m$ and the on-sky measured value is in the same range see Fig. 5.6. The next section discusses the effect the photon noise.

5.8.2 Photon noise

The effect of photon noise on the measurement was carried out by using an on-sky image. The image was dark subtracted and hot pixels removed. Then using the gain calculated from the previous section, pixel counts in ADU were converted to photo-electrons. The number of photo-electrons was varied to see its effect on the measurement. The result of such an analysis is presented in Fig. 5.11. The figure shows variance in the measurement of the dispersion as a function of 1/number photons. The estimated number of photons in the on-sky image is also shown in the figure. The effect of photon noise on the measurement is very small compared to the that of read noise.
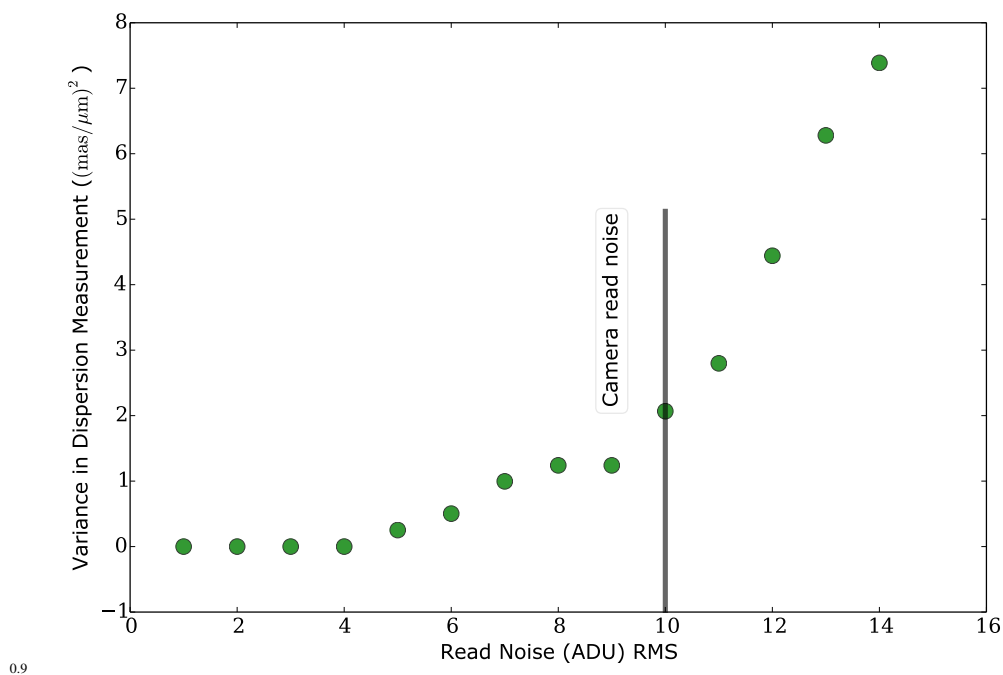
Figure 5.10: Variance in the measurement of the dispersion as a function read noise in ADU.
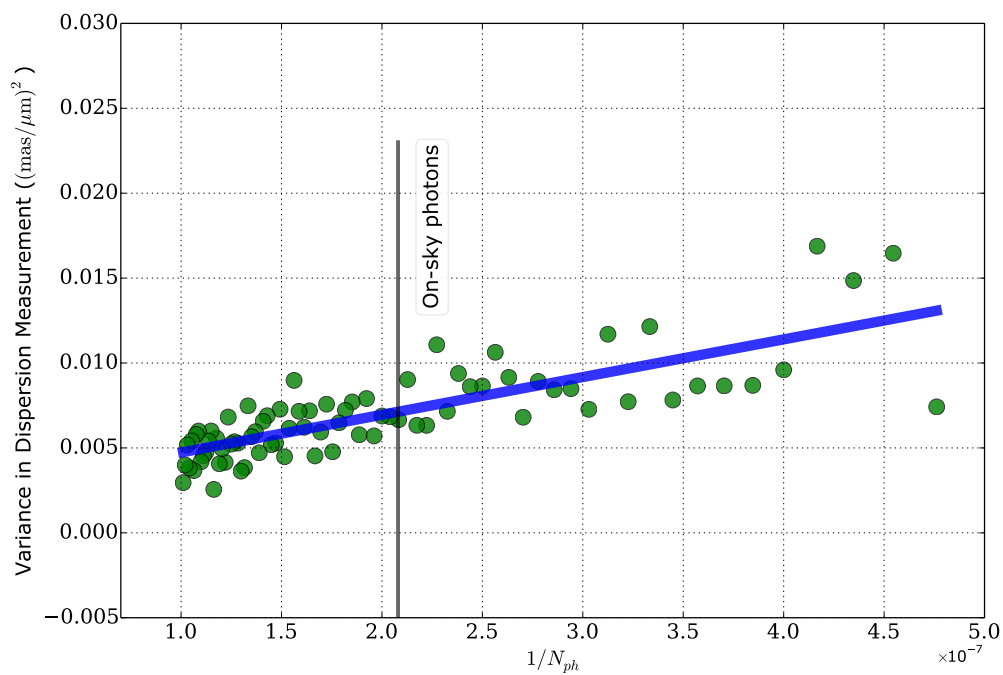
Figure 5.11: Variance in the measurement of the dispersion as a function of photon noise.

5.9   Averaging of the on-sky data

As discussed previously, I have shown that photon noise does not affect the measurement accuracy of the dispersion. In this section, I discuss the improvement in accuracy by averaging the measurements. For this analysis, I used the same data set as presented in the Fig. 5.6, which shows 1000 measurements of the residual dispersion before and after closing the loop. I binned the 1000 data points in 100 bins, each bin contains 10 measurements. Next, I took the average in each bin and result of such analysis is shown in Fig. 5.12. The open loop measurements are shown in green and 10 measurements average by blue, and closed-loop measurement in red (without average) and cyan (with average). It can be concluded from the figure, the accuracy goes up by averaging the measurements. As discussed previously read noise of the camera is the major limitation to the accuracy of measurement, the other possible noise term includes dispersion due to til/tilt, which is discussed next.

5.9.1   Dispersion due to atmospheric tip/tilt

Thus far we have only addressed the static component of the atmospheric dispersion, however, another important limitation to the measurement accuracy comes from the chromatic component of atmospheric tip-tilt, which results in a dynamic variation in the dispersion. The atmospheric dispersion creates a small tip/tilt in the science path assuming a perfect correction of tip/tilt in WFS path (if not LOWFS can sense and correct by driving the DM for this aberration). The atmospheric dispersion also creates a dynamic tip/tilt dispersion in the science band, which is due to variation of the refractivity across the science band. The amplitude of dispersion due to atmospheric tip-tilt can be estimated based on seeing measurements. Assuming a Kolmogorov profile for the turbulence, the atmospheric tip-tilt RMS amplitude is $\approx 93\%$ of the total seeing. Since the median seeing for Maunakea is 0.66 arcsec RMS, the tip-tilt from atmospheric turbulence is 0.61 arcsec RMS. From a model of the refractive index of the atmosphere, the change in the refractivity of air is about 2% from the visible (500 nm) to the NIR (1500 nm) and 0.077% across H-band ($1.5 - 1.8$ μm) alone (Ciddor, 1996). Assuming a perfect tip-tilt correction at the wavefront sensing wavelength, the variation in refractivity will create a differential tip-tilt at the observing wavelength. The amplitude of the resulting dynamic dispersion is given by the variation of refractivity across the observing band multiplied by atmospheric tip-tilt at the sensing wavelength. On Maunakea, the H-band dynamic dispersion due to atmospheric tip-tilt will then be $0.61'' \times 0.00077 = 0.47$ mas RMS and 3.14 mas in y-H band. And this is what we see from our measurement, as shown in Fig. 5.6.

As current ADCs are slow and not designed to correct for fast variations like this, these variations are currently not addressed. However, by observing for much longer than the atmospheric coherence time (several seconds) this effect can be greatly reduced as the mean dispersion, which is the static component, can be well corrected as demonstrated in this body of work. It is important to consider the cadence and exposure time of acquisition images used to measure the residual dispersion to ensure that the dynamic component does not affect the measurement of the atmospheric dispersion.

For ELTs, the diffraction limited PSF will be ~ 6–8 mas at 1 μm. As explained in Devaney et al. (2008), a tip-tilt error of 1 mas RMS will reduce the Strehl ratio by a factor of 0.82. This limitation can be overcome by performing faster measurements and corrections, which are at present limited by the rotational speed of ADC prisms. An error budget study of the temporal variation of dispersion due to atmospheric tip-tilt needs to be carried out for future ADC designs to address the dynamic component of the dispersion.
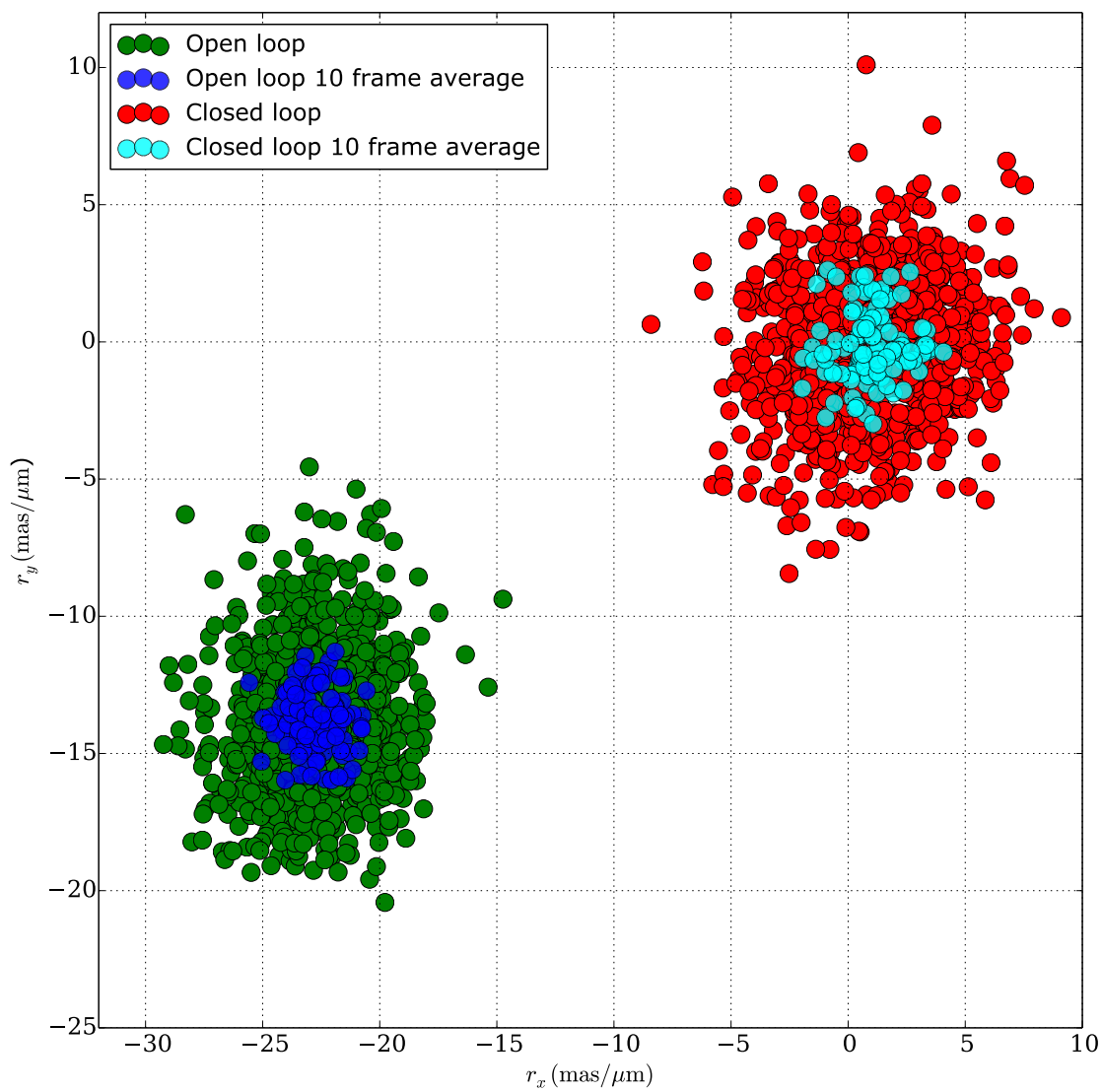
Figure 5.12: Scatter plot showing the effect binning and averaging for the on-sky measurement of the dispersion.

5.10 Summary

In this chapter, I demonstrate the measurement of the residual dispersion in the final science image for the first time, using the concept illustrated in the previous chapter. The measured residual dispersion was corrected by driving the prisms of ADC in a single step. The concept behind the measurement and correction of the dispersion and its on-sky demonstration was published in Pathak et al. (2016). After on-sky verification of the technique, the algorithm for closed-loop correction of the dispersion was developed, which resulted in a better correction than a single step one.

Measurements of the residual dispersion post look-up table based correction of the ADC was carried out for various telescope elevations. These measurements helped me answer key operation and optimization questions, including:

- how residual dispersion varies as a function of elevation?

- how frequently dispersion needs to be corrected?

- Sources of dispersion in the final science image?

- An important result of this analysis was showing the presence dispersion due to internal optics.

The presence of dispersion due to internal optics can be attributed to few refractive components inside the SCExAO, including AO188 beam splitter but it's difficult to pinpoint to a particular optic.

I also showed that even after accounting for the dispersion due to internal optics, there was still some residual dispersion left. As AO188/ADC employs correction based on a look-up table and calculation of this table utilizes constant atmospheric parameter. So the presence dispersion even after accounting for internal optics can be attributed to the varying atmospheric conditions, and its effect was more dominant for lower telescope elevations.

The results of closed-loop correction of the dispersion and performance analysis of look-up table based correction of the dispersion by AO188/ADC will soon be submitted for the publication. In the next chapter, I present the impact of the closed-loop correction of the dispersion for high-performance coronagraphy, which is the main science goal of this thesis.

Science: High-performance Coronagraphy

Direct imaging of exoplanets requires high-angular resolution (100 mas for an exoplanet separated by 1 AU at a distance of 10 pc), and contrast which varies from 10^{-3} for young hot giants to 10^{-10} for Earth-like planets. To image exoplanets close to the host star, high-performance coronagraphs (small IWA) needs to be employed. As mentioned in Chapter 1, small IWA coronagraphs are very sensitive to low-order aberrations (tip-tilt, focus, astigmatism, and coma) and bandwidth (chromaticity). Coronagraphic LOWFS are employed by HCI instruments for correcting low-order aberrations. The atmospheric dispersion in the science path due to uncorrected tip/tilt at wavefront sensing can be measured by LOWFS and corrected using the DM. However, as explained in Section 5.9.1, the atmospheric dispersion can have static and dynamic component (due to the variation of refractivity within the band), which cannot be measured by LOWFS or corrected using the DM, thus the presence of residual dispersion results in a leakage while employing small IWA coronagraphs. In this chapter, I discuss the leakage of light due to the presence of the dispersion and improvement in contrast by correcting the dispersion, using the techniques discussed in the previous chapter.

SCExAO employs three high-performance coronagraphs, which are PIAA, vortex and 8OPM with their IWA being $1.5\lambda/D$, $1\lambda/D$ and $1\lambda/D$ respectively. To study the effects of residual dispersion on contrast performance, I will focus on the vortex coronagraph, because it is the main coronagraph used for science observations with SCExAO, and is therefore the one best characterized.

6.1 Simulation of coronagraphs

Before going into the details of simulating the vortex coronagraph, I will first describe the simulation of a simple classical Lyot coronagraph. The majority of coronagraphs can then be simulated using the same formalism, just by varying the design of the focal plane mask.

6.1.1 Lyot-type coronagraphs

In this section, a general formalism of Lyot-type coronagraphs is presented. A general optical layout of a coronagraph system is shown in Fig. 6.1. The setup consists of four successive coronagraphic planes A, B, C and D as shown in Fig. 6.1. Plane A is the entrance pupil plane (apodized in case PIAA). Plane B is the focal plane with the hard-edged occulting mask in the case of Lyot-coronagraph and phase-mask in the case of vortex or 8OPM. Plane C is a Lyot stop, generally a $5-10\%$ undersized version of the entrance pupil plane. The purpose of the Lyot stop is to stop the residual diffracted starlight outside the edges of the pupil from destroying the contrast. Plane D is the final coronagraphic image plane.
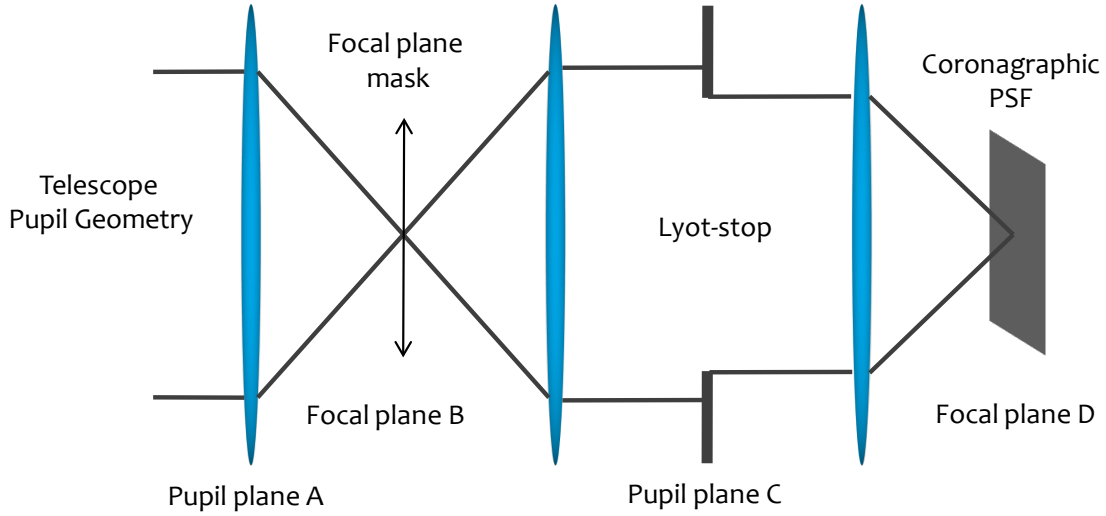
Figure 6.1: Optical layout of a coronagraph system. Four coronagraphic planes: A; pupil plane. B; focal plane mask (hard-edged occulting or phase mask), C; Lyot stop (possibly undersized) and D; image plane.

To describe the effects of propagation between the pupil and focal planes, usual paraxial optics and Fraunhofer approximations (perfect lenses) are considered, so that a FT relationship exists between two successive planes. FT ($\Im$) is used to propagate complex amplitude fields from the pupil plane to the focal plane and the inverse FT ($\Im^{-1}$) from focal to the pupil plane. The equations described below will be applicable to any type of coronagraphs, the variable terms can be the pupil function (apodization) and the focal plane mask (depending on the coronagraph used). The notations used follow Soummer et al. (2007b).

The telescope aperture function with the position vector $r = (x, y)$ can be written as $P(r)$, the apodization function is denoted by $\phi(r)$. The field amplitude ψ_A at telescope pupil plane A is given by,

$$\psi_A(r) = P(r)\phi(r). \tag{6.1}$$

A mask of transmission function described by $1 - M(r)$ is placed at the plane B, where M is the index function that describes the mask shape $M = 1$ inside the mask and 0 outside for classical hard-edged Lyot-coronagraph. The field amplitude ψ_B at the plane B is given by taking a FT of $\Im(\psi_A)$ (complex amplitude) and multiplying by the mask function,

$$\psi_B(r) = \widehat{\psi_A}(r)(1 - M(r)). \tag{6.2}$$

In the equations above and below $\widehat{}$ denotes the FT. The Lyot stop is an undersized function of the pupil plane A, here noted by $L(r)$. The field amplitude ψ_C at the plane C is given by taking an inverse FT of $\Im(\psi_B)$ and multiplying by the Lyot stop,

$$\psi_C(r) = (\psi_A(r) - \psi_A(r) \star \widehat{M}(r))L(r), \tag{6.3}$$

where $\star$ is the convolution product. The field amplitude ψ_D at the plane D is given by taking a FT of $\mathfrak{I}(\psi_C)$

$$\psi_D(r) = (\widehat{\psi_A}(r) - \widehat{\psi_A}(r)M(r)) \star \widehat{L}(r). \tag{6.4}$$

The final intensity on the image plane is given by $I = |\psi_D(r)|^2$. The next section shows a numerical simulation of the Lyot coronagraph for the Subaru Telescope.

Lyot coronagraph simulation for the Subaru Telescope

Numerical simulation of the Lyot coronagraph for H-band ($1.5 - 1.8 \ \mu$m) follows the same steps as discussed in Chapter 3 for the simulation of the PSF and the atmospheric dispersion. For simulating a coronagraphic PSF, it is important to use sufficient sampling in the plane A, to get the features of telescope secondary mirror and its support structures. In plane B, to get a sufficient sampling across the focal plane mask, a padding factor more than $\gamma > 6$ in plane A is usually desired, which translates to more than 6 pixels per resolution element in plane B (for a mask of 5λ/D size, it will have 30 pixels). Figure 6.2 shows a numerical simulation of the classical Lyot coronagraph. Here the sampling across the pupil is kept at $Na = 500$ and with a padding of $\gamma = 6$. The total sampling (pixels) in the focal plane is then 3000 pixels. The plate scale for the simulation is 5 mas/pix. In Fig. 6.2, plane A shows the Subaru telescope pupil plane geometry, plane B shows the PSF after propagating through the focal plane mask. The size of the focal plane mask is $5\lambda/D$ in diameter. Plane C shows the exiting pupil after Lyot stop, leakage of light into the pupil can be clearly seen from the figure. Plane D shows the final coronagraphic PSF, diffraction features (Airy rings) from hard edged mask can be clearly seen. Lyot coronagraphs are limited in IWA to $5\lambda/D$, if the focal plane size is $< 5\lambda/D$ there is more leakage of light in plane C. The contrast and IWA achieved by classical Lyot coronagraph is inferior compared to current generation of stellar coronagraphs like apodized Lyot coronagraph, vortex, FQPM, 8OPM.

   After establishing the formalism for the simulation of the classical Lyot coronagraph, the next section will briefly discuss the theory behind VVC coronagraph and then will present numerical simulations.

6.1.2   Vector vortex coronagraph

The Vector Vortex Coronagraph (VVC) is a phase-masked coronagraph, one of the most efficient in terms of IWA and throughput. The working principle behind VVC is a continuous helical phase ramp in the focal plane with a phase singularity in its center. Upon propagation from the focal plane B to pupil plane C, azimuthal phase ramp sends the light outside the original pupil area, where it can be stopped by a Lyot stop. VVC is sensitive to the central obscuration, telescope support structures (spiders), low-order aberrations (tip-tilt, focus, etc) and bandwidth (chromaticity) (Mawet et al., 2009) . Here I simulate the effects of tip-tilt and atmospheric dispersion on a vortex coronagraph. For detailed theory of the VCC please see Mawet et al. (2005)

   The simulation of the VVC is based on the Lyot coronagraph simulation, except for a different focal plane mask. The focal plane mask of an optical vortex, which only affects the phase of the PSF and not the amplitude, is generated by the complex amplitude transmission mask of the form $e^{i\theta}$, with θ being the azimuthal coordinate. Optical vortex coronagraphs are characterized by their topological charge l, meaning that, upon a complete rotation about the center, it has undergone a
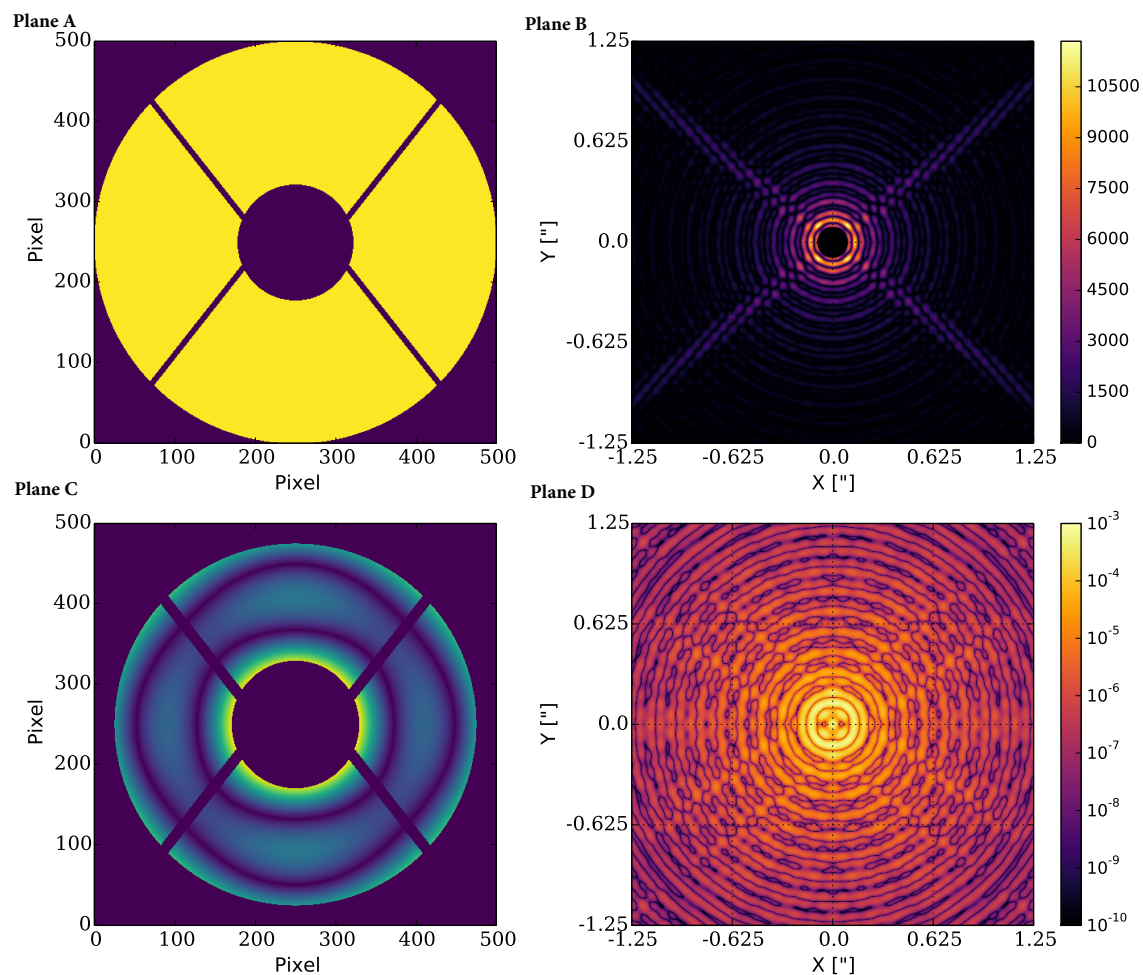
Figure 6.2: Numerical simulation of Lyot coronagraph for the Subaru telescope in H-band. Propagation through each coronagraphic plane is shown. Plane A, Subaru telescope pupil plane geometry, plane B, focal plane mask on top of the PSF, plane C, exiting pupil and plane D shows final coronagraphic PSF.

total of $l \times 2\pi$ phase shift. The phase function of a vortex coronagraph is given by,

$$\psi_A(r) = P(r) \times \exp(jkl\theta), \tag{6.5}$$

where k is the wavenumber and l is the topological charge. To simulate the VVC used by SCExAO, I used an optical vortex of topological charge 2, which has a small IWA compared to charge 4 and 6. But charge 4 and 6 are less sensitive to low-order aberrations. The numerical simulation of a vortex coronagraph for H-band ($1.5 - 1.8\ \mu$m) of charge 2 is shown in the Fig. 6.3. The figure shows different coronagraphic planes. Plane B shows the phase only, which shows the phase modulation around the center, plane C, shows the Lyot-stop and leakage around secondary obstruction can be seen. Plane D shows the coronagraphic PSF in the focal plane and the colorbar represents the contrast normalized to the PSF without coronagraph. Next, the effect of low-order aberration on the performance of coronagraph is discussed.
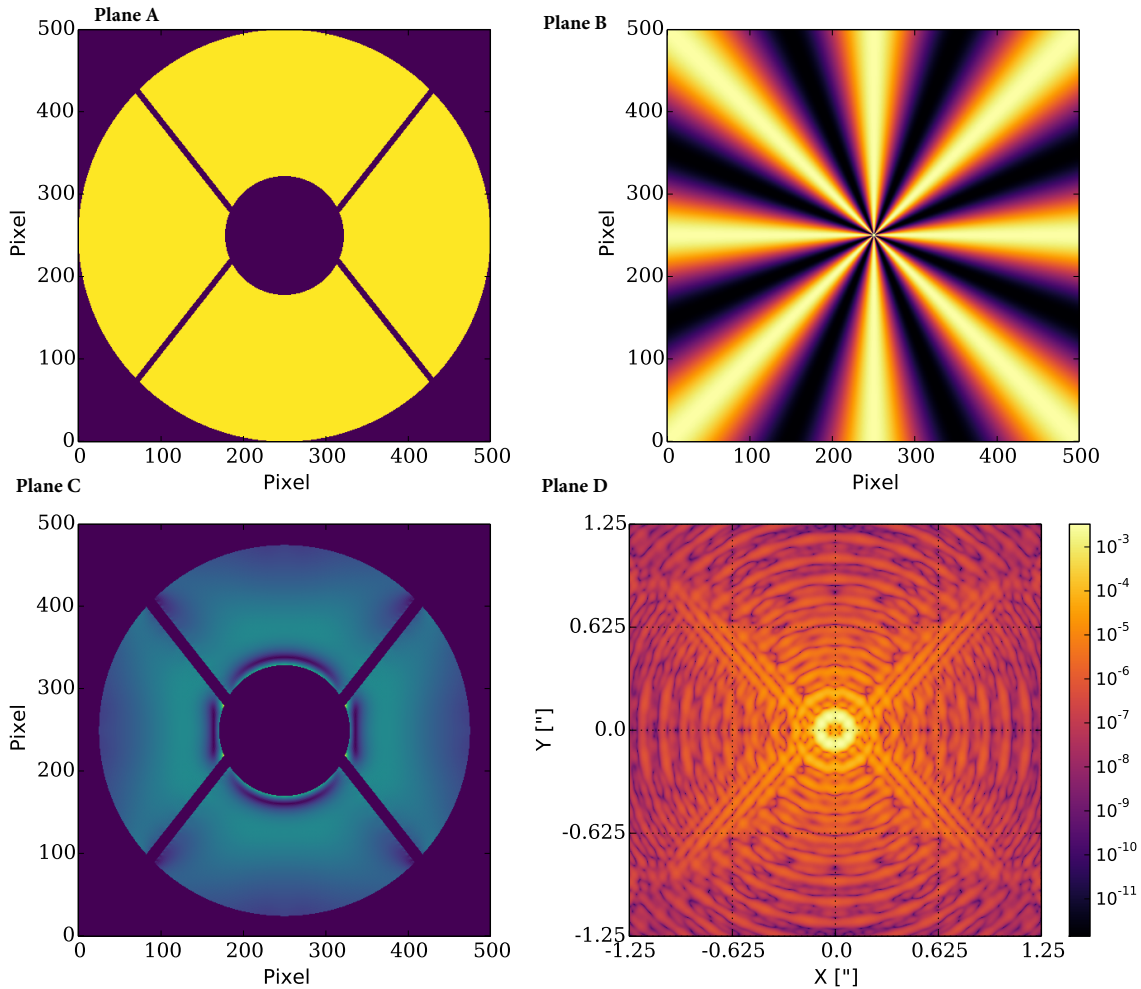
Figure 6.3: Numerical simulation of the vortex coronagraph of charge 2 for Subaru Telescope pupil geometry. Plane A, Subaru telescope pupil geometry, plane B, showing the phase modulation in the focal plane mask, plane C, Lyot stop, and plane D vortex PSF.

6.2 Effect of low-order aberrations on a vortex coronagraphic

To test the effect of low-order aberrations such as tip/tilt and the atmospheric dispersion a high-performance coronagraph such as vortex was chosen. I used the previously simulated vortex coronagraph to test the leakage of light as a function of tip-tilt and the atmospheric dispersion. The result of simulation for a vortex throughput as a function of angular separation applied using the tip in mas is shown in Fig. 6.4. The figure can be interpreted as a leakage of light as a function tip in mas, the inset shows 5% leakage of light for 10 mas of a tip. For example if a VVC is achieving a 10^{-4} contrast at $2\lambda/D$ a 5% leakage will reduce the contrast to $\approx 5 \times 10^{-2}$. Simulation for the VVC throughput as a function of dispersion in mas is shown in Fig. 6.5. The effect of dispersion on VVC is hard to quantify because manufactured VVC suffer from chromaticity (for simulations I assumed an ideal VVC), so the effect of dispersion will be even worse than the results presented here.

6.3 Lab characterization of vortex coronagraph

The lab performance of the vortex coronagraph deployed on SCExAO was carried out to test the flux leakage for low-order aberration. The current hardware of SCExAO is not equipped to simulate the effects of the atmospheric dispersion, so only tip/tilt aberration was tested. The tip was applied using the internal calibration source of the SCExAO. The output of the internal source is mounted on a translation stage, which enables a sub-milliarcsecond precision translation. Figure 6.6 (a) shows a vortex PSF for an aligned coronagraph and (b) for a misaligned coronagraph by applying a tip of 40 mas. The figure shows a better flux suppression for an aligned coronagraph, and for misaligned coronagraph, the leakage of light and diffraction from Lyot stop can be clearly seen. Images were taken using the internal NIR camera inside the SCExAO. The figure shows an average of 100 dark-subtracted frames. The exposure time for each frame was 50 μsec.

Figure 6.9 shows a throughput curve for a vortex coronagraph as a function of angular separation in mas. The tip was applied from 0 mas to 350 mas to an aligned coronagraph. The flux was calculated inside the white circle shown in Fig. 6.6, the radius of the circle is $0.835''$. The counts from all the pixels were summed inside the white circle. The inset of Fig. 6.9 shows the leakage of light for small angular separation. The experimental result presented here is similar to the result obtained from simulation (see Fig. 6.4). A small variation can be noticed, which was due to slightly different designs between simulated Lyot stop and the experimental one. This figure shows the sensitivity of the coronagraph to a low-order aberration such as tip/tilt, which can also be attributed to the atmospheric dispersion. The next section presents the on-sky results for coronagraphic measurements.

6.4 On-sky results

In this section, I present the effect of residual dispersion on the performance of VVC. The presence of residual dispersion becomes a dominant noise source for small IWA coronagraphs once the other WFE have been accounted for. To test the impact of the closed-loop correction of the dispersion on the performance of small IWA coronagraphs, a high Strehl ratio (preferably $> 90\%$) and a fine correction of coronagraphic low-order modes are required. At the time of the test due to limitations in the SCExAO control software, PyWFS and LLOWFS could not be employed simultaneously
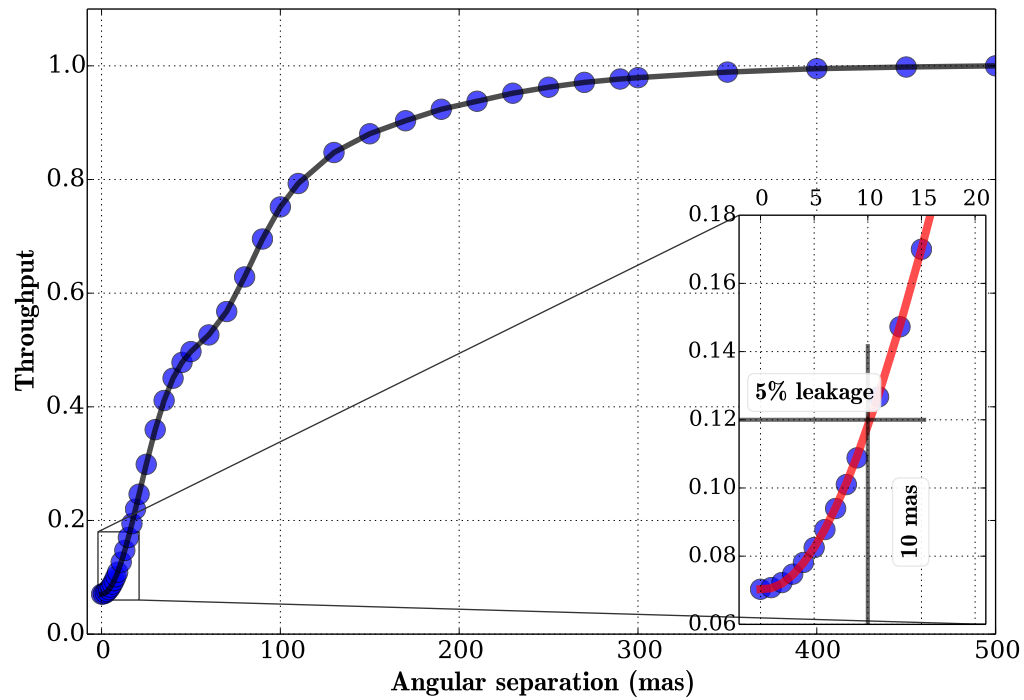
Figure 6.4: Throughput for a simulated vortex coronagraph as a function of angular separation (mas). the zoomed inset shows throughput measurement for small angular separation.
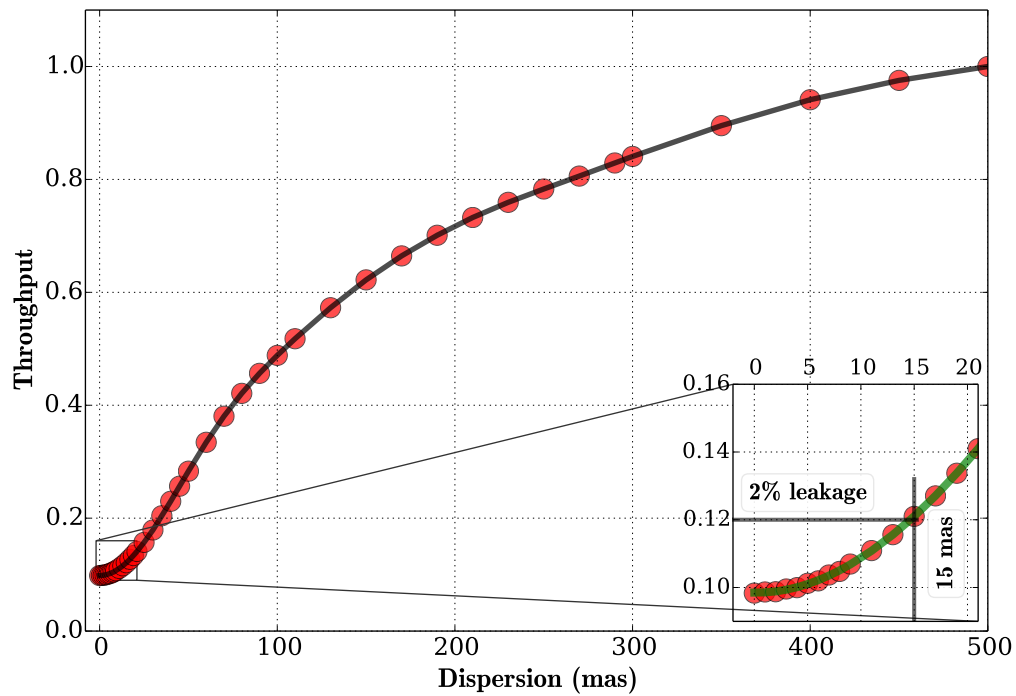
Figure 6.5: Leakage of light through a simulated vortex coronagraph throughput as a function of dispersion. The zoomed inset shows throughput measurement for small dispersion.
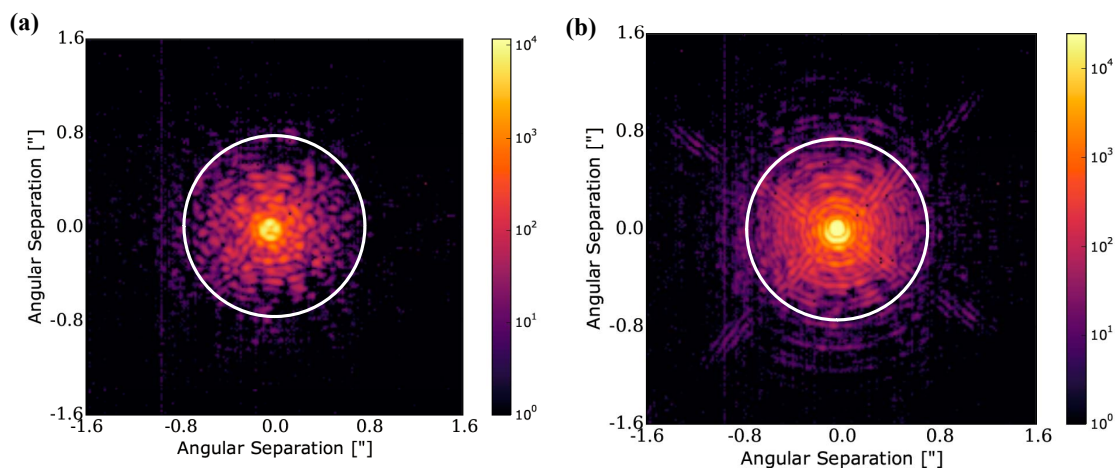
Figure 6.6: Lab image (taken using internal NIR camera) showing leakage around the vortex PSF. (a) Aligned vortex coronagraph (b) misaligned vortex coronagraph with 40 mas of tip in *y*-direction, the white circle shows area were flux was summed for throughput measurement.
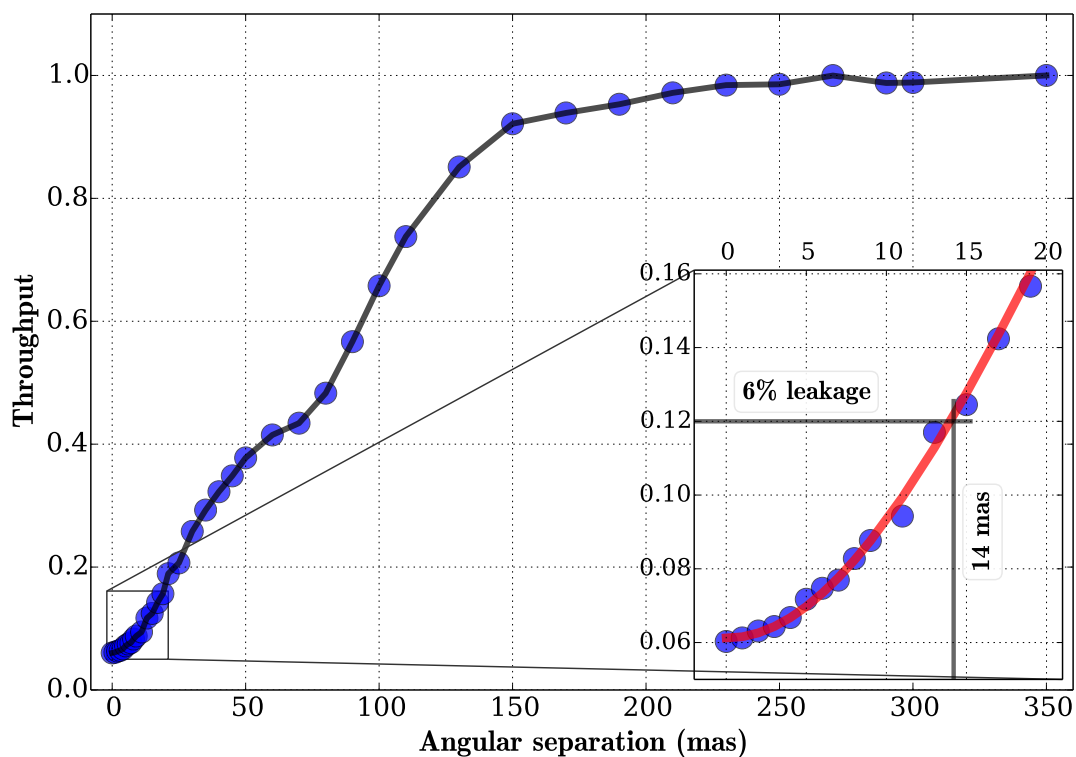
Figure 6.7: Vortex coronagraph throughput as a function of angular separation. The zoomed inset shows throughput measurement for small angular separation.

while using the satellite speckles for the dispersion measurement. To overcome this limitation, the following strategy was used:

1. The coronagraph flux leakage test was performed within a 10-minute window and it is assumed that the static atmospheric dispersion did not change considerably within that window, based on the results from Chapter 5.

2. Next, I closed the correction loop on the on-sky dispersion (including dispersion from the atmosphere and internal-optics) using the method explained in chapter 5. Then the loop was paused and satellite speckles were removed.

3. The PyWFS loop was closed to provide high Strehl ratio.

4. The LLOWFS loop was closed with vortex coronagraph to provide a fine correction of tip/tilt, focus, and astigmatisms.

5. Coronagraphic data were collected using the static correction of the on-sky dispersion.

6. Prism offsets used by closed-loop correction of the dispersion were removed. The ADC was reverted back to the look-up table based correction.

7. Coronagraphic data were collected again for look-up table based correction of the dispersion.

Using the steps explained above, the on-sky data was collected on the target W Hya (spectral type M7, V-mag= 7.70, H-mag= -2.56) on SCExAO's engineering night of March 13th, 2017. The telescope elevation during the data collection was $41°$. The result of this on-sky experiment is shown in Fig. 6.8. The data shown in the figure represents an average of 1000 co-added frames. Figure 6.8 (a) shows an on-sky vortex PSF with the look-up table based ADC correction and Fig. 6.8 (b) with closed-loop ADC correction. From the figure it can be seen that diffraction features from spiders are present in Fig. 6.8 (a) compared to that of Fig. 6.8 (b), which clearly shows the leakage of light due to residual dispersion (similar to lab measurements, see Fig. 6.6).

The raw contrast curve (with no post-processing) for the VVC PSF as shown in Fig. 6.8 was calculated by dividing maximum of the flux from a PSF without coronagraph. The raw contrast curve shown in Fig. 6.9 was generated by taking a radial average from the center of the VVC PSF (see Fig. 6.8). The comparison between the raw contrast curve for look-up table based and closed-loop correction of the dispersion is shown in Fig. 6.9. The figure shows an improvement in the raw contrast at small separations < 100 *mas*, where the starlight leakages are the strongest for a closed-loop correction of the on-sky dispersion compared to a look-up table based correction of the ADC. The improvement was marginal because we are dominated by low-order aberrations, especially tip/tilt variations.

6.4.1 Summary

In this chapter, I demonstrate using on-sky measurements, that closed-loop atmospheric dispersion compensation yields in an improved coronagraphic contrast compared to the conventional look-up table based correction of dispersion. The vortex coronagraph used on-sky testing has an IWA of $1.5\lambda/D$. The effect of dispersion will be even worse for $1\lambda/D$ IWA coronagraphs.

During my measurement, the image quality is dominated by residual WF errors (providing a Strehl ratio of $60-80\%$ in H-band), poor low-order correction and telescope vibration. However, I
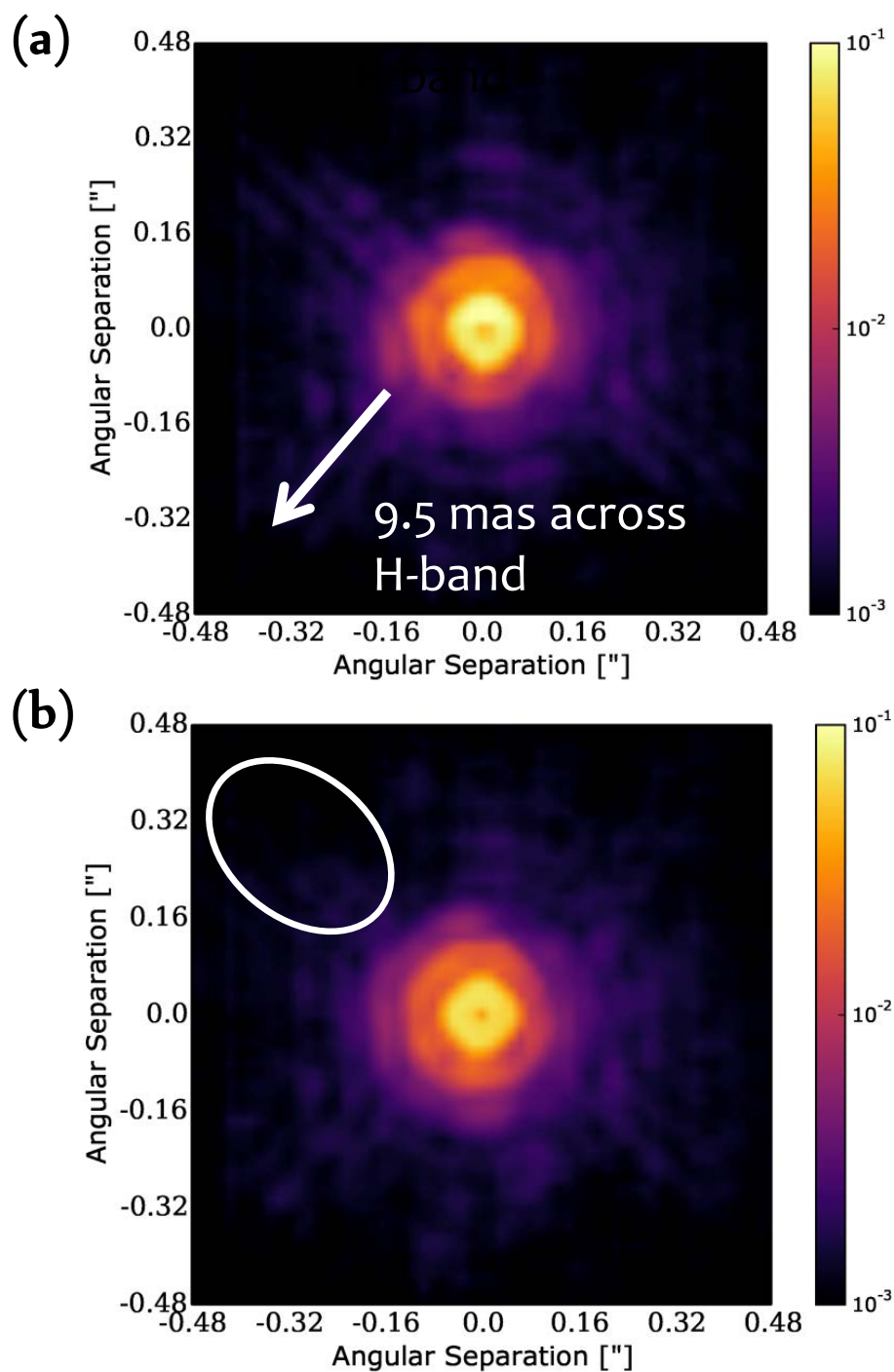
Figure 6.8: On-sky vortex coronagraph PSF (1000 frame average). Wavefront correction using PyWFS and LLOWFS was applied. (a) With look-up table based ADC correction. (b) With closed-loop ADC correction.
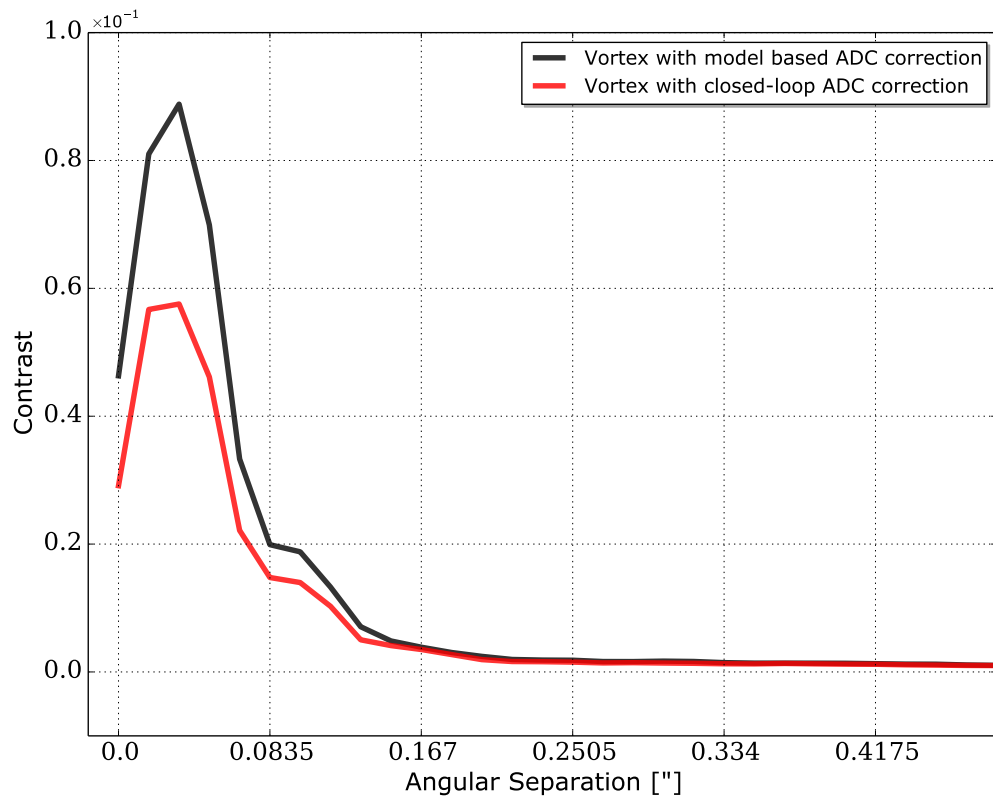
Figure 6.9: Vortex coronagraph contrast curve as a function of angular separation for closed-loop and model-based ADC correction.

was still able to show the effect of residual dispersion on the performance of vortex coronagraph. The residual dispersion will be a dominant source of noise once the other noise terms have been addressed. So the work presented in this thesis will help mitigate the effects of residual dispersion yielding in a better contrast for small IWA coronagraphs.

CHAPTER 7

Summary and Future Work

Atmospheric dispersion is a chromatic error due to the presence of Earth's atmosphere and until now there was no method to measure its presence in the final science image. In this work, I have demonstrated a new focal plane based technique to measure residual dispersion in the final science image. My approach offers a way to measure residual dispersion to a high-precision and apply a correction by a fine control of the ADC, as an offset to the look-up table based correction presently used. The technique was validated on-sky and can also be used to drive an ADC correction in a closed loop. In closed-loop, we managed to achieve < 1 mas of elongation in the PSF across H-band. We observed that the residual dispersion (static component) does not change significantly as a function of time or elevation, therefore very small corrections at low cadence are needed to implement a high level of correction. This work addresses the issue of imperfect compensation by the ADC and dispersion resulting from internal optics. The presence of dispersion due to internal optics can significantly offset the correction by an ADC, even when the theoretical look-up table utilized for compensation is accurate. This is expected as the model is not aware of any instrumental biases.

The measurement of dispersion uses internal NIR camera inside the SCExAO, it runs at a speed of 170 Hz. Currently, the measurement of dispersion is limited by read noise of the camera. The high-speed measurement makes it possible to identify both static and dynamic component of the atmospheric dispersion. This capability can be employed to design advance ADCs to correct dispersion due to atmospheric tip/tilt in a closed-loop manner, which is currently limited by the hardware design of the ADC.

Finally, I show the impact of residual dispersion on a $1.5\lambda/D$ IWA vortex coronagraph. By correcting the dispersion in closed-loop there was an improvement in the contrast compared to look-up table based correction. The effect of residual dispersion will be even worse for $1\lambda/D$ IWA coronagraphs. The residual dispersion will be the dominant source of noise once the other noise terms have been addressed. The test needs to carried out for other small IWA coronagraphs such as 8OPM and PIAA. Closed-loop atmospheric dispersion correction will become increasingly important as SCExAO's contrast improves thanks to the further development of its coronagraph and wavefront control subsystems.

At present, the measurement algorithm relies on very broadband light (y to H-band), in order to improve the measurement accuracy. Since most high-contrast coronagraphic observations are performed over a single band at a time, the algorithm would need to be adapted to work with J, H or K band, based on observation requirement. The impact of reducing the bandwidth on the accuracy of extracting the residual dispersion would need to be carefully investigated. However, if MKIDS or an IFS such as CHARIS could be used, it would allow for a very accurate extraction

of the satellite speckles as a function of wavelength to enable precise measurement of the residual dispersion. This would be one avenue to reducing the slow-varying (static) component atmospheric dispersion even further. Another possible avenue of investigation will be to use MKIDs real-time fast measurement of dispersion to estimate the associated coronagraphic leaks and remove it from the data in post-processing. This measurement will allow for a better calibration and reduction of science images for high-contrast science.

An important limitation throughout this work was that the ExAO performance of SCExAO could not be used while the calibration speckles were used for the measurement of dispersion. Recently this limitation has been overcome by employing a better software architecture for wavefront control. By addressing the deployment of calibration speckles while the ExAO loop is running, the work in thesis will soon be integrated for science observations, which will improve the performance of IWA coronagraphs. As ExAO loop of SCExAO and AO loop of AO188 are limited to 8 magnitude star for wavefront sensing. The measurement of dispersion can use a more sensitive camera such as CHARIS or SAPHIRA compared to currently used internal NIR camera throughout this work. Another limitation to the correction of dispersion was slow rotation speed of ADC prisms, which can be addressed by using a faster protocol to apply offsets from SCExAO's to AO188 computer than currently used SSH protocol (which is slow). At present, the ADC prisms apply offsets one at a time, which can be addressed by using a better software control.

This work can also be used as a diagnostic tool to measure the dispersion due to internal optics in the final science image and it can also be used to test and calibrate the look-up table based correction of ADCs. I presented the first-hand calculation of dispersion due to atmospheric tip/tilt for the Maunakea site for median seeing in H-band, $\approx 0.5''$. The dynamic component of the atmospheric dispersion sets a limit on the precision of a look-up table can achieve, even by testing and calibrating its correction. The effect of the dynamic component will be even worse for poor seeing conditions.

For AO systems operating on ELTs, chromatic effects will be a dominant source of error, which will require a closed-loop correction of dispersion. I propose the following concept to achieve a closed-loop correction of dispersion on ELTs,

- Using a dedicated band for high-speed sensing of the dispersion. Depending on the science band used (y-J or H) for observation, an alternative band can be used for measurement.

- Current measurement algorithm needs to be adapted to work in y-J or H-band.

- Dispersion being linear in IR can be interpolated in science band to correct for it.

- Calibration speckles for the measurement can be generated using a transmission grating.

An error budget study of the temporal variation of dispersion due to atmospheric tip-tilt needs to be carried out for future ADC designs to address the dynamic component of the dispersion. At present the read noise of internal NIR camera affects the dispersion measurements, this makes the measurement of the dynamic component of dispersion unreliable. In future SAPHIRA camera (currently undergoing on-sky testing) can be used to study the temporal variation of the dynamic component of the dispersion.

So the work presented in this thesis will help to achieve a better contrast for small IWA coronagraphs, pushing the limits of achievable contrast from ground-based HCI instruments. In the era of ELTs, sub-milliarcsecond correction of dispersion will be required to image and perform high-precision astrometric measurements of terrestrial exoplanets.

Bibliography

C. W. Allen. *Astrophysical quantities*. 1973.

D. Atkinson, D. Hall, C. Baranec, I. Baker, S. Jacobson, and R. Riddle. Observatory deployment and characterization of SAPHIRA HgCdTe APD arrays. In *High Energy, Optical, and Infrared Detectors for Astronomy VI*, volume 9154 of *Proc. SPIE*, page 915419, July 2014. doi: 10.1117/ 12.2056807.

L. H. Auer and E. M. Standish. Astronomical Refraction: Computational Method for All Zenith Angles. *AJ*, 119:2472–2474, May 2000. doi: 10.1086/301325.

G. Bakos, R. W. Noyes, G. Kovács, K. Z. Stanek, D. D. Sasselov, and I. Domsa. Wide-Field Millimagnitude Photometry with the HAT: A Tool for Extrasolar Planet Detection. *PASP*, 116: 266–277, Mar. 2004. doi: 10.1086/382735.

J.-L. Beuzit, M. Feldt, K. Dohlen, D. Mouillet, P. Puget, F. Wildi, L. Abe, J. Antichi, A. Baruffolo, P. Baudoz, A. Boccaletti, M. Carbillet, J. Charton, R. Claudi, M. Downing, C. Fabron, P. Feautrier, E. Fedrigo, T. Fusco, J.-L. Gach, R. Gratton, T. Henning, N. Hubin, F. Joos, M. Kasper, M. Langlois, R. Lenzen, C. Moutou, A. Pavlov, C. Petit, J. Pragt, P. Rabou, F. Rigal, R. Roelfsema, G. Rousset, M. Saisse, H.-M. Schmid, E. Stadler, C. Thalmann, M. Turatto, S. Udry, F. Vakili, and R. Waters. SPHERE: a 'Planet Finder' instrument for the VLT. In *Ground-based and Airborne Instrumentation for Astronomy II*, volume 7014 of *Proc. SPIE*, page 701418, July 2008a. doi: 10.1117/12.790120.

J.-L. Beuzit, M. Feldt, K. Dohlen, D. Mouillet, P. Puget, F. Wildi, L. Abe, J. Antichi, A. Baruffolo, P. Baudoz, A. Boccaletti, M. Carbillet, J. Charton, R. Claudi, M. Downing, C. Fabron, P. Feautrier, E. Fedrigo, T. Fusco, J.-L. Gach, R. Gratton, T. Henning, N. Hubin, F. Joos, M. Kasper, M. Langlois, R. Lenzen, C. Moutou, A. Pavlov, C. Petit, J. Pragt, P. Rabou, F. Rigal, R. Roelfsema, G. Rousset, M. Saisse, H.-M. Schmid, E. Stadler, C. Thalmann, M. Turatto, S. Udry, F. Vakili, and R. Waters. SPHERE: a 'Planet Finder' instrument for the VLT. In *Ground-based and Airborne Instrumentation for Astronomy II*, volume 7014 of *Proc. SPIE*, page 701418, July 2008b. doi: 10.1117/12.790120.

M. Bonnefoy, A. Zurlo, J. L. Baudino, P. Lucas, D. Mesa, A.-L. Maire, A. Vigan, R. Galicher, D. Homeier, F. Marocco, R. Gratton, G. Chauvin, F. Allard, S. Desidera, M. Kasper, C. Moutou, A.-M. Lagrange, J. Antichi, A. Baruffolo, J. Baudrand, J.-L. Beuzit, A. Boccaletti, F. Cantalloube, M. Carbillet, J. Charton, R. U. Claudi, A. Costille, K. Dohlen, C. Dominik, D. Fantinel, P. Feautrier, M. Feldt, T. Fusco, P. Gigan, J. H. Girard, L. Gluck, C. Gry, T. Henning, M. Janson, M. Langlois, F. Madec, Y. Magnard, D. Maurel, D. Mawet, M. R. Meyer, J. Milli, O. Moeller-Nilsson, D. Mouillet, A. Pavlov, D. Perret, P. Pujet, S. P. Quanz, S. Rochat, G. Rousset, A. Roux, B. Salasnich, G. Salter, J.-F. Sauvage, H. M. Schmid, A. Sevin, C. Soenke, E. Stadler, M. Turatto, S. Udry, F. Vakili, Z. Wahhaj, and F. Wildi. First light of the VLT planet finder SPHERE. IV.

Physical and chemical properties of the planets around HR8799. *A&A*, 587:A58, Mar. 2016. doi: 10.1051/0004-6361/201526906.

M. Born and E. Wolf. *Principles of Optics*. Oct. 1999.

T. D. Brandt, M. W. McElwain, M. Janson, G. R. Knapp, K. Mede, M. A. Limbach, T. Groff, A. Burrows, J. E. Gunn, O. Guyon, J. Hashimoto, M. Hayashi, N. Jovanovic, N. J. Kasdin, M. Kuzuhara, R. H. Lupton, F. Martinache, S. Sorahana, D. S. Spiegel, N. Takato, M. Tamura, E. L. Turner, R. Vanderbei, and J. Wisniewski. CHARIS science: performance simulations for the Subaru Telescope's third-generation of exoplanet imaging instrumentation. In *Adaptive Optics Systems IV*, volume 9148 of *Proc. SPIE*, page 914849, July 2014. doi: 10.1117/12.2057256.

M. Carbillet, P. Bendjoya, L. Abe, G. Guerri, A. Boccaletti, J.-B. Daban, K. Dohlen, A. Ferrari, S. Robbe-Dubois, R. Douet, and F. Vakili. Apodized Lyot coronagraph for SPHERE/VLT. I. Detailed numerical study. *Experimental Astronomy*, 30:39–58, May 2011. doi: 10.1007/s10686-011-9219-4.

G. Chauvin, A.-M. Lagrange, C. Dumas, B. Zuckerman, D. Mouillet, I. Song, J.-L. Beuzit, and P. Lowrance. A giant planet candidate near a young brown dwarf. Direct VLT/NACO observations using IR wavefront sensing. *A&A*, 425:L29–L32, Oct. 2004. doi: 10.1051/0004-6361:200400056.

P. E. Ciddor. Refractive index of air: new equations for the visible and near infrared. *Appl. Opt.*, 35: 1566, Mar. 1996. doi: 10.1364/AO.35.001566.

L. M. Close, J. R. Males, D. A. Kopon, V. Gasho, K. B. Follette, P. Hinz, K. Morzinski, A. Uomoto, T. Hare, A. Riccardi, S. Esposito, A. Puglisi, E. Pinna, L. Busoni, C. Arcidiacono, M. Xompero, R. Briguglio, F. Quiros-Pacheco, and J. Argomedo. First closed-loop visible AO test results for the advanced adaptive secondary AO system for the Magellan Telescope: MagAO's performance and status. In *Adaptive Optics Systems III*, volume 8447 of *Proc. SPIE*, page 84470X, July 2012. doi: 10.1117/12.926545.

R. Cosentino, C. Lovis, F. Pepe, A. Collier Cameron, D. W. Latham, E. Molinari, S. Udry, N. Beza-wada, M. Black, A. Born, N. Buchschacher, D. Charbonneau, P. Figueira, M. Fleury, A. Galli, A. Gallie, X. Gao, A. Ghedina, C. Gonzalez, M. Gonzalez, J. Guerra, D. Henry, K. Horne, I. Hughes, D. Kelly, M. Lodi, D. Lunney, C. Maire, M. Mayor, G. Micela, M. P. Ordway, J. Pea-cock, D. Phillips, G. Piotto, D. Pollacco, D. Queloz, K. Rice, C. Riverol, L. Riverol, J. San Juan, D. Sasselov, D. Segransan, A. Sozzetti, D. Sosnowska, B. Stobie, A. Szentgyorgyi, A. Vick, and L. Weber. Harps-N: the new planet hunter at TNG. In *Ground-based and Airborne Instrumentation for Astronomy IV*, volume 8446 of *Proc. SPIE*, page 84461V, Sept. 2012. doi: 10.1117/12.925738.

T. Currie, O. Guyon, M. Tamura, T. Kudo, N. Jovanovic, J. Lozi, J. E. Schlieder, T. D. Brandt, J. Kuhn, E. Serabyn, M. Janson, J. Carson, T. Groff, N. J. Kasdin, M. W. McElwain, G. Singh, T. Uyama, M. Kuzuhara, E. Akiyama, C. Grady, S. Hayashi, G. Knapp, J.-m. Kwon, D. Oh, J. Wisniewski, M. Sitko, and Y. Yang. Subaru/SCExAO First-light Direct Imaging of a Young Debris Disk around HD 36546. *ApJ*, 836:L15, Feb. 2017. doi: 10.3847/2041-8213/836/1/L15.

G. V. David. *Computational Fourier Optics: A MATLAB Tutorial*. 2011.

R. Dekany, J. Roberts, R. Burruss, A. Bouchez, T. Truong, C. Baranec, S. Guiwits, D. Hale, J. Angione, T. Trinh, J. Zolkower, J. C. Shelton, D. Palmer, J. Henning, E. Croner, M. Troy, D. McKenna, J. Tesch, S. Hildebrandt, and J. Milburn. PALM-3000: Exoplanet Adaptive Optics for the 5 m Hale Telescope. *ApJ*, 776:130, Oct. 2013. doi: 10.1088/0004-637X/776/2/130.

N. Devaney, A. V. Goncharov, and J. C. Dainty. Chromatic effects of the atmosphere on astronomical adaptive optics. *Appl. Opt.*, 47:1072–1081, Mar. 2008. doi: 10.1364/AO.47.001072.

S. Egner, Y. Ikeda, M. Watanabe, Y. Hayano, T. Golota, M. Hattori, M. Ito, Y. Minowa, S. Oya, Y. Saito, H. Takami, and M. Iye. Atmospheric dispersion correction for the Subaru AO system. In *Adaptive Optics Systems II*, volume 7736 of *Proc. SPIE*, page 77364V, July 2010. doi: 10.1117/12.856579.

S. Esposito and A. Riccardi. Pyramid Wavefront Sensor behavior in partial correction Adaptive Optic systems. *A&A*, 369:L9–L12, Apr. 2001. doi: 10.1051/0004-6361:20010219.

R. Galicher, C. Marois, B. Macintosh, T. Barman, and Q. Konopacky. M-band Imaging of the HR 8799 Planetary System Using an Innovative LOCI-based Background Subtraction Technique. *ApJ*, 739:L41, Oct. 2011. doi: 10.1088/2041-8205/739/2/L41.

B. Garfinkel. An investigation in the theory of astronomical refraction. *AJ*, 50:169–179, Feb. 1944. doi: 10.1086/105767.

B. Garfinkel. Astronomical refraction in a polytropic atmosphere. *AJ*, 72:235–254, Mar. 1967. doi: 10.1086/110225.

J. W. Goodman. *Introduction to Fourier optics*. 2005.

R. M. Green. *Spherical astronomy*. 1985.

O. Guyon. Phase-induced amplitude apodization of telescope pupils for extrasolar terrestrial planet imaging. *A&A*, 404:379–387, June 2003. doi: 10.1051/0004-6361:20030457.

O. Guyon. Limits of Adaptive Optics for High-Contrast Imaging. *ApJ*, 629:592–614, Aug. 2005. doi: 10.1086/431209.

O. Guyon, E. A. Pluzhnik, M. J. Kuchner, B. Collins, and S. T. Ridgway. Theoretical Limits on Extrasolar Terrestrial Planet Detection with Coronagraphs. *ApJS*, 167:81–99, Nov. 2006. doi: 10.1086/507630.

O. Guyon, F. Martinache, R. Belikov, and R. Soummer. High Performance PIAA Coronagraphy with Complex Amplitude Focal Plane Masks. *ApJS*, 190:220–232, Oct. 2010. doi: 10.1088/0067-0049/190/2/220.

E. Han, S. X. Wang, J. T. Wright, Y. K. Feng, M. Zhao, O. Fakhouri, J. I. Brown, and C. Hancock. Exoplanet Orbit Database. II. Updates to Exoplanets.org. *PASP*, 126:827, Sept. 2014. doi: 10.1086/678447.

J. W. Hardy. *Adaptive Optics for Astronomical Telescopes*. July 1998.

Y. Hayano, H. Takami, O. Guyon, S. Oya, M. Hattori, Y. Saito, M. Watanabe, N. Murakami, Y. Minowa, M. Ito, S. Colley, M. Eldred, T. Golota, M. Dinkins, N. Kashikawa, and M. Iye. Current status of the laser guide star adaptive optics system for Subaru Telescope. In *Adaptive Optics Systems*, volume 7015 of *Proc. SPIE*, page 701510, July 2008. doi: 10.1117/12.789992.

P. Hibon, S. Thomas, J. Dunn, J. Atwood, L. Saddlemyer, N. Sadakuni, S. Goodsell, B. Macintosh, J. Graham, M. Perrin, F. Rantakyro, V. Fesquet, A. Serio, C. Quiroz, A. Cardwell, G. Gausachs, D. Savransky, D. Kerley, M. Hartung, R. Galvez, and K. Hardie. Characterization of the atmospheric dispersion corrector of the Gemini planet imager. In *Ground-based and Airborne Instrumentation for Astronomy V*, volume 9147 of *Proc. SPIE*, page 91474U, July 2014. doi: 10.1117/12.2055545.

K. W. Hodapp, R. Suzuki, M. Tamura, L. Abe, H. Suto, R. Kandori, J. Morino, T. Nishimura, H. Takami, O. Guyon, S. Jacobson, V. Stahlberger, H. Yamada, R. Shelton, J. Hashimoto, A. Tavrov, J. Nishikawa, N. Ukita, H. Izumiura, M. Hayashi, T. Nakajima, T. Yamada, and T. Usuda. HiCIAO: the Subaru Telescope's new high-contrast coronographic imager for adaptive optics. In *Ground-based and Airborne Instrumentation for Astronomy II*, volume 7014 of *Proc. SPIE*, page 701419, July 2008. doi: 10.1117/12.788088.

C. Y. Hohenkerk and A. Sinclair. *The Effect of Atmospheric Refraction on Laser Ranging Data*. H.M. Nautical Almanac Office, 1985.

E. Huby, G. Perrin, F. Marchis, S. Lacour, T. Kotani, G. Duchêne, E. Choquet, E. L. Gates, J. M. Woillez, O. Lai, P. Fédou, C. Collin, F. Chapron, V. Arslanyan, and K. J. Burns. FIRST, a fibered aperture masking instrument. I. First on-sky test results. *A&A*, 541:A55, May 2012. doi: 10.1051/0004-6361/201118517.

N. Jovanovic, O. Guyon, F. Martinache, C. Schwab, and N. Cvetojevic. How to inject light efficiently into single-mode fibers. In *Ground-based and Airborne Instrumentation for Astronomy V*, volume 9147 of *Proc. SPIE*, page 91477P, July 2014. doi: 10.1117/12.2057210.

N. Jovanovic, O. Guyon, F. Martinache, P. Pathak, J. Hagelberg, and T. Kudo. Artificial Incoherent Speckles Enable Precision Astrometry and Photometry in High-contrast Imaging. *ApJ*, 813:L24, Nov. 2015a. doi: 10.1088/2041-8205/813/2/L24.

N. Jovanovic, F. Martinache, O. Guyon, C. Clergeon, G. Singh, T. Kudo, V. Garrel, K. Newman, D. Doughty, J. Lozi, J. Males, Y. Minowa, Y. Hayano, N. Takato, J. Morino, J. Kuhn, E. Serabyn, B. Norris, P. Tuthill, G. Schworer, P. Stewart, L. Close, E. Huby, G. Perrin, S. Lacour, L. Gauchet, S. Vievard, N. Murakami, F. Oshiyama, N. Baba, T. Matsuo, J. Nishikawa, M. Tamura, O. Lai, F. Marchis, G. Duchene, T. Kotani, and J. Woillez. The Subaru Coronagraphic Extreme Adaptive Optics System: Enabling High-Contrast Imaging on Solar-System Scales. *PASP*, 127:890, Sept. 2015b. doi: 10.1086/682989.

N. Jovanovic, N. Cvetojevic, C. Schwab, B. Norris, J. Lozi, S. Gross, C. Betters, G. Singh, O. Guyon, F. Martinache, D. Doughty, and P. Tuthill. Efficiently feeding single-mode fiber photonic spectrographs with an extreme adaptive optics system: on-sky characterization and preliminary spectroscopy. In *Ground-based and Airborne Instrumentation for Astronomy VI*, volume 9908 of *Proc. SPIE*, page 99080R, Aug. 2016. doi: 10.1117/12.2234299.

N. J. Kasdin, R. J. Vanderbei, D. N. Spergel, and M. G. Littman. Extrasolar Planet Finding via Optimal Apodized-Pupil and Shaped-Pupil Coronagraphs. *ApJ*, 582:1147–1161, Jan. 2003. doi: 10.1086/344751.

A. L. Kraus and M. J. Ireland. LkCa 15: A Young Exoplanet Caught at Formation? *ApJ*, 745:5, Jan. 2012. doi: 10.1088/0004-637X/745/1/5.

D. Lafrenière, C. Marois, R. Doyon, D. Nadeau, and É. Artigau. A New Algorithm for Point-Spread Function Subtraction in High-Contrast Imaging: A Demonstration with Angular Differential Imaging. *ApJ*, 660:770–780, May 2007. doi: 10.1086/513180.

J. Lozi, O. Guyon, N. Jovanovic, G. Singh, S. Goebel, B. Norris, and H. Okita. Characterizing and mitigating vibrations for SCExAO. In *Adaptive Optics Systems V*, volume 9909 of *Proc. SPIE*, page 99090J, July 2016. doi: 10.1117/12.2233040.

B. Lyot. The study of the solar corona and prominences without eclipses (George Darwin Lecture, 1939). *MNRAS*, 99:580, June 1939. doi: 10.1093/mnras/99.8.580.

B. Macintosh, J. R. Graham, P. Ingraham, Q. Konopacky, C. Marois, M. Perrin, L. Poyneer, B. Bauman, T. Barman, A. S. Burrows, A. Cardwell, J. Chilcote, R. J. De Rosa, D. Dillon, R. Doyon, J. Dunn, D. Erikson, M. P. Fitzgerald, D. Gavel, S. Goodsell, M. Hartung, P. Hibon, P. Kalas, J. Larkin, J. Maire, F. Marchis, M. S. Marley, J. McBride, M. Millar-Blanchaer, K. Morzinski, A. Norton, B. R. Oppenheimer, D. Palmer, J. Patience, L. Pueyo, F. Rantakyro, N. Sadakuni, L. Saddlemyer, D. Savransky, A. Serio, R. Soummer, A. Sivaramakrishnan, I. Song, S. Thomas, J. K. Wallace, S. Wiktorowicz, and S. Wolff. First light of the Gemini Planet Imager. *Proceedings of the National Academy of Science*, 111:12661–12666, Sept. 2014a. doi: 10.1073/pnas.1304215111.

B. Macintosh, J. R. Graham, P. Ingraham, Q. Konopacky, C. Marois, M. Perrin, L. Poyneer, B. Bauman, T. Barman, A. S. Burrows, A. Cardwell, J. Chilcote, R. J. De Rosa, D. Dillon, R. Doyon, J. Dunn, D. Erikson, M. P. Fitzgerald, D. Gavel, S. Goodsell, M. Hartung, P. Hibon, P. Kalas, J. Larkin, J. Maire, F. Marchis, M. S. Marley, J. McBride, M. Millar-Blanchaer, K. Morzinski, A. Norton, B. R. Oppenheimer, D. Palmer, J. Patience, L. Pueyo, F. Rantakyro, N. Sadakuni, L. Saddlemyer, D. Savransky, A. Serio, R. Soummer, A. Sivaramakrishnan, I. Song, S. Thomas, J. K. Wallace, S. Wiktorowicz, and S. Wolff. First light of the Gemini Planet Imager. *Proceedings of the National Academy of Science*, 111:12661–12666, Sept. 2014b. doi: 10.1073/pnas.1304215111.

P.-Y. Madec. Overview of deformable mirror technologies for adaptive optics and astronomy. In *Adaptive Optics Systems III*, volume 8447 of *Proc. SPIE*, page 844705, July 2012. doi: 10.1117/12.924892.

C. Marois, D. Lafrenière, R. Doyon, B. Macintosh, and D. Nadeau. Angular Differential Imaging: A Powerful High-Contrast Imaging Technique. *ApJ*, 641:556–564, Apr. 2006. doi: 10.1086/500401.

C. Marois, B. Macintosh, T. Barman, B. Zuckerman, I. Song, J. Patience, D. Lafrenière, and R. Doyon. Direct Imaging of Multiple Planets Orbiting the Star HR 8799. *Science*, 322:1348, Nov. 2008. doi: 10.1126/science.1166585.

F. Martinache, O. Guyon, N. Jovanovic, C. Clergeon, G. Singh, T. Kudo, T. Currie, C. Thalmann, M. McElwain, and M. Tamura. On-Sky Speckle Nulling Demonstration at Small Angular Separation with SCExAO. *PASP*, 126:565, June 2014a. doi: 10.1086/677141.

F. Martinache, O. Guyon, N. Jovanovic, C. Clergeon, G. Singh, T. Kudo, T. Currie, C. Thalmann, M. McElwain, and M. Tamura. On-Sky Speckle Nulling Demonstration at Small Angular Separation with SCExAO. *PASP*, 126:565, June 2014b. doi: 10.1086/677141.

D. Mawet, P. Riaud, O. Absil, and J. Surdej. Annular Groove Phase Mask Coronagraph. *ApJ*, 633: 1191–1200, Nov. 2005. doi: 10.1086/462409.

D. Mawet, E. Serabyn, K. Liewer, C. Hanot, S. McEldowney, D. Shemo, and N. O'Brien. Optical Vectorial Vortex Coronagraphs using Liquid Crystal Polymers: theory, manufacturing and laboratory demonstration. *Optics Express*, 17:1902–1918, Feb. 2009. doi: 10.1364/OE.17.001902.

D. Mawet, E. Serabyn, K. Liewer, R. Burruss, J. Hickey, and D. Shemo. The Vector Vortex Coronagraph: Laboratory Results and First Light at Palomar Observatory. *ApJ*, 709:53–57, Jan. 2010. doi: 10.1088/0004-637X/709/1/53.

D. Mawet, L. Pueyo, P. Lawson, L. Mugnier, W. Traub, A. Boccaletti, J. T. Trauger, S. Gladysz, E. Serabyn, J. Milli, R. Belikov, M. Kasper, P. Baudoz, B. Macintosh, C. Marois, B. Oppenheimer, H. Barrett, J.-L. Beuzit, N. Devaney, J. Girard, O. Guyon, J. Krist, B. Mennesson, D. Mouillet, N. Murakami, L. Poyneer, D. Savransky, C. Vérinaud, and J. K. Wallace. Review of small-angle coronagraphic techniques in the wake of ground-based second-generation adaptive optics systems. In *Space Telescopes and Instrumentation 2012: Optical, Infrared, and Millimeter Wave*, volume 8442 of *Proc. SPIE*, page 844204, Sept. 2012. doi: 10.1117/12.927245.

M. Mayor and D. Queloz. A Jupiter-mass companion to a solar-type star. *Nature*, 378:355–359, Nov. 1995. doi: 10.1038/378355a0.

M. Mayor, F. Pepe, D. Queloz, F. Bouchy, G. Rupprecht, G. Lo Curto, G. Avila, W. Benz, J.-L. Bertaux, X. Bonfils, T. Dall, H. Dekker, B. Delabre, W. Eckert, M. Fleury, A. Gilliotte, D. Gojak, J. C. Guzman, D. Kohler, J.-L. Lizon, A. Longinotti, C. Lovis, D. Megevand, L. Pasquini, J. Reyes, J.-P. Sivan, D. Sosnowska, R. Soto, S. Udry, A. van Kesteren, L. Weber, and U. Weilenmann. Setting New Standards with HARPS. *The Messenger*, 114:20–24, Dec. 2003.

B. A. Mazin, B. Bumble, S. R. Meeker, K. O'Brien, S. McHugh, and E. Langman. A superconducting focal plane array for ultraviolet, optical, and near-infrared astrophysics. *Optics Express*, 20:1503, Jan. 2012. doi: 10.1364/OE.20.001503.

M. W. McElwain, T. D. Brandt, M. Janson, G. R. Knapp, M. A. Peters, A. S. Burrows, A. Carlotti, M. A. Carr, T. Groff, J. E. Gunn, O. Guyon, M. Hayashi, N. J. Kasdin, M. Kuzuhara, R. H. Lupton, F. Martinache, D. Spiegel, N. Takato, M. Tamura, E. L. Turner, and R. J. Vanderbei. Scientific design of a high contrast integral field spectrograph for the Subaru Telescope. In *Ground-based and Airborne Instrumentation for Astronomy IV*, volume 8446 of *Proc. SPIE*, page 84469C, Sept. 2012. doi: 10.1117/12.927108.

Y. Minowa, Y. Hayano, S. Oya, M. Watanabe, M. Hattori, O. Guyon, S. Egner, Y. Saito, M. Ito, H. Takami, V. Garrel, S. Colley, T. Golota, and M. Iye. Performance of Subaru adaptive optics system AO188. In *Adaptive Optics Systems II*, volume 7736 of *Proc. SPIE*, page 77363N, July 2010. doi: 10.1117/12.857818.

L. M. Mugnier, A. Cornia, J.-F. Sauvage, N. Védrenne, T. Fusco, and G. Rousset. Maximum likelihood-based method for angular differential imaging. In *Adaptive Optics Systems*, volume 7015 of *Proc. SPIE*, page 70152B, July 2008. doi: 10.1117/12.790329.

N. Murakami, J. Nishikawa, K. Yokochi, M. Tamura, N. Baba, and L. Abe. Achromatic Eight-octant Phase-mask Coronagraph using Photonic Crystal. *ApJ*, 714:772–777, May 2010. doi: 10.1088/0004-637X/714/1/772.

B. Norris, G. Schworer, P. Tuthill, N. Jovanovic, O. Guyon, P. Stewart, and F. Martinache. The VAMPIRES instrument: imaging the innermost regions of protoplanetary discs with polarimetric interferometry. *MNRAS*, 447:2894–2906, Mar. 2015. doi: 10.1093/mnras/stu2529.

P. Pathak, O. Guyon, N. Jovanovic, J. Lozi, F. Martinache, Y. Minowa, T. Kudo, H. Takami, Y. Hayano, and N. Narita. A High-precision Technique to Correct for Residual Atmospheric Dispersion in High-contrast Imaging Systems. *PASP*, 128(12):124404, Dec. 2016. doi: 10.1088/1538-3873/128/970/124404.

A. C. Phillips, R. Suzuki, J. E. Larkin, A. M. Moore, Y. Hayano, T. Tsuzuki, and S. A. Wright. The Infrared Imaging Spectrograph (IRIS) for TMT: the ADC optical design. In *Ground-based and Airborne Instrumentation for Astronomy VI*, volume 9908 of *Proc. SPIE*, page 9908A1, Aug. 2016. doi: 10.1117/12.2232952.

D. L. Pollacco, I. Skillen, A. Collier Cameron, D. J. Christian, C. Hellier, J. Irwin, T. A. Lister, R. A. Street, R. G. West, D. R. Anderson, W. I. Clarkson, H. Deeg, B. Enoch, A. Evans, A. Fitzsimmons, C. A. Haswell, S. Hodgkin, K. Horne, S. R. Kane, F. P. Keenan, P. F. L. Maxted, A. J. Norton, J. Osborne, N. R. Parley, R. S. I. Ryans, B. Smalley, P. J. Wheatley, and D. M. Wilson. The WASP Project and the SuperWASP Cameras. *PASP*, 118:1407–1418, Oct. 2006. doi: 10.1086/508556.

R. Ragazzoni. Pupil plane wavefront sensing with an oscillating prism. *Journal of Modern Optics*, 43:289–293, Feb. 1996. doi: 10.1080/09500349608232742.

G. R. Ricker, J. N. Winn, R. Vanderspek, D. W. Latham, G. Á. Bakos, J. L. Bean, Z. K. Berta-Thompson, T. M. Brown, L. Buchhave, N. R. Butler, R. P. Butler, W. J. Chaplin, D. Charbonneau, J. Christensen-Dalsgaard, M. Clampin, D. Deming, J. Doty, N. De Lee, C. Dressing, E. W. Dunham, M. Endl, F. Fressin, J. Ge, T. Henning, M. J. Holman, A. W. Howard, S. Ida, J. Jenkins, G. Jernigan, J. A. Johnson, L. Kaltenegger, N. Kawai, H. Kjeldsen, G. Laughlin, A. M. Levine, D. Lin, J. J. Lissauer, P. MacQueen, G. Marcy, P. R. McCullough, T. D. Morton, N. Narita, M. Paegert, E. Palle, F. Pepe, J. Pepper, A. Quirrenbach, S. A. Rinehart, D. Sasselov, B. Sato, S. Seager, A. Sozzetti, K. G. Stassun, P. Sullivan, A. Szentgyorgyi, G. Torres, S. Udry, and J. Villasenor. Transiting Exoplanet Survey Satellite (TESS). In *Space Telescopes and Instrumentation 2014: Optical, Infrared, and Millimeter Wave*, volume 9143 of *Proc. SPIE*, page 914320, Aug. 2014. doi: 10.1117/12.2063489.

F. Roddier. The effects of atmospheric turbulence in optical astronomy. *Progress in optics. Volume 19. Amsterdam, North-Holland Publishing Co., 1981, p. 281-376.*, 19:281–376, 1981. doi: 10.1016/S0079-6638(08)70204-X.

F. Roddier. *Adaptive Optics in Astronomy*. Nov. 2004.

D. Rouan, P. Riaud, A. Boccaletti, Y. Clénet, and A. Labeyrie. The Four-Quadrant Phase-Mask Coronagraph. I. Principle. *PASP*, 112:1479–1486, Nov. 2000. doi: 10.1086/317707.

G. Rousset. *Wave-front sensors*. 1999.

Y. Saito, Y. Hayano, M. Ito, Y. Minowa, S. Egner, S. Oya, M. Watanabe, M. Hattori, V. Garrel, K. Akagawa, O. Guyon, S. Colley, T. Golota, N. Saito, A. Takazawa, M. Ito, H. Takami, S. Wada, and M. Iye. The performance of the laser guide star system for the Subaru Telescope. In *Adaptive Optics Systems II*, volume 7736 of *Proc. SPIE*, page 773653, July 2010. doi: 10.1117/12.856484.

J.-F. Sauvage, T. Fusco, M. Lamb, J. Girard, M. Brinkmann, A. Guesalaga, P. Wizinowich, J. O'Neal, M. N'Diaye, A. Vigan, D. Mouillet, J.-L. Beuzit, M. Kasper, M. Le Louarn, J. Milli, K. Dohlen, B. Neichel, P. Bourget, P. Haguenauer, and D. Mawet. Tackling down the low wind effect on SPHERE instrument. In *Adaptive Optics Systems V*, volume 9909 of *Proc. SPIE*, page 990916, July 2016. doi: 10.1117/12.2232459.

M. Schöck, T. Do, B. L. Ellerbroek, L. Gilles, G. Herriot, L. Meyer, R. Suzuki, L. Wang, and S. Yelda. Thirty Meter Telescope astrometry error budget. In *Adaptive Optics Systems IV*, volume 9148 of *Proc. SPIE*, page 91482L, July 2014. doi: 10.1117/12.2057089.

R. V. Shack, J. D. Rancourt, and H. Morrow. Effects of dilution on a six-element synthetic aperture. *Appl. Opt.*, 10:257–259, Feb. 1971. doi: 10.1364/AO.10.000257.

A. Sinclair. *The Effect of Atmospheric Refraction on Laser Ranging Data*. H.M. Nautical Almanac Office, 1982.

G. Singh, J. Lozi, O. Guyon, P. Baudoz, N. Jovanovic, F. Martinache, T. Kudo, E. Serabyn, and J. Kuhn. On-Sky Demonstration of Low-Order Wavefront Sensing and Control with Focal Plane Phase Mask Coronagraphs. *PASP*, 127:857, Sept. 2015a. doi: 10.1086/682726.

G. Singh, J. Lozi, O. Guyon, P. Baudoz, N. Jovanovic, F. Martinache, T. Kudo, E. Serabyn, and J. Kuhn. On-Sky Demonstration of Low-Order Wavefront Sensing and Control with Focal Plane Phase Mask Coronagraphs. *PASP*, 127:857, Sept. 2015b. doi: 10.1086/682726.

A. Sivaramakrishnan and B. R. Oppenheimer. Astrometry and Photometry with Coronagraphs. *ApJ*, 647:620–629, Aug. 2006. doi: 10.1086/505192.

A. Sivaramakrishnan, C. D. Koresko, R. B. Makidon, T. Berkefeld, and M. J. Kuchner. Ground-based Coronagraphy with High-order Adaptive Optics. *ApJ*, 552:397–408, May 2001. doi: 10.1086/320444.

A. J. Skemer, P. M. Hinz, W. F. Hoffmann, L. M. Close, S. Kendrew, R. J. Mathar, R. Stuik, T. P. Greene, C. E. Woodward, and M. S. Kelley. A Direct Measurement of Atmospheric Dispersion in N-band Spectra: Implications for Mid-IR Systems on ELTs. *PASP*, 121:897, Aug. 2009. doi: 10.1086/605312.

W. M. Smart. *Text-book on spherical astronomy*. 1965.

R. Soummer, L. Pueyo, A. Sivaramakrishnan, and R. J. Vanderbei. Fast computation of Lyot-style coronagraph propagation. *Optics Express*, 15:15935, 2007a. doi: 10.1364/OE.15.015935.

R. Soummer, L. Pueyo, A. Sivaramakrishnan, and R. J. Vanderbei. Fast computation of Lyot-style coronagraph propagation. *Optics Express*, 15:15935, 2007b. doi: 10.1364/OE.15.015935.

R. Soummer, A. Sivaramakrishnan, B. R. Oppenheimer, R. Roberts, D. Brenner, A. Carlotti, L. Pueyo, B. Macintosh, B. Bauman, L. Saddlemyer, D. Palmer, D. Erickson, C. Dorrer, K. Caputa, C. Marois, K. Wallace, E. Griffiths, and J. Mey. The Gemini Planet Imager coronagraph testbed. In *Techniques and Instrumentation for Detection of Exoplanets IV*, volume 7440 of *Proc. SPIE*, page 74400R, Aug. 2009. doi: 10.1117/12.826700.

R. Soummer, L. Pueyo, and J. Larkin. Detection and Characterization of Exoplanets and Disks Using Projections on Karhunen-Loève Eigenimages. *ApJ*, 755:L28, Aug. 2012. doi: 10.1088/2041-8205/755/2/L28.

P. Spanò. Accurate astronomical atmospheric dispersion models in ZEMAX. In *Advances in Optical and Mechanical Technologies for Telescopes and Instrumentation*, volume 9151 of *Proc. SPIE*, page 915157, July 2014. doi: 10.1117/12.2057072.

H. Takami, N. Takato, M. Otsubo, T. Kanzawa, Y. Kamata, K. Nakashima, and M. Iye. Adaptive optics system for Cassegrain focus of SUBARU 8.2-m telescope. In D. Bonaccini and R. K. Tyson, editors, *Adaptive Optical System Technologies*, volume 3353 of *Proc. SPIE*, pages 500–507, Sept. 1998. doi: 10.1117/12.321685.

H. Takami, M. Watanabe, N. Takato, S. Colley, M. Eldred, T. Kane, O. Guyon, M. Hattori, M. Goto, M. Iye, Y. Hayano, Y. Kamata, N. Arimoto, N. Kobayashi, and Y. Minowa. Laser guide star AO project at the Subaru Telescope. In D. Bonaccini Calia, B. L. Ellerbroek, and R. Ragazzoni, editors, *Advancements in Adaptive Optics*, volume 5490 of *Proc. SPIE*, pages 837–845, Oct. 2004. doi: 10.1117/12.550839.

K. Wagner, D. Apai, M. Kasper, K. Kratter, M. McClure, M. Robberto, and J.-L. Beuzit. Direct imaging discovery of a Jovian exoplanet within a triple-star system. *Science*, 353:673–678, Aug. 2016. doi: 10.1126/science.aaf9671.

G. Walker, J. Matthews, R. Kuschnig, R. Johnson, S. Rucinski, J. Pazder, G. Burley, A. Walker, K. Skaret, R. Zee, S. Grocott, K. Carroll, P. Sinclair, D. Sturgeon, and J. Harron. The MOST Asteroseismology Mission: Ultraprecise Photometry from Space. *PASP*, 115:1023–1035, Sept. 2003. doi: 10.1086/377358.

O. Wertz, O. Absil, C. A. Gómez González, J. Milli, J. H. Girard, D. Mawet, and L. Pueyo. VLT/SPHERE robust astrometry of the HR8799 planets at milliarcsecond-level accuracy. Orbital architecture analysis with PyAstrOFit. *A&A*, 598:A83, Feb. 2017. doi: 10.1051/0004-6361/201628730.

A. Wolszczan. Confirmation of Earth-Mass Planets Orbiting the Millisecond Pulsar PSR B1257+12. *Science*, 264:538–542, Apr. 1994. doi: 10.1126/science.264.5158.538.

A. Wolszczan and D. A. Frail. A planetary system around the millisecond pulsar PSR1257 + 12. *Nature*, 355:145–147, Jan. 1992. doi: 10.1038/355145a0.

C. G. Wynne. Correction of atmospheric dispersion in the infrared. *MNRAS*, 282:863–867, Oct. 1996. doi: 10.1093/mnras/282.3.863.

A. T. Young. Sunset Science. IV. Low-Altitude Refraction. *AJ*, 127:3622–3637, June 2004. doi: 10.1086/420806.

T. J. Ypma. Historical development of the newton–raphson method. *SIAM Review*, 37(4):531–551, 1995. doi: 10.1137/1037125.